A Numerical Study of Wall Erosion and Material Transport in Hall Thrusters

by

Brandon Denis Smith

A dissertation submitted in partial fulfillment
of the requirements for the degree of
Doctor of Philosophy
(Aerospace Engineering)
in The University of Michigan
2015

Doctoral Committee:

Professor Iain D. Boyd, Chair
Professor John E. Foster
Professor Alec D. Gallimore
Hani Kamhawi, NASA Glenn Research Center

“The best way to live a full life is to be a child, no matter what your age.”

For my brothers, Nathan and Austin

ACKNOWLEDGEMENTS

A number of people have helped to make my experience at the University of Michigan as enjoyable as it has been. I would first like to thank my doctoral advisor, Iain Boyd, for inviting me to join NGPDL back in 2010. Although I had next to no experience in scientific computing before coming to Michigan, I have no doubt now that this was the right choice for me. Thanks to Professor Boyd's invitation I have discovered the boundless joy of getting a simulation to work after days of programming, and have found the greatest city I've ever had the pleasure to live in. Professor Boyd has also served as an excellent advisor ever since I arrived here, supporting the ideas I brought to him, pointing me in the right direction when I went astray, and directing me towards any new opportunities whenever they arose. His presence has played a significant role in making my five years in graduate school some of the best of my life.

I would also like to thank some of the alumni and other members of NGPDL for their assistance and support over these last five years. In particular, I would like to thank Erin Farbar and Paul Giuliano, who were always willing to assist me whenever I was stuck or confused. Thanks also to Kelly Stephani for working with me on the molecular dynamics model. It was a blast working together and I learned a lot from her experience. I would also like to thank Kentaro Hara, my classmate and officemate, for throwing his ideas and questions my way and for helping to develop a parallelized PIC solver when I really should have been working on my dissertation research. I think we have learned a lot from each other over the years, and I hope to continue working with him even after he leaves Michigan.

I'd like to thank the many members of the Plasmadynamics and Electric Propulsion Laboratory for providing their expansive knowledge of Hall thruster physics and testing. Namely, thanks to Mike Sekerak for being the voice of reason whenever I freaked out while studying for quals and for our many productive discussions on Hall thrusters. Thanks to Frans Ebersohn for teaching me all the things I forgot about PIC and for helping with the development of my aforementioned pet project. I would also like to thank the many staff members of the Department of Aerospace Engineering—namely Denise Phelps, Cindy Enoch, and Julie Power—for making sure I don't starve and for helping me through all the red tape that shows up when you try to get a graduate degree. In addition, I would like to thank Josh Anderson from the Department of Chemical Engineering for all of his assistance with HOOMD. Josh, it has honestly been a thrill and a pleasure to work with your code.

There are several researchers at NASA Glenn Research Center whom I'd like to thank. First, thanks to Hani Kamhawi for serving as my mentor during my summer visits at GRC. In spite of his ever-packed schedule, Hani managed to find time for me whenever I visited. He also taught me a lot about Hall thruster testing and was a big help when writing papers. Thanks also to Rohit Shastry and Wensheng Huang, who supplied much of the experimental data I needed to validate my model. Thanks to John Yim, my predecessor, who helped immensely as I worked to build on his research. I am grateful to all of you at GRC for your support and assistance.

I'd like to extend a huge thanks to the friends I've made here at Michigan. To Tim and Matt, my fellow founding members of trivia team Taco Cat, thanks for all the good times we had together at the Blue Leprechaun and elsewhere. To Tony, thanks for all the crazy nights spent at your shady house in Ypsi. My next Rondeau will be dedicated to you. To Ashley, thanks for laughing at all my dumb jokes and impersonations. It always made me feel more funny than I actually am. To Lauren, thanks for being the broest of bros, bro. Finally, to my trivia and Risk buddies Luke, Michelle, and Jon, thanks for your help in turning North America into a mutant-ridden nuclear wasteland and in founding the proud city of Doodyville. May its energy shields forever protect it from the onslaught of dump trucks, bear cavalry, and mechs.

Finally, I would like to thank my family. Mom, special thanks to you. If there is any one person who is responsible for making me who I am today, it's you. You are the best mom I could ask for, and I want you to know how much your love and care mean to me. Thank you.

TABLE OF CONTENTS

LIST OF FIGURES

Figure

LIST OF TABLES

Table

LIST OF APPENDICES

Appendix

CHAPTER I

Introduction

Satellite technology has become a pillar of life in the developed world. Between cellular phones, digital satellite radio, GPS, and numerous other technologies, many people utilize some form of satellite communication on a daily basis. These communication technologies allow us to stay in touch with our loved ones from across the globe, pinpoint one's location to within 10 m,[1] and transmit orders to troops around the world nearly instantaneously, among other things. There are also deep-space exploration satellites that travel through our solar system and to distant planets, expanding our knowledge of our system's history and of our origins. Space-based telescopes allow us to view and identify distant stars and galaxies, granting us valuable insight into the history of the universe.

The extensive use of satellites by humankind is much more likely to expand than to shrink, so there is a clear need to continue developing satellite technologies to make them better, cheaper, and more reliable. Of the various subsystems required to make a satellite work, the propulsion system in particular has tremendous room for improvement. A more durable and reliable propulsion system, for example, would enable reduced system redundancy, in turn reducing spacecraft mass and, thus launch cost. Hence, the research and development of novel and improved in-space propulsion systems is a very rich and diverse field of study, and is the focus of this work.

1.1 The Rocket Equation

The fundamental governing equation of propulsion systems is the *rocket equation*. This is derived from Newton's second law:

$$\mathbf{F} = \frac{d\mathbf{p}}{dt}, \tag{1.1}$$

where $\mathbf{F}$ is the net force from external sources and $\mathbf{p}$ is the momentum of the vehicle system, including propellant. Neglecting aerodynamic forces and gravity, the net external force for a self-propelled vehicle is zero. At any point in time, the vehicle has some instantaneous mass m and instantaneous velocity v. Meanwhile, the spacecraft mass *decreases* in time due to the consumption of propellant. Assuming a constant propellant mass flow rate of $\dot{m}$ and a constant, uniform exhaust velocity u_e relative to the vehicle body, Eq. 1.1 becomes

$$0 = m\frac{dv}{dt} - \dot{m}u_e. \tag{1.2}$$

Integrating and rearranging terms gives the rocket equation:

$$m_1 = m_0 \exp\left(\frac{-\left|v_1 - v_0\right|}{u_e}\right) = m_0 \exp\left(\frac{-\Delta v}{u_e}\right), \tag{1.3}$$

where Δv is the required change in the vehicle velocity to execute some maneuver or maneuvers. The rocket equation is most often written in terms of the *specific impulse*, I_{sp}:

$$I_{sp} \equiv \frac{F_{th}}{\dot{m}g}, \tag{1.4}$$

$$\frac{m_1}{m_0} = \exp\left(\frac{-\Delta v}{gI_{sp}}\right), \tag{1.5}$$

where F_{th} is the thrust force of the propulsion system and g is the acceleration due

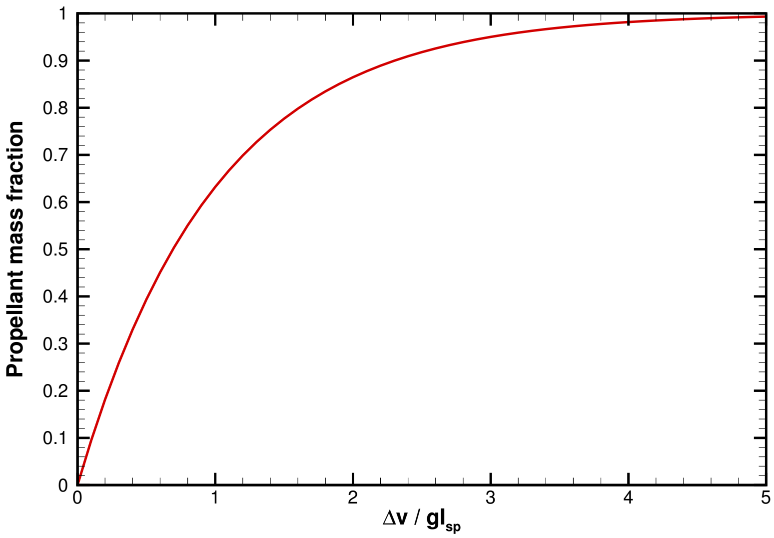

Figure 1.1: Propellant mass fraction as a function of $^{\Delta v}/_{gI_{sp}}$

to gravity at sea level on Earth.

In spacecraft design, it is very useful to determine the *propellant mass fraction* for a mission:

$$\frac{m_p}{m_0} = 1 - \exp\left(\frac{-\Delta v}{gI_{sp}}\right), \tag{1.6}$$

where Δv is the sum for all maneuvers required over the course of the mission. This quantity is plotted in Fig. 1.1. This plot indicates that when Δv is on the order of gI_{sp}, the majority of the spacecraft mass at the time of deployment is propellant mass. Ideally, a spacecraft will carry as little propellant as allowable to complete its mission, as propellant mass is still mass, and launching mass into orbit is very costly. Hence, a propulsion system with a high I_{sp} is desirable in order to minimize the required propellant mass for a mission.

Table 1.1 shows the typical range of I_{sp} and thrust for a few types of in-space propulsion systems.[2] The electric thrusters—arcjets, gridded ion thrusters, Hall effect thrusters, and MPD thrusters—all have much higher specific impulse than the chemical rockets, and are thus more desirable from a propellant mass standpoint.

Table 1.1: Characteristic values of specific impulse and thrust for various types of in-space propulsion systems.

Thruster type	I_{sp} range, s	Thrust range, N
Liquid chemical monopropellant	150–250	$\lesssim 10^6$
Liquid chemical bipropellant	300–500	$\lesssim 10^6$
Arcjet	500–1500	0.5–5
Gridded ion thruster	2000–6000	10^{-6}–0.5
Hall effect thruster	1500–3000	10^{-6}–0.5
Magnetoplasmadynamic (MPD)	~ 2000	20–200

One of these thruster types, the Hall effect thruster, is the focus of the present work. However, due to their low thrust, electric propulsion systems must operate for much longer periods of time to achieve the same total impulse as a chemical rockets, as will be discussed below.

1.2 Hall Effect Thrusters

Hall effect thrusters (HETs), often simply called Hall thrusters, are gridless electrostatic propulsion devices that produce a thrust force by accelerating ions through an electric field. A typical Hall thruster consists of an annular discharge channel with an anode placed at its upstream end and a hollow cathode placed just downstream of the channel exit. The anode is biased to some positive potential relative to the cathode and also serves as the injection point for the propellant gas. The hollow cathode serves as an electron source, providing some electrons that ionize the propellant atoms in the discharge channel and others that neutralize the ions accelerated downstream. The body of the thruster is made primarily of magnetic iron, and electromagnetic coils are placed on either side of the discharge channel in order to produce a nominally radial magnetic field. The applied magnetic field is strongest near the exit plane of the discharge channel and inhibits the flow of electrons between the cathode and the anode. This results in a strong axial electric field in the region

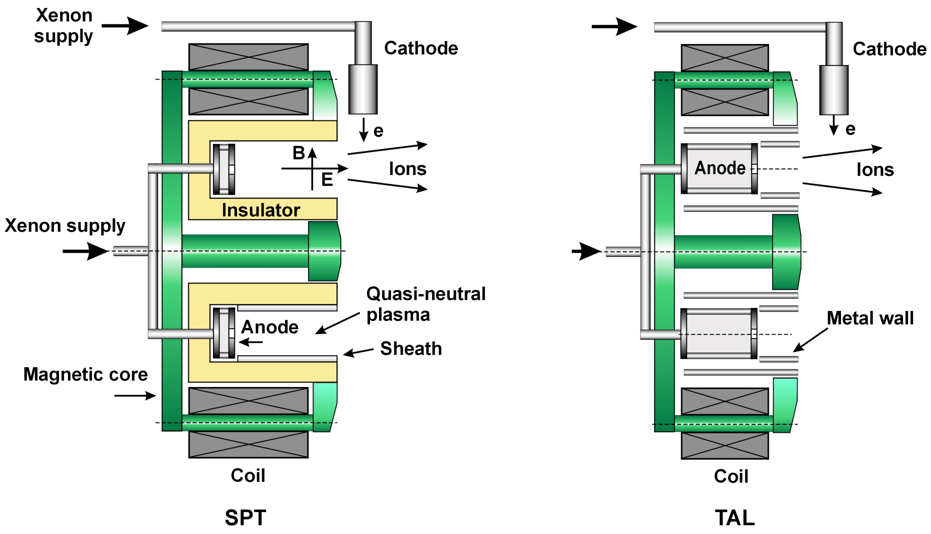

Figure 1.2: Schematic of the SPT and TAL variants of Hall effect thrusters.

of the large radial magnetic field. The crossed-field configuration traps the electrons in an $\mathbf{E} \times \mathbf{B}$ drift, similar to the Hall effect observed in current-carrying metals under transverse magnetic fields. It is from this phenomenon that the name "Hall effect thruster" is derived. Due to their enormous mass compared to the electrons, the ions remain unmagnetized and accelerate along the electric field lines, producing thrust.

There are two common variants of the basic Hall thruster design: the stationary plasma thruster (SPT) and the thruster with anode layer (TAL), both developed in the USSR in the 1960s and 1970s. A schematic of each design is shown in Fig. 1.2. The SPT design is characterized by a discharge channel with an axial length several times greater than its radial width. In order to shield the magnetic coils and pole pieces from the plasma discharge, the channel is lined with a dielectric material, usually hexagonal boron nitride (h-BN) or a BN-based ceramic such as borosil. Dielectric materials are chosen so that the channel walls do not form a conductive pathway between the cathode and anode, thus reducing electron losses. The TAL design is characterized by a discharge channel whose length is less than its width. The channel walls are lined with an electrically conductive material that is biased to a negative potential in order to repel electrons. The differences in geometry and material composition between the

SPT and TAL designs cause different physical phenomena to manifest, but both obey the basic operating principles of Hall thrusters. Of the two designs, the SPT is by far more common, having been the subject of extensive research and development over the past several decades. It also has a much stronger flight heritage, with roughly a hundred SPT units having been used on successful satellite missions in the USSR.[3] Thus, the SPT design is the focus of the present research.

Hall thrusters have a number of advantages compared to other propulsion systems apart from the relatively high I_{sp}. Compared to gridded ion thrusters, Hall thrusters have a smaller footprint for the same power level, are electronically simpler, and provide a greater ratio of thrust to input power. Hall thrusters also have a strong flight heritage, with roughly a hundred being flown on USSR satellites between 1972 and 1991.[3] The European Space Agency's (ESA) successful SMART-1 technology demonstration mission, launched in 2003, employed a Hall thruster for primary propulsion.[4,5] In 2011, the US Air Force satellite AEHF-1 successfuly reached geosynchronous orbit from its initial transfer orbit using Hall thrusters after the failure of the primary propulsion system.[6] Finally, NASA's planned Asteroid Redirect Mission (ARM)[7] will utilize a state-of-the-art Hall thruster to reach an asteroid and return that asteroid to translunar orbit.

1.2.1 Hall Thruster Lifetime

The primary challenge for utilizing Hall thrusters as primary propulsion is the lifetime requirements. Consider, for example, NASA's Asteroid Redirect Mission (ARM).[7] Based on a few proposed launch configurations for retrieval of the asteroid 2009 BD, the total Δv required for the mission excluding the asteroid capture maneuvers is between 4000 m/s and 8700 m/s.[8]

To determine the lifetime requirements from the mission Δv, the spacecraft dry mass and propulsion system must be known. For the case of the ARM, a spacecraft dry mass of 4500 kg is a reasonable assumption.[8] For the propulsion system, let us use the Fakel SPT-100, arguably the most mature Hall thruster design available today. The SPT-100 is a 1.5 kW-class Hall thruster that uses xenon as a propellant and is capable of 1600 m/s specific impulse and 85 mN of thrust when operating at a discharge voltage of 300 V and a propellant mass flow rate of 5.2 mg/s.[9] Using these operating parameters, the total propellant mass required to complete the mission outlined above is given by

$$m_p = \frac{m_p}{m_0}\frac{m_0}{m_1}m_1 = m_1\left(\exp\left(\frac{\Delta v}{gI_{sp}}\right) - 1\right), \tag{1.7}$$

where m_1 is the spacecraft mass at the end of the mission, or if zero margin of error is assumed, the spacecraft dry mass. Assuming the minimum Δv requirement of 4000 m/s, this equation evaluates to about 1306 kg for the ARM. If the propulsion system consists of a single SPT-100, this translates to a required thruster lifetime of nearly 70,000 hours. The SPT-100 has only been validated for a lifetime of about 5700 hours,[10] so at least a dozen SPT-100 units would be required to complete this mission, and that is without any margin of error or system redundancy. Such factors may ultimately result in a greater increase in spacecraft mass than was saved in propellant to begin with. Hence, validating Hall thrusters for tens of thousands of hours of operation is of critical importance for their use on future missions.

The principal difficulties in validating a Hall thruster's operational life on the ground are the time and monetary investments involved. There is no theoretical barrier to operation of a general plasma thruster at atmospheric pressure, but the power density required to sustain such a plasma would be enormous, and thermal considerations would ultimately render such a thruster impractical. For Hall thrusters in particular, the increased collisionality at higher pressures would knock electrons off of the magnetic field lines, resulting in increased cross-field transport and changing the thruster's operating characteristics. Hence, Hall thrusters uniformly operate at a low plasma density, and must be tested in ground-based vacuum chambers. Moreover, the facility can have an effect on the thruster operation, so a larger facility is generally more desirable. Maintaining high vacuum conditions for several thousand hours in a large vacuum chamber is tremendously expensive. Thus, identifying and characterizing the life-limiting phenomena in Hall thrusters using analysis and modeling is considered an attractive alternative to ground-based life testing.

Historically, the primary life-limiting mechanism in Hall thrusters has been the erosion of the discharge channel walls. As ions from the discharge plasma strike the walls, they sputter atoms from the wall material. Over time, these accumulated sputtering events result in macroscopic erosion of the wall. Eventually, this process will expose the magnetic pole pieces and coils to the discharge plasma. Although the thruster may operate for some time once the magnetic circuit is exposed, the erosion of the pole pieces changes the magnetic field topography over time, altering the behavior of the thruster and ultimately resulting in failure. The erosion process also produces free material that may condense on thruster and spacecraft surfaces. Hence, this work seeks to characterize the fundamental sputtering process that underlies Hall thruster wall erosion, and then model the transport of the sputtering products through a Hall thruster in order to predict their behavior.

1.3 Thesis Outline

This work focuses on development of a model to calculate the erosion rate of the channel walls in a Hall thruster and then track the condensible products of erosion through the thruster via numerical simulation. Chapter II discusses the history of erosion modeling in Hall thrusters, including the modeling of the sputtering process itself and the modeling of Hall thruster plasma discharges. Chapter III describes the molecular dynamics model for sputtering. This model builds on previous work by

Yim[11,12] in order to characterize the steady-state sputtering of *h*-BN and to describe the behavior of the condensible erosion products. Chapter IV shows the results of the molecular dynamics model, including integrated sputter yields, differential sputter yields, and 3D velocity distribution functions of the condensible erosion products. Chapter V gives an overview of the Hall thruster plasma model, including the updates made to the ionization and erosion submodels. Chapter VI discusses the application of the plasma model to simulate a Hall thruster. The effects of the ionization updates are described, and the results of the material transport simulations are compared to experimental measurements. Finally, Chapter VII summarizes the findings and posits areas for future investigation.

CHAPTER II

Hall Thruster Erosion Modeling

The erosion of the discharge channel walls of a Hall thruster is a very slow process, requiring thousands of hours of thruster operation before the magnetic circuit is exposed to the plasma discharge. Traditionally, the operational life of Hall thrusters has been assessed by long-term operation of the thruster in ground-based vacuum chambers. One such test is the $\sim$ 5700-hour endurance test of the Fakel SPT-100.[10] This test determined that the most likely "hard" failure mechanism of the SPT-100 is electrical shorting between the cathode emitter and cathode ignitor. However, measured erosion profiles indicated that the outer channel wall of the SPT-100 was completely eroded after about 1000 hours of operation.[9] Another long-duration test was performed for the Aerojet BPT-4000 Hall thruster in the early 2000s.[13,14] This test demonstrated that the BPT-4000 is capable of at least 6750 hours of operation between 1 kW and 4.5 kW discharge power, and later predictions indicated that operation for several thousand more hours was possible before the magnetic circuit was exposed to the plasma.[15] However, the immense cost of these tests (on the order of a million US dollars) has led to various efforts to characterize Hall thruster wall erosion either empirically or through physics-based computer simulations.

Hall thruster erosion is the result of interactions between two physically disparate substances: the gaseous plasma discharge and the solid wall. The plasma serves as a source of energetic particles that bombard the wall, causing wall erosion, but the presence of the wall in turn alters the plasma properties. However, the timescale on which the plasma responds to the wall is much smaller than the time required for macroscopic erosion. Thus, two separate models can be used to approach the problem of Hall thruster erosion: a plasma model for computing the flux of ions to the channel walls and a model for the sputtering of the wall material under ion bombardment. By coupling these models, one can compute the wall erosion rate for a given thruster configuration, or even introduce new species corresponding to the erosion products into the plasma model.

2.1 Atomic Sputtering Models

The macroscopic erosion that occurs in Hall thrusters is the result of accumulated sputtering of the wall material under ion bombardment. Each time an ion strikes the wall, it deposits some of its energy into the wall material, initiating a collision cascade in the near-surface atoms. Occasionally, the collision cascade results in the ejection of one or more atoms or molecules from the surface. Under continuous ion bombardment, the cumulative sputtering events manifest as a recession of the surface away from the bulk plasma.

The sputtering of a material under ion bombardment is described by the sputter yield. For a given target material, this quantity is a function only of the mass, translational kinetic energy, and polar incidence angle of the impacting ions. In SPT-type Hall thrusters, the wall material is usually hexagonal boron nitride (h-BN) or some BN-based ceramic, and the propellant gas is usually xenon. Hence, this work will primarily focus on the sputtering of h-BN under bombardment by xenon ions.

The simplest form of the sputter yield is the total or integrated sputter yield, defined as the mean number of atoms ejected per incident ion:

$$Y = Y\left(\mathcal{E}_i, \theta_i\right) = \frac{N_{ejected}}{N_{ions}}. \tag{2.1}$$

Coupled with the number density and 3D velocity distribution (VDF) function of the ions in the plasma, this quantity is sufficient to determine the erosion rate of a surface under ion bombardment. However, the integrated sputter yield does not contain any information regarding the behavior of the ejected particles, and is thus insufficient for modeling material transport. To determine the outgoing trajectories of the sputtered particles, one can compute the differential sputter yield:

$$y\left(\mathcal{E}_i, \theta_i, \theta, \phi\right) = \frac{\partial}{\partial\Omega}\left(\frac{N_{ejected}\left(\theta, \phi\right)}{N_{ions}}\right) \tag{2.2}$$

where θ is the polar ejection angle of the sputtered particle relative to the surface normal, ϕ is the azimuthal angle of the sputtered particle's trajectory, and $N_{ejected}$ is the number of atoms passing through the differential element $d\Omega$ centered about θ and ϕ. One can recover the total sputter yield by integrating the differential sputter yield over solid angle space. Thus, the differential yield can be interpreted as a probability distribution function where $\left({}^{y}/_{Y}\right) d\Omega$ is the probability that a sputtered particle will pass through the differential element $d\Omega$ defined by θ and ϕ. Note, however, that the differential sputter yields do not provide any information regarding the speed of the sputtered particles. Such information is provided by the complete energy distribution function (EDF). The theoretical form for the EDF of sputtered particles is discussed briefly below, and a statistical method for determining the EDF is discussed in Chapter III.

In the past, the sputter yields of materials have been determined through means such as empirical fits to experimental measurements, theoretical or semi-empirical analyses, and numerical modeling. A brief overview of each of these techniques and some relevant results follow below.

2.1.1 Experimental Curve Fits

Perhaps the simplest means of evaluating the sputter yield of a material is to fit an empirical curve to experimental data. This method is commonly applied for multi-component crystalline materials such as boron nitride, where the theoretical description of sputtering is somewhat lacking. Consider, for example, the work of Garnier *et al.*,[16] which used a mass loss technique to measure the sputter yields of *h*-BN under xenon ion bombardment from 350 eV to 1 keV ion energy. Garnier recommends a linear fit to the experimental data for use in Hall thruster erosion modeling. In a Hall thruster, however, the majority of ions striking the walls are expected to have energies less than 100 eV. In order to extrapolate Garnier's data to the near-threshold regime, Manzella *et al.* applied a logarithmic fit to the data, assuming a threshold energy of 50 eV:[17]

$$Y_{\mathcal{E}_i}\left(\mathcal{E}_i\right) = 0.0346 \ln \mathcal{E}_i - 0.136. \tag{2.3}$$

The angular dependence is then found from a quartic fit to Garnier's data:

$$\begin{aligned} \hat{Y}_{\theta_i}\left(\theta_i\right) \equiv \frac{Y\left(\theta_i\right)}{Y\left(0\right)} &= -1.89 \times 10^{-7}\theta_i^4 + 2.04 \times 10^{-5}\theta_i^3 \\ &\quad - 3.77 \times 10^{-4}\theta_i^2 + 1.85 \times 10^{-3}\theta_i + 0.426. \end{aligned} \tag{2.4}$$

Then, given the angular distribution $f\left(\theta_i\right)$ and energy distribution $g\left(\mathcal{E}_i\right)$ of the ions, the total sputter yield is given by

$$Y\left(\mathcal{E}_i, \theta_i\right) = f\left(\theta_i\right) \hat{Y}_{\theta_i}\left(\theta_i\right) \cdot g\left(\mathcal{E}_i\right) Y_{\mathcal{E}_i}\left(\mathcal{E}_i\right). \tag{2.5}$$

The resulting erosion profile calculations for the SPT-100 Hall thruster show good agreement with experimental measurements near the thruster exit plane, but the calculations clearly underestimate the erosion rate several millimeters upstream of the exit, where the bombarding ions have lower energies. This is a result of the considerable uncertainty in the logarithmic extrapolation to lower ion energies, and the uncertainty of boron nitride sputter yields in the near-threshold regime in general. Without accurate measurements or calculations of the BN sputter yields near threshold, empirical fits to experimental data will always have a high degree of uncertainty.

2.1.2 Theoretical and Semi-Empirical Analysis

The theoretical description of atomic sputtering largely comes from the work of Sigmund.[18,19] Consider a semi-infinite, amorphous, monatomic solid with a plane surface at $x = 0$. A bombarding ion with arbitrary velocity $\mathbf{v}$ ($\mathbf{v} \cdot \hat{\mathbf{x}} = v_x > 0$) strikes the surface at time $t = 0$. Sigmund defines the function

$$G(x, \mathbf{v}_0, \mathbf{v}, t) d\mathbf{v}_0 dx \tag{2.6}$$

as the number of atoms moving at time t within a differential layer $(x, x + dx)$ with velocity $(\mathbf{v}_0, \mathbf{v}_0 + d\mathbf{v}_0)$. Similarly, the number of atoms with velocity $(\mathbf{v}_0, \mathbf{v}_0 + d\mathbf{v}_0)$ penetrating the plane at x in a time interval dt is given by

$$G(x, \mathbf{v}_0, \mathbf{v}, t) d\mathbf{v}_0 \left| v_{0x} \right| dt. \tag{2.7}$$

The sputter yield is simply the total number of atoms to pass through the surface at $x = 0$ over all time, calculated as

$$Y = \int_{-\infty}^{-v_{min}} \int_{-\infty}^{\infty} \int_{-\infty}^{\infty} \int_{0}^{\infty} G\left(0, \mathbf{v}_0, \mathbf{v}, t\right) \left| v_{0x} \right| dt dv_{0z} dv_{0y} dv_{0x}, \tag{2.8}$$

where v_{min} is the minimum velocity magnitude required to overcome the surface binding forces. Thus, to determine the sputter yield, one need only find a solution for the function $G\left(x, \mathbf{v}_0, \mathbf{v}, t\right)$.

Sigmund's solution for G falls within the linear cascade regime and makes several assumptions.[18] First, all collisions are assumed to be binary in nature. Second, the presence of the free surface at $x = 0$ is neglected. Instead, the solid is treated as an infinite medium. It is also assumed that only the bombarding ion has a finite velocity at $t = 0$, i.e.:

$$G\left(x, \mathbf{v}_0, \mathbf{v}, t = 0\right) = \delta\left(x\right)\delta\left(\mathbf{v} - \mathbf{v}_0\right), \tag{2.9}$$

where $\delta\left(x\right)$ is the Dirac delta function. In the limit of $t \to \infty$, it is assumed that all particles slow down to zero velocity:

$$G\left(x, \mathbf{v}_0, \mathbf{v}, t \to \infty\right) = 0. \tag{2.10}$$

Finally, in the presence of a planar potential energy barrier at the surface and for low ion energies ($< 1\,\mathrm{keV}$), a solution of the linearized Boltzmann equation gives an expression for the integrated sputter yield:[19]

$$Y\left(\mathcal{E}_i, \theta_i\right) = \frac{3}{4\pi^2}\frac{4 m_i m_a}{\left(m_i + m_a\right)^2}\frac{\mathcal{E}_i \alpha}{U_b}, \tag{2.11}$$

where m_i is the ion mass, m_a is the molecular mass of the target material, U_b is the surface binding energy, and α is a nondimensional function of the mass ratio ${}^{m_i}/_{m_a}$ and the ion incidence angle θ. In the limit of $m_i \gg m_a$ and $\theta_i = 0$, $\alpha \approx 0.15$ and the sputter yield becomes

$$Y\left(\mathcal{E}_i\right) = \frac{0.45}{\pi^2}\frac{m_a}{m_i}\frac{\mathcal{E}_i}{U_b}. \tag{2.12}$$

So, the integrated sputter yield is a linear function of the ion energy. This formula is subject to considerable uncertainty. Namely, the validity of the binary collision approximation at low energies is questionable, and the elastic collision cross-sections between the ion and the surface atoms are not well known. Sigmund claims[18] that the linear relationship is valid down to ion energies “somewhat below 100 eV” for heavier ions based on experimental evidence. However, the exact energy range in which the linear relationship is valid is unknown.

Sigmund’s theory also predicts the energy distribution function of the sputtered atoms.[19] For normal ion incidence:

$$f\left(\mathcal{E},\theta\right) \propto \frac{\mathcal{E}}{\left(\mathcal{E}+U_b\right)^{3-2m}} \left|\cos\theta\right|, \tag{2.13}$$

where θ is the polar ejection angle of the sputtered particles, as in Eq. 2.2. This function is called the Sigmund-Thompson distribution, having been derived independently by both Sigmund and Thompson.[20] The parameter m is, in general, a function of both $\mathcal{E}_i$ and $\mathcal{E}$. Sigmund posits that in the limit of $\mathcal{E}_i \gg \mathcal{E}$, $m = m\left(\mathcal{E}\right)$ only. However, this conflicts with the assumption that the energy of the incident ion is small. Betz and Wien, in contrast, argue that m is a function of $\mathcal{E}_i$ only.[21] For the purposes of this work, the approach of Betz and Wien is taken and m is treated as a function of $\mathcal{E}_i$ only.

Equation 2.11 is a limiting form of the more general expression

$$Y\left(\mathcal{E}_i\right) = 0.042\frac{\alpha S_n\left(\mathcal{E}_i\right)}{U_b}, \tag{2.14}$$

where S_n is the nuclear stopping power,[18,19] which is not well known in general. Bohdansky[22] used a semi-empirical approach to modify Eq. 2.14 to better match experimental data in the near-threshold regime:

$$Y\left(\mathcal{E}_i\right) = \alpha S_n\left(\mathcal{E}_i\right)\left[1-\left(\frac{E_{th}}{\mathcal{E}_i}\right)^{2/3}\right]\left[1-\frac{E_{th}}{\mathcal{E}_i}\right]^2. \tag{2.15}$$

This form introduces the threshold energy for sputtering, E_{th}. In the near-threshold energy regime, Bohdansky argues that the energy dependence of S_n is negligible compared to the other terms, and S_n can thus be treated as a constant. Similarly, for normal ion incidence and $m_i \gg m_a$, α is also constant, so Eq. 2.15 can be fit to experimental data with αS_n and E_{th} behaving as free fit coefficients.

Matsunami *et al.* also modified Eq. 2.14,[23] finding a form similar to the Bohdansky function:

$$Y\left(\mathcal{E}_i\right) = 0.042 \frac{\alpha S_n\left(\mathcal{E}_i\right)}{U_b}\left[1-\left(\frac{E_{th}}{\mathcal{E}_i}\right)^{1/2}\right]. \tag{2.16}$$

Compared to Eq. 2.14, this form matches experimental measurements of sputter yields over a wider range of energies, but does not perform as well in the near-threshold regime as the Bohdansky function. Yamamura and Tawara[24] later adapted the Matsunami form for high-energy sputtering by light ions:

$$Y\left(\mathcal{E}_i\right) = 0.042 \frac{\alpha}{U_b} \frac{S_n\left(\mathcal{E}_i\right)}{1+\Gamma s_e\left(\epsilon\right)/s_n\left(\epsilon\right)}\left[1-\left(\frac{E_{th}}{\mathcal{E}_i}\right)^{1/2}\right]^{s}, \tag{2.17}$$

where s_e and s_n are the reduced electronic stopping power and reduced nuclear stopping power, respectively, and the parameter Γ is a function of the ion mass. For heavy ions and low ion energies, Γs_e is very small and Eq. 2.16 can be recovered by setting $s = 1$.

A simplified form of Eq. 2.17 has been used to model Hall thruster erosion:

$$Y\left(\mathcal{E}_i\right) = S\left(\mathcal{E}_i\right) \times A\left[1-\left(\frac{E_{th}}{\mathcal{E}_i}\right)^{1/2}\right]^{2.5}, \tag{2.18}$$

where the form of $S\left(\mathcal{E}_i\right)$ varies. In the work of Cheng and Martínez-Sánchez,[25] it takes the form

$$S\left(\mathcal{E}_i\right) = \frac{\mathcal{E}_i^{0.474}}{1+B\mathcal{E}_i^{0.3}}, \tag{2.19}$$

with A and B acting as free fit parameters. Other works[15,26] use the form:

$$S\left(\mathcal{E}_i\right) = \sqrt{\mathcal{E}_i}, \tag{2.20}$$

with A acting as the sole fit coefficient.

All of the above analyses have focused on the energy dependence of the sputter yield. However, the angular dependence has also been investigated. Assuming Rutherford scattering collisions, Sigmund derived the expression[18]

$$\hat{Y}\left(\theta_i\right) \equiv \frac{Y\left(\theta_i\right)}{Y\left(0\right)} \approx \left(\cos\theta_i\right)^{-0.94}, \tag{2.21}$$

so long as θ_i is not too large. This expression is very similar to the common inverse cosine model of the angular yield dependence, but depends on the assumption of Rutherford scattering and is only valid for light ions. Sigmund's expression and the inverse cosine form also perform very poorly at oblique angles of incidence ($\theta_i \to 90°$). In order to capture the angular dependence of the sputter yields even at oblique incidence, Yamamura proposed an empirical relation for sputtering by heavy ions:[27]

$$\hat{Y}\left(\theta_i\right) = \cos^A\left(\theta_i\right)\exp\left[-B\left(\frac{1}{\cos\left(\theta_i\right)} - 1\right)\right]\left[\frac{1 - \sqrt{\frac{E_Y}{\mathcal{E}_i}}\cos\left(\theta_i\right)}{1 - \sqrt{\frac{E_Y}{\mathcal{E}_i}}}\right] \tag{2.22}$$

where A, B, and E_Y behave as fitting coefficients.

Zhang and Zhang[28,29] expanded upon the work of Sigmund and Yamamura to find a form for the differential sputter yield:

$$
\begin{aligned}
y\left(\mathcal{E}_i,\theta_i,\theta,\phi\right) &= 0.042\frac{\alpha S_n}{U_b}\times\frac{\cos\left(\theta\right)}{\pi} \qquad (2.23)\\
&\times\left[1-\frac{1}{4}\sqrt{\frac{E^*}{\mathcal{E}_i}}\left(\cos\left(\theta_i\right)\psi\left(\theta\right)+\frac{3\pi}{2}\sin\left(\theta_i\right)\sin\left(\theta\right)\cos\left(\phi\right)\right)\right],\\
\psi\left(\theta\right) &= \frac{3\sin^2\left(\theta\right)-1}{\sin^2\left(\theta\right)}+\frac{\cos^2\left(\theta\right)\left(3\sin^2\left(\theta\right)+1\right)}{2\sin^3\left(\theta\right)}\ln\left(\frac{1+\sin\left(\theta\right)}{1-\sin\left(\theta\right)}\right). \qquad (2.24)
\end{aligned}
$$

After integrating over solid angle space, the total sputter yield is found as

$$
Y\left(\mathcal{E}_i,\theta_i\right)=0.042\frac{\alpha S_n}{U_b}\left[1-\left(\frac{E^*}{\mathcal{E}_i}\right)^{1/2}\cos\theta_i\right], \qquad (2.25)
$$

which closely resembles the form described by Matsunami *et al.*, Eq. 2.16, only with the angular dependence included.

2.1.3 Numerical Modeling

A third approach to determining the sputter yields of *h*-BN is physics-based numerical modeling. Whereas theoretical analysis must often make numerous assumptions in order to make a problem tractable, a numerical model can approach the same problem with fewer assumptions by approximating the solution through discretization of the governing equations, stochastic treatment of some processes, or other means. Numerical models are also very useful for isolating specific physical processes, something that is often very difficult to do experimentally.

The sputtering of solids is an atomistic, collisional process. Thus, it is necessary that any numerical model of sputtering resolve the particle collisions in some way. Three common methods for resolving the particle collisions are:

1. Binary collision approximation (BCA): Collisions are assumed to be binary in nature and obey a set of collision cross-sections. Each collision is treated

stochastically such that momentum and energy are conserved. Between collisions, particles move according to a discretized equation of motion.

2. Molecular dynamics (MD): Particles are assumed to behave classically and interact through continuous interatomic potential energy functions. The equations of motion are discretized in time, and the forces between particles are derived from the interatomic potentials.
3. Quantum or semi-classical methods: The quantum interactions between atoms are either fully or partially resolved, giving rise to interatomic forces.

The quantum methods include techniques such as density functional theory (DFT).[30] These methods are, in general, higher-fidelity than the binary collision and MD techniques, but incur an extraordinary computational cost, and are often limited to systems consisting of no more than a few atoms. For that reason, quantum methods are not considered a viable tool for modeling *h*-BN sputtering.

2.1.3.1 Binary Collision Approximation

As its name implies, the core assumption of the binary collision approximation is that all collisions can be modeled as interactions between two bodies only. This approximation lends itself well to the Monte Carlo method, in which collisions are treated stochastically according to a prescribed set of collision cross-sections. One implementation of the Monte Carlo method with BCA is the SRIM package, "The Stopping and Range of Ions in Matter."[31] This code has been applied to study the sputtering of both single-[32] and multi-component[33] materials. It has also been applied to simulate the sputtering of *h*-BN under argon ion bombardment.[34] However, there are no known instances of SRIM being applied to simulate the sputtering of *h*-BN by xenon ions.

One limitation of the BCA method with regards to sputtering studies is that it requires prior knowledge of the surface binding energy U_b. If the binding energy is not known, it must be treated as an input parameter and adjusted until the desired output is achieved. In the work of Chen *et al.*,[34] it was found that the calculated sputter yields were highly sensitive to the specified binding energy. A value between 2 eV and 3 eV was found to give the best results, but there is now experimental evidence that the surface binding energy of boron in *h*-BN is closer to 5 eV.[35,36] It is possible that the binding energy of nitrogen in *h*-BN is substantially smaller than that of boron, but given the available evidence, it appears that the binary collision approximation may not capture all of the physics relevant to sputtering of *h*-BN.

2.1.3.2 Molecular Dynamics

Molecular dynamics (MD)[37,38] is a deterministic technique for simulating atomic-scale systems and is strongly analogous to the N-body problem of orbital mechanics. Atoms are treated as classical particles with some position in space. These atoms interact with one another through analytical potential functions. At each time step, the net force acting on each atom from all other atoms is calculated. Then, the position and velocity of each atom are integrated numerically in time according to the laws of classical mechanics, leading to a new system state. Any desired macroscopic parameters, such as the system temperature, are computed from statistical averages of the particle properties. This process is then repeated until the desired level of uncertainty in the macroscopic quantities is reached. If the selected interatomic potentials are physically appropriate, then a time-accurate view of the particle dynamics and average system properties can be achieved.

Although the MD model itself is quite simple, its implementation introduces several challenges. First, for each species-pairing present in the system, a completely different interatomic potential may be required. In addition, the time step required to resolve the atomic motion through those potentials may be much smaller than the time scale of the process being investigated. In the particular case of sputtering, a large number of individual impact events may be needed in order to gather sufficient statistics for calculating the sputter yields. The domain sizing also presents a problem, as the *h*-BN lattice must be large enough to dissipate the energy introduced by the bombarding ion without being so large as to make the simulation intractable.

Many of the problems listed above were addressed by Yim, who previously applied the MD method to study the sputtering of *h*-BN by xenon ions.[11,12] Yim demonstrated the feasibility of this approach, but was severely limited by the computational power available. His most extensive simulation case consisted of only 1500 ion impact events, but recent work has shown[39] that tens of thousands of ion impacts may be required to reach steady-state conditions in these simulations. Yim was also unable to resolve the differential sputter yields or the VDFs of the sputtered particles, as the limited number of impact events directly resulted in limited statistical samples for those quantities.

The present work seeks to build on the work of Yim and develop an updated, high-speed MD model for the sputtering of *h*-BN. Namely, the goal is to resolve both the total and differential sputter yields of *h*-BN under steady-state conditions, and to resolve the velocity distribution functions of the condensible products of sputtering. These data can then be coupled to a Hall thruster plasma model in order to calculate the wall erosion rates and to model the transport of condensible materials through the thruster and plume.

2.2 Hall Thruster Plasma Models

Even if the boron nitride sputter yields are well known, the flux and energy distribution of ions striking the thruster walls must be known in order to accurately compute the erosion rate. Hence, a model of the plasma discharge is required. The goal of any plasma model is to solve the governing equations for the electrons, ions, and neutral atoms in the plasma with appropriate boundary conditions. In practice, a complete solution of the system is often intractable, so limiting assumptions are made and some mathematical terms are neglected in order to acquire a more approximate solution.

Several techniques for numerical modeling of plasmas have been developed over the years, ranging in application from nuclear fusion to semiconductor manufacturing. However, these models can generally be grouped into one of two types: continuum models and kinetic models. These techniques are separated based on the physical regime of the problem, defined by the Knudsen number:

$$Kn = \frac{\lambda_{\mathrm{mfp}}}{L}, \tag{2.26}$$

where λ_{mfp} is the mean free path of the gas or plasma and L is a characteristic length scale. For very small Kn, the continuum approximation is valid, but at intermediate and large Kn, the kinetic, non-equilibrium effects become important.

The continuum and kinetic methods each have their own advantages and disadvantages, and each have been applied to simulate Hall thrusters at some point in the past. Below is a brief summary of the two techniques and an overview of their advantages and disadvantages with regard to erosion modeling.

2.2.1 Continuum Models

Continuum or fluid models treat the plasma species as one or more continua that obey the conservation laws of fluid dynamics, i.e. continuity, momentum conservation, and energy conservation. The fundamental assumption of such methods is that the plasma is sufficiently collisional that any perturbations from a Maxwell-Boltzmann velocity distribution are small, thus making non-equilibrium effects negligible. Inelastic collisions such as electron impact ionization are treated as source and sink terms in the conservation equations for each species.

An example of a modern continuum model for Hall thruster plasmas is Hall2De.[40] Hall2De solves the fluid conservation laws for ions, neutral atoms, and electrons on a 2D axisymmetric mesh that is aligned with the applied magnetic field. By aligning the mesh with the magnetic field, the pronounced anisotropy induced by the magnetic field can be modeled in a largely self-consistent manner. Hall2De simulations were previously used to identify the fundamental physics behind magnetic shielding,[41,42] a novel technique for mitigating the erosion of the discharge channel walls in a Hall thruster. A magnetically-shielded Hall thruster is currently being developed as part of NASA's Asteroid Redirect Mission,[43] and Hall2De simulations are being used to guide the design.

The key advantage of continuum models is their low computational cost relative to kinetic methods. However, they are incapable of capturing many non-equilibrium effects that may manifest in the thruster plasma. In particular, a purely continuum model may not perform well for modeling material transport in a Hall thruster, as the products of wall erosion are highly rarefied and do not follow a Maxwell-Boltzmann VDF. Hence, a continuum model is not considered adequate for the present work, wherein capturing the behavior of the erosion products is one of the principal goals.

2.2.2 Kinetic Models

Kinetic models differ from continuum models in that they make no assumptions about the velocity distributions of the simulated species. Thus, kinetic simulations are capable of fully capturing non-equilibrium effects. Kinetic models can be further broken down into two types: particle-based methods and Boltzmann solvers. Particle-based methods treat the plasma component species as numerical macroparticles, also called superparticles. Each macroparticle behaves like a finite cloud consisting of many real particles. The macroparticles move freely, and macroscopic properties are calculated by interpolating the particle properties onto a mesh. Inter-particle collisions are typically assumed to follow the binary collision approximation and are treated in a stochastic manner such that momentum and energy are conserved.

A common particle-based technique for simulating neutral gases is the direct simulation Monte Carlo (DSMC) method.[44] In DSMC, elastic collisions are modeled using a set of differential collision cross-sections, allowing anisotropic scattering of the colliding macroparticles. The time scale of the collisions is assumed to be very small, so the velocity of each colliding particle is changed instantaneously. Dragnea *et al.* previously applied the DSMC code MONACO to model the transport of boron eroding from the walls of the SPT-70 Hall thruster,[45,46] but there was considerable uncertainty associated with the simulations. Namely, because the plasma was not modeled, the ion wall flux and wall erosion rate could not be computed dynamically. Instead, the erosion rate, which was not exactly known, was used as an input to the model. Modeling the plasma would allow the wall erosion rate—and thus the boron production rate—to be calculated dynamically as the simulation runs, removing the need to provide an erosion rate to the simulation.

A particle-based method for modeling plasma flows is the particle-in-cell (PIC) technique.[47,48] The electrostatic version of the PIC method computes the charge density from the average charge interpolated from the macroparticles onto the numerical mesh. Then, the plasma potential is computed from the Poisson equation. The electric field is computed from the first derivative of the plasma potential and is then interpolated from the mesh back onto the macroparticles. The particle equations of motion are then integrated in time by one time step and the process is repeated. The effects of steady magnetic fields are easily modeled using the well known Boris integration method. Collisions can also be included, and are frequently modeled using the DSMC technique described above, resulting in a so-called DSMC-PIC model.

PIC and DSMC-PIC simulations have the advantage of capturing non-equilibrium effects, as noted above. This is particularly important when modeling wall erosion and material transport in Hall thrusters because the erosion products express non-equilibrium behavior. However, because such simulations utilize a finite number of macroparticles, there is always some statistical noise present in the macroscopic quantities. This is particularly relevant when studying plasma oscillations, as the noise may interfere with or completely mask real oscillations in the plasma. Full PIC methods are also extraordinarily expensive because they must resolve the temporal and spatial scales of the plasma, namely the plasma frequency and the Debye length. These requirements can be loosened by artificially increasing the electron mass and free-space permittivity, but such techniques also influence the plasma behavior. Thus, a purely PIC-based model is considered infeasible for the present work.

The second major class of kinetic methods is the Boltzmann or Vlasov solvers. As the name suggests, these methods seek to solve the Boltzmann equation directly:

$$\frac{\partial g}{\partial t} + \mathbf{v} \cdot \frac{\partial g}{\partial \mathbf{r}} + \frac{\mathbf{F}}{m} \cdot \frac{\partial g}{\partial \mathbf{v}} = I, \tag{2.27}$$

where $g\left(\mathbf{r}, \mathbf{v}, t\right)$ is the phase-space probability distribution function and I is the collision integral. Boltzmann solvers avoid the statistical noise associated with particle simulations, but introduce other difficulties. First, the Boltzmann equation contains both integral and differential terms, making it very difficult to solve either analytically or numerically. Second, Boltzmann solvers require discretization of 7 different dimensions to find a complete 3D solution: 3 dimensions in physical space, 3 in velocity space, and 1 in time. These aspects make Boltzmann solvers very computationally expensive, often limiting their applications to one- or two-dimensional phenomena.

Recently, Hara developed a 1D1V (1 dimension in space, 1 dimension in velocity space) Boltzmann solver and studied numerous plasma phenomena, including some nonlinear plasma waves.[49] A simulation of nonlinear Landau damping shows that the Boltzmann solver achieves numerical convergence even for a relatively coarse discretization of velocity space, whereas a PIC model fails to achieve convergence given the same number of degrees of freedom. Hara's Boltzmann solver was also used to analyze a trapped particle instability and shows excellent agreement with theoretical predictions.[50] Just as with PIC methods, however, modeling a Hall thruster plasma with a Boltzmann solver is an intractable problem due to the prohibitive computational cost. Thus, alternative modeling techniques are necessary to approach the problem of wall erosion and material transport in Hall thrusters.

2.2.3 Hybrid Models

The majority of plasma models developed in the Hall thruster community utilize a hybrid technique. These methods mitigate the computational cost of the simulations by modeling the electrons as a fluid, but model the ions and neutral atoms kinetically to capture some of the non-equilibrium effects in those species. The continuum and kinetic submodels are linked through assumptions such as quasineutrality to ensure that the models are physically consistent. The hybrid simulation then proceeds by repeatedly iterating between the two submodels. In the context of wall erosion and material transport, hybrid models have the distinct advantage of modeling the highly-rarefied erosion products kinetically without incurring the large computational cost associated with fully kinetic models.

Many hybrid plasma models have been developed in the Hall thruster community, most notably the so-called hybrid-PIC models.[51,52] These models treat ions and neutrals using the PIC method, and couple the PIC and electron submodels by assuming quasineutrality. Among the most well-established hybrid-PIC models is the axial-radial code HPHall,[51] notable for providing some of the earliest evidence of the physical mechanisms behind the low-frequency breathing mode that occurs in Hall thrusters.[53] More recently, Hara developed a hybrid fluid-Boltzmann solver to study plasma oscillations and mode transitions in Hall thrusters.[49,54,55] However, Hara's hybrid model is an axial-azimuthal model, which is inadequate for modeling processes such as wall erosion in which the radial direction is critical. Hence, the axial-radial model HPHall is chosen as the plasma model for use in the present work.

HPHall has been utilized to model Hall thruster wall erosion several times in the past,[15,25,26,56] but does not have the capability to introduce any erosion products into the simulation domain as of the start of the present work. Hence, this work seeks to add additional species to HPHall corresponding to the condensible products of the wall erosion process. The *h*-BN sputter yields and the initial conditions for the erosion products will be based on the results of the molecular dynamics model. HPHall will then be used to simulate a Hall thruster and track the erosion products into the near-field plume. Finally, the density of the erosion products will be compared to experimental measurements where data are available.

CHAPTER III

Molecular Dynamics Sputtering Model

This chapter describes the model for the sputtering of *h*-BN by xenon ions. This model employs the molecular dynamics (MD) technique, a deterministic method for analyzing the dynamics of atomic-scale systems. The MD model used in this work is largely based on the work of Yim,[11,12] who previously demonstrated the feasibility of MD modeling for boron nitride sputtering.

Although MD is relatively inexpensive for an atomistic technique, it still incurs a hefty computational cost. Thus, rather than developing a new code package from scratch, it was determined early on that the sputtering model should be implemented in an existing MD framework with massively parallel processing capabilities. The MD package ultimately chosen for use in this work is the Highly-Optimized Object-Oriented Molecular Dynamics suite, blue edition,[57] or simply HOOMD-blue. HOOMD-blue is a modular MD framework that utilizes Nvidia's CUDA technology[58] to perform parallel calculations on graphics processing units (GPUs). In contrast with CPUs, GPUs typically consist of a few hundred to a few thousand relatively low-power computing cores specialized for floating-point calculations. They are well-suited to tasks wherein each item of a large data set must undergo the same set of operations, such as in MD. For a polymer system of about 64,000 atoms, calculations performed on a single Nvidia Tesla K40 workstation GPU have been shown to run an order of magnitude faster than on a 10-core Intel Xeon E5-2680 v2 processor.[*] However, the MSRP of the K40 GPU is less than twice that of the 10-core processor, making GPU computing very cost-effective. It is for this reason that HOOMD-blue is chosen as the MD code package for this work.

3.1 Governing Equations

3.1.1 Newton's Second Law

The motion of the atoms in the MD domain is governed by Newton's second law. For a particle i of constant mass, this is written as

$$\sum_{j \neq i} \mathbf{F}_{ij} = m_i \frac{d^2 \mathbf{r}_i}{dt^2} = m_i \frac{d\mathbf{v}_i}{dt}, \tag{3.1}$$

where $\mathbf{F}_{ij}$ is the force exerted on particle i by particle j. The force on particle i from those particles j is determined from an interatomic potential function Φ as

$$\mathbf{F}_{ij} = -\nabla_{\mathbf{r}_i} \Phi \left(\mathbf{r}_i, \mathbf{r}_j \right). \tag{3.2}$$

Note the subscript $\mathbf{r}_i$ on the gradient. This denotes that the potential is differentiated with respect to the position of particle i. Conversely, the force on particle j is computed as

$$\mathbf{F}_{ji} = -\nabla_{\mathbf{r}_j} \Phi \left(\mathbf{r}_i, \mathbf{r}_j \right). \tag{3.3}$$

This distinction becomes important when the potential function includes the effects of tertiary particles k.

---

[*] According to benchmarks section of the HOOMD-blue webpage: `http://codeblue.umich.edu/hoomd-blue`. Accessed 23 July 2015.

3.1.1.1 Velocity Verlet Scheme

In order to integrate Eq. 3.1 in time, it must first be discretized. The finite difference scheme used in the present work is the second-order Velocity Verlet technique:[59]

$$\mathbf{r}\left(t+\Delta t\right)=\mathbf{r}\left(t\right)+\mathbf{v}\left(t\right)\Delta t+\frac{1}{2}\mathbf{a}\left(t\right)\Delta t^{2}, \tag{3.4}$$

$$\mathbf{v}\left(t+\Delta t\right)=\mathbf{v}\left(t\right)+\left(\frac{\mathbf{a}\left(t+\Delta t\right)+\mathbf{a}\left(t\right)}{2}\right)\Delta t, \tag{3.5}$$

where $\mathbf{a}$ is the particle acceleration, which is determined from the interatomic potential functions and is thus a function of the particle positions only. The Velocity Verlet method is mathematically identical to the common leapfrog method when updating the particle position. However, the Velocity Verlet method has the advantage of recording the position and velocity of each particle at the same point in time, whereas the leapfrog method requires position and velocity to be offset by half of a time step. In HOOMD-blue, the Velocity Verlet integration is split into two steps with the force calculation taking place in between:

1. The particle positions are integrated one full time step according to Eq. 3.4. The particle velocities are integrated by half of a time step as $\mathbf{v}\left(t+\frac{\Delta t}{2}\right)=\mathbf{v}\left(t\right)+\frac{\mathbf{a}(t)}{2}\Delta t$.

2. The force on each particle is calculated as a function of the particle positions to determine $\mathbf{a}\left(t+\Delta t\right)$.

3. The velocity of each particle is integrated by another half of a time step according to $\mathbf{v}\left(t+\Delta t\right)=\mathbf{v}\left(t+\frac{\Delta t}{2}\right)+\frac{\mathbf{a}(t+\Delta t)}{2}\Delta t$.

Thus, Eq. 3.5 is recovered without storing the particle acceleration at two separate points in time.

3.1.2 Interatomic Potential Functions

In order to adequately model the sputtering of *h*-BN by xenon ions, two potential functions are required. The first describes the covalent bonds between the boron and nitrogen atoms in the lattice. The second describes the interactions between the bombarding xenon ion and the lattice atoms. In principle, atoms may interact according to these potential functions even at very large distances. In MD, however, the maximum range at which atoms interact is limited in order to reduce the computational cost of the simulations. This is accomplished by modifying the potential with a cutoff function, as described below.

3.1.2.1 Boron Nitride Potential Function

The potential used to model the covalently-bonded boron and nitrogen atoms is the Tersoff-like Albe-Möller potential[60,61]. This is a bond-order potential of the form

$$\begin{aligned} \Phi_{AM}\left(\mathbf{r}_i, \mathbf{r}_j, \mathbf{r}_{k\neq i,j}\right) &= \frac{1}{2} f_C\left(r_{ij}\right)\left[f_R\left(r_{ij}\right) - b_{ij}\left(\mathbf{r}_i, \mathbf{r}_j, \mathbf{r}_{k\neq i,j}\right) f_A\left(r_{ij}\right)\right], \\ r_{ij} &= \left|\mathbf{r}_j - \mathbf{r}_i\right|. \end{aligned} \tag{3.6}$$

The cutoff function $f_C(r)$ is a critical component of the Albe-Möller potential, appearing both within the function itself and as a modifying factor for the overall potential. In this work, the cutoff function takes the form

$$\begin{aligned} f_C(r) &= \begin{cases} 1, & r \leq R - D \\ \exp\left(\dfrac{\alpha \hat{r}^3}{\hat{r}^3 - 1}\right), & R - D < r < R + D \\ 0, & r \geq R + D \end{cases}, \\ \hat{r} &= \frac{r - (R - D)}{2D}. \end{aligned} \tag{3.7}$$

This form was initially proposed by Bazant *et al.*[62] and later used by Yim with

$\alpha = 3^{11,12}$, where the magnitude of the local minimum of the first derivative is minimized. This contrasts with the sine-based form used by Albe *et al.*, given by

$$f_C\left(r\right) = \begin{cases} 1, & r \leq R - D \\ \dfrac{1}{2} - \dfrac{1}{2}\sin\left(\pi\dfrac{r-R}{2D}\right), & R - D < r < R + D \\ 0, & r \geq R + D \end{cases}, \tag{3.8}$$

For this work, the exponential-based cutoff function is used in place of the sine-based function because it is continuous in both the first and second derivative at $r = R \pm D$. These properties are desirable in MD, where the force is calculated from the first derivative of the potential function. The value of α used in the present work is 3, the same as that used by Yim.

The repulsive and attractive components of the potential, f_R and f_A in Eq. 3.6, each take the form of a Morse potential:

$$f_R\left(r\right) = \frac{D_0}{S-1}\exp\left(-\beta\sqrt{2S}\left(r - r_0\right)\right), \tag{3.9}$$

$$f_A\left(r\right) = \frac{SD_0}{S-1}\exp\left(-\beta\sqrt{2/S}\left(r - r_0\right)\right). \tag{3.10}$$

The coefficient b_{ij} in Eq. 3.6 is a modifier to the attractive term that takes into account factors such as the number of bonded neighbors, bond angles, and the relative distance of bonded neighbors. It takes the form:

$$b_{ij}\left(\mathbf{r}_i, \mathbf{r}_j, \mathbf{r}_{k\neq i,j}\right) = \left[1 + \left(\gamma\chi_{ij}\left(\mathbf{r}_i, \mathbf{r}_j, \mathbf{r}_{k\neq i,j}\right)\right)^n\right]^{-1/2n}, \tag{3.11}$$

$$\chi_{ij}\left(\mathbf{r}_i, \mathbf{r}_j, \mathbf{r}_{k\neq i,j}\right) = \sum_{k\neq i,j} f_C\left(r_{ik}\right) g\left(\theta_{ijk}\right) \exp\left(\lambda^3\left(r_{ij} - r_{ik}\right)^3\right), \tag{3.12}$$

$$g\left(\theta_{ijk}\right) = 1 + \frac{c^2}{d^2} - \frac{c^2}{d^2 + \left(h - \cos\theta_{ijk}\right)^2}. \tag{3.13}$$

Here, the variable χ_{ij} introduces the effects of tertiary particles k. When such par-

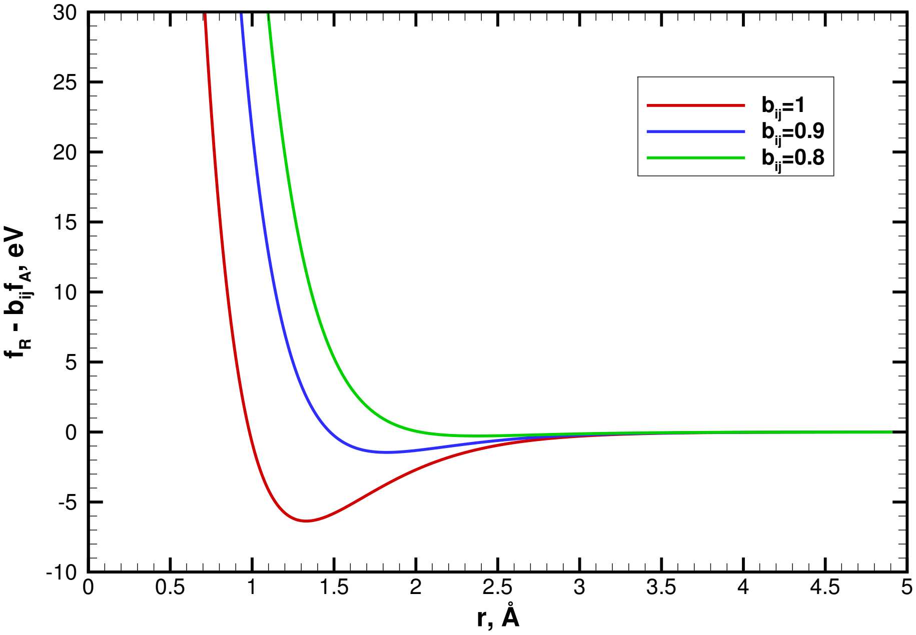

Figure 3.1: Example Albe-Möller potential profiles for different values of b_{ij}.

ticles are present, the bond angle θ_{ijk}, defined as the angle between $\mathbf{r}_{ij}$ and $\mathbf{r}_{ik}$, is controlled by $g(\theta_{ijk})$ with the equilibrium bond angle determined by h. The parameter λ determines how much the tertiary particle k affects the bond between particles i and j. For $r_{ij} \ll r_{ik}$, $\chi_{ij} \approx 0$ and $b_{ij} \approx 1$, so the attractive force between i and j is unaffected. For $\lambda > 0$ and $r_{ij} \gg r_{ik}$, χ_{ij} is very large and $b_{ij} \approx 0$, so the attractive force between particles i and j is greatly reduced. To illustrate this, a few potential profiles for different values of b_{ij} are shown in Fig. 3.1.

The Albe-Möller parameter values for each species pairing are given in Table 3.1. Note that the values of c and d for B–B bonds differ from those initially proposed by Albe and Möller. The original values cause B–B bonds to be extremely sensitive to the bond angle θ_{ijk}. Thus, in order to resolve the particle motion, a very small time step must be used in the numerical simulations. Yim found alternative values of c and d that maintained the same ratio ${}^{c^2}/_{d^2}$ while reducing the sensitivity of B–B bonds to bond angles.[11,12] The function $g(\theta_{ijk})$ is plotted in Fig. 3.2 with both the original and revised parameters. Because of the extraordinary computational cost associated with using the original parameters, Yim's choice of values is used in the present work.

Table 3.1: Pair-specific parameter values for the Albe-Möller potential.

	B–B	B–N	N–N
D_0, eV	3.08	6.36	9.91
r_0, Å	1.59	1.33	1.11
S	1.0769	1.0769	1.0769
β, Å^{-1}	1.5244506	2.043057	1.92787
γ	1.6×10^{-6}	1.1134×10^{-5}	1.9251×10^{-2}
n	3.9929061	0.364153367	0.6184432
λ, Å^{-1}	0	1.9925	0
c	3.316257	1092.9287	17.7959
d	0.01	12.38	5.9484
h	0.5	-0.5413	0
R, Å	2.0	2.0	2.0
D, Å	0.1	0.1	0.1

To compute the force on particle i, one must substitute the potential function into Eq. 3.2. However, the differentation is nontrivial due to the effects of the tertiary particles k. For a complete overview of the force derivation, see Appendix A.

3.1.2.2 Xenon Potential Function

The potential function used to model the interactions between the impacting xenon ion and the atoms in the BN lattice is the Ziegler-Biersack-Littmark (ZBL) "universal" potential[63,64]. It is a screened Coulomb potential of the form

$$\Phi_{ZBL}\left(\mathbf{r}_i, \mathbf{r}_j\right) = \Phi_{ZBL}\left(r_{ij}\right) = f_C\left(r_{ij}\right) \frac{Z_i Z_j e^2}{4\pi\varepsilon_0 r_{ij}} \sum_{n=1}^{4} A_n \exp\left(-B_n \frac{r_{ij}}{a_F}\right), \tag{3.14}$$

where a_F is the screening length, calculated as

$$a_F = \frac{0.8853 a_0}{Z_i^{0.23} + Z_j^{0.23}}. \tag{3.15}$$

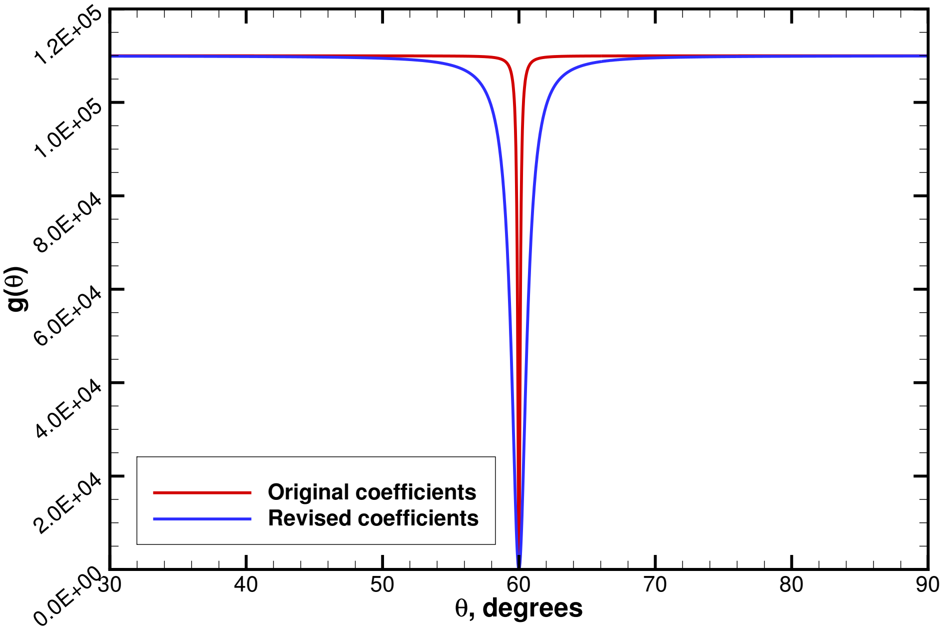

Figure 3.2: $g\left(\theta_{ijk}\right)$ for each set of coefficients c and d

The values for the parameters A_n and B_n are given in Table 3.2. Note that the ZBL potential is purely repulsive. The van der Waals attraction between the impacting xenon and the lattice atoms is very weak compared to the covalent attraction between the lattice atoms. Thus, a purely repulsive potential function is considered acceptable. Note also that this potential differs from the Molière potential used by Yim. Although both are screened Coulomb potentials, the ZBL potential better reproduces experimental measurements, particularly at long interaction ranges[64]. A comparison of the two potential functions is given in Fig. 3.3. The cutoff function used for the ZBL potential is given by

$$f_C\left(r\right) = \begin{cases} 1, & r \leq r_{cut} \\ 0, & r > r_{cut} \end{cases}, \tag{3.16}$$

with $r_{cut} = 4.6\,\text{Å}$. Although a smooth cutoff function is often preferred, this function is considered adequate for the present work because the value of the potential is very small at the selected cutoff radius.

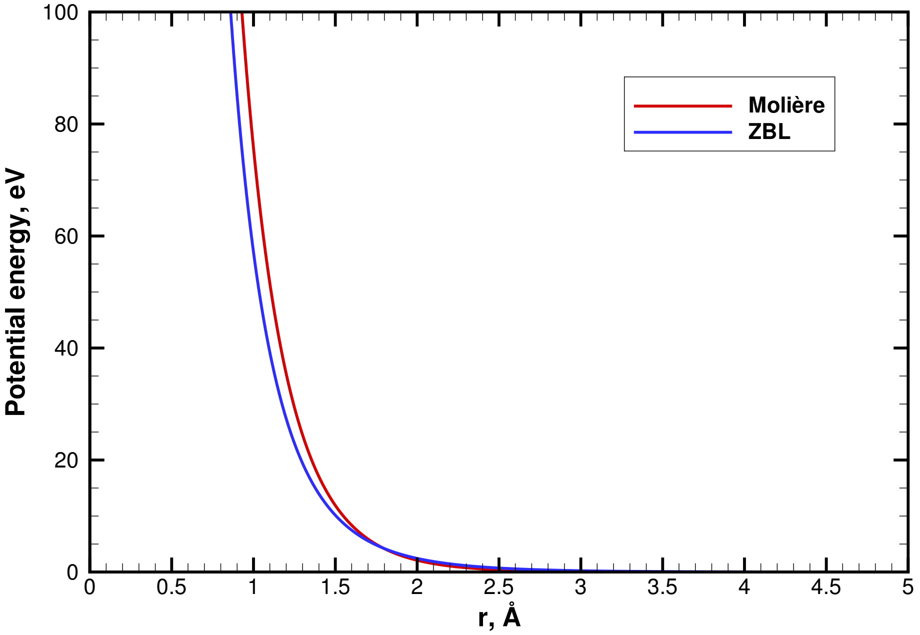

Figure 3.3: ZBL and Molière potential functions for $Z_i = 54$ and $Z_j = 5$.

Table 3.2: Parameter values for the Ziegler-Biersack-Littmark potential.

n	1	2	3	4
A_n	0.1818	0.5099	0.2802	0.02817
B_n	3.2	0.9423	0.4029	0.2016

By substituting the ZBL potential function into Eq. 3.2, one can calculate the force acting on particles i and j due to their interaction. Because the ZBL potential is a simple pair-wise function, the force is simply

$$\mathbf{F}_{ij} = \hat{\mathbf{r}}_{ij} \frac{d}{dr_{ij}} \left(\Phi_{ZBL} \left(r_{ij} \right) \right) = -\mathbf{F}_{ji}, \tag{3.17}$$

where $\hat{\mathbf{r}}_{ij}$ is the unit vector pointing from i to j. For the complete derivation of the force vector, see Appendix A.

As a final note: Although the impacting particle is referred to as an ion, it is likely that it absorbs an electron from the BN surface and reflects as a neutral atom.

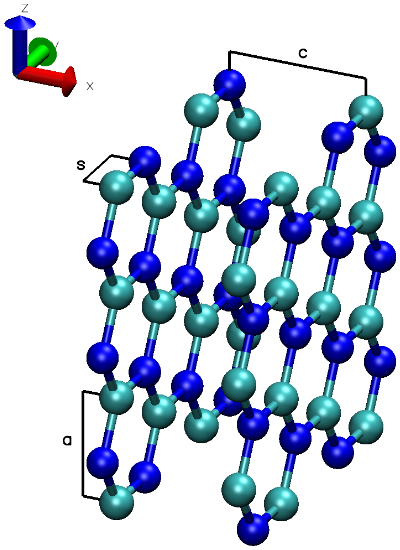

Figure 3.4: Definition of the lattice constants for *h*-BN.

Table 3.3: Lattice constants for *h*-BN.

Lattice constant	Value, Å
a	2.496
c	3.245
s	1.441

However, the basic MD method is not capable of accurately modeling shifts in the charge state of a particle. Instead, it is assumed that the xenon potential function is independent of charge state, so that the ZBL potential can be used to model all interactions with the impacting xenon. However, the term “ion” is still used to refer to the impacting particle for the sake of convenience.

3.2 Simulation Domain

Hexagonal boron nitride has a structure much like that of graphite, with many parallel sheets that consist of alternating boron and nitrogen atoms arranged in a repeating hexagonal pattern. A sample of the *h*-BN structure is shown in Fig. 3.4 along with the definitions of the lattice constants a, c, and s. The equilibrium value for each lattice constant is given in Table 3.3.

3.2.1 Boron Nitride Lattice

The *h*-BN lattice used in the sputtering simulations must be sized such that the energy deposited by the impacting ion is well distributed among the lattice atoms before the collision cascade reaches the domain boundaries. If the lattice is too small, then the calculated sputter yields will be artificially increased. However, larger lattices incur a greater computational cost, so it is advantageous to use a domain that is no larger than necessary. For these reasons, the size of the lattice used depends on the properties of the incident ion.

In his work,[11,12] Yim used three separate lattice sizes depending on the energy of the incident ions. These lattice sizes are defined by the number of parallel sheets (x direction), point-to-point hexagons (y direction), and side-to-side hexagons (z direction). For ion energies of 100 eV and below, the lattice consists of 24 sheets that are 18 point-to-point hexagons wide and 10 side-to-side hexagons tall, resulting in dimensions of $78 \times 78 \times 25\,\text{Å}^3$. For ion energies between 100 eV and 250 eV, the lattice consists of 32 sheets of 24 × 12 hexagons, or dimensions of $104 \times 104 \times 30\,\text{Å}^3$. Finally, for ion energies 250 eV or greater, the lattice consists of 40 sheets of 30 × 12 hexagons, or dimensions of $130 \times 130 \times 30\,\text{Å}^3$.

The rules established by Yim are used to guide the domain sizing in the present work, but with two key changes. First, there are additional domain sizes used for energies less than 250 eV. Second, the depth of the simulated lattice, determined by the number of side-to-side hexagons, is not fixed in the present work. Instead, additional atoms are added at the lower z boundary as the surface recesses under repeated ion bombardment. This prevents the boundary conditions from affecting the collisional processes near the exposed surface even after pronounced surface erosion. The criteria used to determine when additional atoms are added to the domain are discussed in Chapter IV. The lattice size used for each simulation case is presented along with the tabulated sputter yields in Appendix B.

As a final note regarding the lattice sizing: Due to the immense cost of the MD sputter simulations (several minutes *per ion impact*), a detailed sensitivity study with respect to the lattice dimensions has not yet been performed. This is particularly important for the cases of high ion energy ($\mathcal{E}_i \gtrsim 100\,\mathrm{eV}$), as the computational cost of the MD simulations increases with the lattice size, as mentioned above. Hence, it is possible that the simulations at these high ion energies are not domain independent. For some of the lower-energy cases, abbreviated sputtering simulations ($\lesssim 10,000$ impacts) were performed using larger domains, and no statistically significant differences were observed in the calculated sputter yields. Thus, the low-energy simulations are considered to be domain independent.

3.2.2 Boundary Conditions

The simulation domain has periodic boundary conditions in x and y, with all potential calculations wrapping across the periodic boundaries. Any atoms that pass a boundary in x or y also wrap across the boundary. In this sense, the simulation domain behaves as a single unit in an infinitely repeating array of h-BN lattices. The boundary in $+z$ is open and is placed $24\,\text{Å}$ above the exposed h-BN surface, allowing particles to exit the system during sputtering events. Each time a particle passes the $+z$ boundary, the current time step is recorded to a text file. If the exiting particle is a xenon ion, its kinetic energy, angle of ejection relative to the surface normal, and azimuthal angle relative to the x axis are recorded to the same text file. If the exiting particle is a boron or nitrogen atom, then any additional boron and nitrogen atoms within the interaction range of the Albe-Möller potential are also flagged, and the group of particles is treated as an exiting molecule. The center-of-mass velocity of the molecule is then calculated, and the species, translational kinetic energy, ejection angle, and azimuthal angle are then recorded to the text file.

The boundary conditions in $-z$ are less trivial to define. The simulated lattice is meant to represent several angstroms of depth near the exposed surface of a much larger mass of solid BN. The virtual solid below the $-z$ boundary has the effect of fixing the simulated lattice in place and serves as a heat sink through which the energy deposited by impacting ions can be dissipated. Since the bulk material is not simulated, this mechanical and thermal stabilization must be achieved by altering the behavior of the simulated particles.

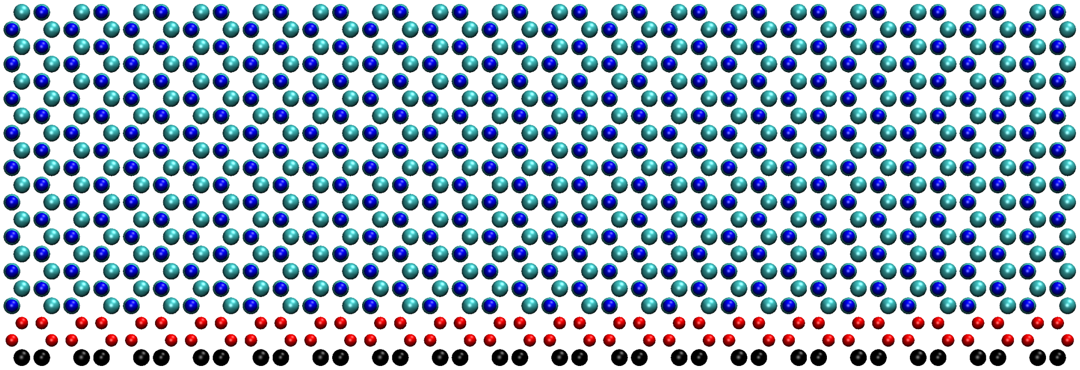

Figure 3.5: Example of initial h-BN lattice used in sputtering simulations.

Figure 3.5 shows a side-on view of an h-BN lattice for use in the sputtering simulations. To model the mechanically stabilizing effect of the bulk material, the atoms in the bottommost layer, shown in black, are fixed in space and are referred to as the "immobile atoms." The interatomic forces anchor the rest of the lattice to these atoms, preventing any bulk rotation or drift. The two layers of atoms immediately above the immobile layer are called the "thermostat layers" (shown in red), and serve to regulate the system temperature. Note that both the immobile atoms and the thermostat atoms are placed far away from the exposed surface of the h-BN lattice. This is done to minimize the influence of the modified particle dynamics in these layers on the dynamics near the surface.

3.2.2.1 Temperature Regulation

The technique used to regulate the system temperature is called the Berendsen thermostat,[65] a method of scaling the post-integration velocity of the thermostat particles according to the instantaneous system temperature T. When applied to the Velocity Verlet scheme, it is written as

$$\begin{aligned}\mathbf{v}\left(t+\Delta t\right) &= \lambda_B\left(T\right)\left(\mathbf{v}\left(t\right)+\frac{\mathbf{a}\left(t+\Delta t\right)+\mathbf{a}\left(t\right)}{2}\Delta t\right)\\ &= \lambda_B\left(T\right)\left(\mathbf{v}\left(t+\frac{\Delta t}{2}\right)+\frac{\mathbf{a}\left(t+\Delta t\right)}{2}\Delta t\right),\end{aligned} \tag{3.18}$$

$$\lambda_B\left(T\right) = \sqrt{1+\frac{\Delta t}{\tau}\left(\frac{T_0}{T}-1\right)}, \tag{3.19}$$

where T_0 is a prescribed equilibrium temperature. The time constant τ determines the strength of the thermal coupling, with smaller values of τ resulting in a faster approach to equilibrium. The ratio ${}^{\Delta t}/_{\tau}$ is kept at 0.0025 for this work. The temperature T used to calculate λ_B is computed from a statistical average of the kinetic energy of all N lattice atoms:

$$T = \frac{2}{3\left(N-1\right)}\sum_{i=1}^{N}\frac{1}{2}m_i\left|\mathbf{v}_i\right|^2. \tag{3.20}$$

Note that this temperature is instantaneous, and thus varies from one time step to the next. Berendsen *et al.* noted,[65] however, that λ_B is a relatively weak function of T, so the precise time at which T and λ_B are calculated does not significantly affect the overall dynamics. For the purposes of this work, λ_B is calculated from the temperature at time $t+\left({}^{\Delta t}/_{2}\right)$, just after the force calculation and just before the second step of the Velocity Verlet integration.

As stated above, the Berendsen thermostat is applied only to the atoms in the thermostat layers. With the exception of the immobile atoms, all other particles in the system follow the standard two-step Velocity Verlet integration scheme. This is done to prevent the thermostat from dissipating the energy in the collision cascades that develop near the surface during ion bombardment.

For the purposes of this work, the equilibrium temperature set by the Berendsen thermostat is fixed at 150°C. This temperature is reported in several studies of *h*-BN sputtering under xenon ion bombardment.[16,66,67] However, it should be noted that the temperature of the ceramic walls in a Hall thruster is expected to be several hundred °C. Although the temperature discrepancy does not directly affect the validity of the calculated sputter yields, it should be considered a potential source of error in the Hall thruster simulations described in Chapter VI, as the sputter yield of a material tends to increase with temperature.

3.3 Simulation Methodology

Each MD simulation case is defined by the kinetic energy and incidence angle of the impacting ions. The range of ion energies investigated is meant to cover the range of ion energies that typically appear in Hall thrusters, from tens to hundreds of electron volts. The incidence angles investigated range from 0° (normal incidence) up to 75°.

Each ion impact is simulated by placing the ion at the upper z boundary with the prescribed energy and angle of incidence. The ion's initial position in x and y and the azimuthal angle of the ion's trajectory are randomized in order to minimize the influence of the lattice orientation on the calculated sputter yields. The lattice atoms are initialized according to a 3D Maxwell-Boltzmann distribution with the equilibrium temperature T_0 using the acceptance-rejection method.

After initialization, each ion impact is simulated for a minimum of 20,000 time steps with $\Delta t = 0.1\,\mathrm{fs}$. The simulation continues to run until the system temperature re-equilibrates to within 10% of the prescribed equilibrium temperature and no particles have exited the domain within the last 10,000 time steps. The system is then reinitialized to simulate an additional ion impact. This process is repeated until a steady state is reached. Here, the steady state is defined by two criteria:

1. The sputter yields do not change with additional ion impacts.
2. Boron and nitrogen are sputtered at the stoichiometric ratio of bulk BN.

These criteria are discussed further in Chapter VI.

3.3.1 Temperature Monitoring

As noted above, there can be large statistical fluctuations in the calculated system temperature in the MD simulations. When monitoring the system temperature during re-equilibration, it is desirable to smooth these fluctuations through some averaging process. In this work, the sub-relaxation technique proposed by Sun and Boyd[68] is used to calculate a time-averaged temperature $\bar{T}$ from the previous time-averaged temperature and the present instantaneous temperature T:

$$\bar{T} = \left(1 - \frac{1}{\sigma}\right)\bar{T} + \frac{1}{\sigma}T, \tag{3.21}$$

where σ sets the strength of the weighting. Because HOOMD-blue uses a high-level scripting language to control the flow of simulations, this temperature calculation is only performed at a set interval of 2500 time steps, and a relatively large value of $\sigma = 5$ is used. Each time the average is updated, it is compared to the desired equilibrium temperature T_0 set by the Berendsen thermostat. If the average temperature does not fall within 10% of the equilibrium temperature, the current ion impact simulation continues to run. Once the minimum 20,000 time steps are simulated and the average temperature falls within 10% of equilibrium for four consecutive checks, the system is reinitialized and a new ion is injected.

3.3.2 Lattice Pre-Conditioning

With repeated ion bombardment, the topology and chemical composition of the *h*-BN surface are expected to change. Namely, the crystal structure near the surface degrades and becomes enriched in boron, with nitrogen being preferentially sputtered during the early stages of bombardment. An example of a lattice after repeated bombardment is shown in Fig. 3.6. Under the conditions typical of Hall thrusters, however, the process of amorphization and boron enrichment is completed in seconds to minutes. Thus, these transient sputtering conditions are considered irrelevant to the problem of Hall thruster wall erosion.

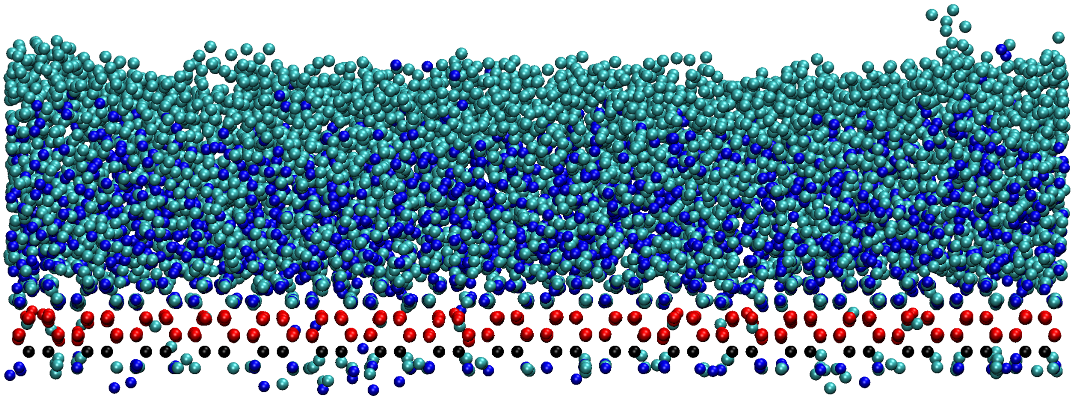

Figure 3.6: Boron nitride lattice after continuous ion bombardment. Note the amorphous, boron-enriched structure near the surface.

In order to accelerate the approach to steady-state sputtering conditions, a lattice pre-conditioning algorithm has been developed. This algorithm uses a Monte Carlo technique to randomly remove nitrogen atoms from the near-surface layers of the lattice and then perturb the remaining atoms, generating an amorphous, boron-enriched structure. The algorithm proceeds as follows.

1. The user sets an initial depth from the BN surface over which the algorithm operates, measured in side-to-side hexagons.

2. The nitrogen atoms in the assigned layers are removed at random. The proba-

bility that a given atom is removed is a function of its distance from the exposed BN surface, with atoms closer to the surface more likely to be removed.

3. Remaining atoms are randomly perturbed. If the perturbation causes the total potential energy of the system to decrease, then it is accepted. Otherwise it is rejected and the perturbed atom is restored to its previous position. This process is repeated until the change in total potential energy with each perturbation becomes small or until 1000 consecutive perturbations are rejected.
4. The interatomic forces and time integration are activated, and the lattice is allowed to reach thermal equilibrium before injecting any ions.

After this process is completed, the first ion is injected and the simulation is allowed to proceed as normal.

3.3.3 Data Reduction

The raw outputs of the sputtering model are the time of ejection, species, kinetic energy, polar ejection angle, and azimuthal angle of each particle that passes the upper z boundary. These data must be reduced in order to determine the integrated and differential sputter yields for comparison to experimental measurements. These data can also be used to analyze the behavior of the sputtered particles, which is a critical factor in predicting the transport of the erosion products in a Hall thruster.

3.3.3.1 Integrated Sputter Yields

The integrated sputter yield is computed as the average number of boron and nitrogen atoms lost from the surface over some number of ion impacts N_{ions}:

$$Y_{total} = \frac{N_B + N_N}{N_{ions}}, \tag{3.22}$$

where Y is measured in units of atoms/ion. To convert this to units of mm^3/C:

$$Y\left[\mathrm{mm}^3/\mathrm{C}\right] = Y\left[\mathrm{atoms/ion}\right] \times \frac{0.5\left(m_B + m_N\right)}{e\rho_{BN}}, \tag{3.23}$$

where m_B and m_N are the molecular mass of boron and nitrogen, respectively, e is the elementary charge, and ρ_{BN} is the mass density of *h*-BN.

3.3.3.2 Differential Sputter Yields

Differential sputter yields are computed by generating a virtual hemisphere centered at the origin of the ejected particles, separating the hemisphere into slices of equal solid angle Ω_0, and recording each particle that passes through each section. The differential yield is then evaluated as

$$y\left(\theta, \phi\right) = \frac{N_B\left(\theta, \phi\right) + N_N\left(\theta, \phi\right)}{\Omega_0 N_{ions}}, \tag{3.24}$$

where θ and ϕ define the centroid of each section of the hemisphere. To determine $y\left(\theta, \phi\right)$ in units of $\mathrm{mm}^3/\mathrm{C/sr}$, a transformation similar to Eq. 3.23 is used.

3.3.3.3 Velocity Distribution Functions

The 3-dimensional velocity distribution function (VDF) of the sputtered particles is determined by first calculating the velocity vector of each particle from its kinetic energy, ejection angle, and azimuthal angle. Then, velocity space is discretized into bins, and each particle is assigned into the corresponding bin for each dimension in space in order to generate a histogram. Finally, the histogram is normalized so that it integrates to 1, giving a properly normalized VDF for each dimension. Analytical functions such as the Sigmund-Thompson distribution (Eq. 2.13) can then be fit to these histograms for implementation into a Hall thruster plasma model.

CHAPTER IV

MD Simulation Results and Validation

What follows below is a detailed discussion of the MD simulation results, including the total sputter yields, differential sputter yields, and sputtered particle properties. The dependence of these results on ion energy and incidence angle is also discussed, although only for a subset of simulation cases. A complete set of total sputter yields and the various fit parameters discussed below is given in Appendix B.

4.1 Chemical Composition

For the purposes of material transport modeling, it is valuable to know the species composition of the products of *h*-BN sputtering. The condensible erosion products are of particular interest, as these particles can redeposit on the thruster walls, reducing the effective erosion rate, or on spacecraft surfaces, possibly affecting mission-critical systems. In the case of *h*-BN, the condensible products of erosion include any compound containing boron, as boron compounds tend to exist in the solid state, and possibly monatomic nitrogen because it is highly reactive. Diatomic nitrogen is not considered condensible, as it is highly nonreactive and exists naturally in the gaseous state except under extreme conditions.

Table 4.1 shows the mole fractions of some boron-containing species within the population of sputtered particles. Only a subset of the MD simulation cases are repre-

Table 4.1: Mole fractions of boron-containing species in the sputtered particle population for a subset of MD simulation cases.

Ion energy, eV	Incidence angle	Monatomic	Diatomic	B_xN_y
60	0°	0.96	0.00	0.04
	60°	0.96	0.01	0.02
100	0°	0.95	0.01	0.02
	60°	0.86	0.03	0.02
250	0°	0.88	0.03	0.06
	60°	0.74	0.05	0.11

sented, but the results for all other cases show similar trends. These data indicate that between 70% and 100% of sputtered particles that contain boron are simply boron atoms. Thus, it is reasonable to say that for *h*-BN under xenon ion bombardment, boron tends to sputter in its monatomic form.

It is worth noting that, over the range of ion energies investigated, the fraction of molecular boron and B_xN_y compounds appears to increase with ion energy. This is likely an indication that the ions transfer more energy into the *h*-BN lattice at higher impact energies, and that some of this additional energy is dissipated through the ejection of heavier particles. Table 4.1 also suggests that the fraction of heavy particles is greater at 60° incidence compared to 0° incidence, at least for 250 eV ion energy. As will be demonstrated below, the peak in the total sputter yield tends to occur around 50°–70° incidence for a given ion energy, suggesting that more energy is deposited in the lattice atoms at these oblique angles of incidence than at near-normal incidence. Thus, it is again likely that the additional deposited energy is dissipated via the ejection of heavier particles.

Table 4.2 shows the mole fractions of nitrogen containing species for the same subset of simulation cases. The data for nitrogen show greater variability than those for boron, but seem to indicate that nitrogen is sputtered largely in the form of N_2. The mole fraction of atomic nitrogen increases somewhat from 60 eV to 100 eV, but stays approximately the same between 100 eV and 250 eV. Conversely, the fraction

Table 4.2: Mole fractions of nitrogen-containing species in the sputtered particle population for a subset of MD simulation cases.

Ion energy, eV	Incidence angle	Monatomic	Diatomic	B_xN_y
60	0°	0.10	0.86	0.02
	60°	0.23	0.74	0.03
100	0°	0.16	0.80	0.03
	60°	0.31	0.62	0.06
250	0°	0.19	0.69	0.10
	60°	0.31	0.48	0.20

of diatomic nitrogen appears to decrease with increasing ion energy, and the fraction of B_xN_y compounds increases. Thus, it appears that the form of sputtered nitrogen shifts from N_2 to B_xN_y with increasing ion energy, but N_2 still makes up the relative majority of nitrogen-containing species even at 250 eV and 60° incidence.

The above data provide valuable insight regarding the chemical composition of the erosion products that may appear in a Hall thruster, but at present, it is infeasible to perform a detailed analysis of the post-sputtering behavior of every single species. For example, over the course of 43,000 ion impact events at 250 eV and 60° incidence, only 44 molecules of BN_2 were ejected from the lattice. This small sample size is inadequate for calculating a fitted VDF within reasonable statistical uncertainty. It is also unclear whether such compounds are physically realistic or are simply an unexpected consequence of the Albe-Möller potential function used for the boron and nitrogen interactions. Hence, for the remainder of this work, two assumptions are made regarding the sputtered particles:

1. Boron sputters in the form of B only.
2. Nitrogen sputters in the form of N_2 only.

The first assumption is well supported by the MD results over the range of ion energies investigated, but may break down at even higher ion energies. The second assumption is not so well supported. In particular, there seems to be a significant fraction of atomic nitrogen sputtered from the *h*-BN lattice. Atomic nitrogen readily forms compounds with many other elements, and can thus be considered condensible. However, N_2 is still more prevalent than N among the sputtered particles, and under steady-state sputtering conditions, atomic boron is still the most abundant condensible species. Thus, B is considered the only condensible product of erosion for the purposes of this work, and the influence of N is saved for future studies.

4.2 Total Sputter Yields

4.2.1 Dependence on Ion Fluence

In Sect. 3.3.2, it was asserted that during the early stages of ion bombardment, nitrogen is sputtered preferentially over boron from an *h*-BN lattice, resulting in boron enrichment in the near-surface layers. To demonstrate this, Fig. 4.1 shows the average total sputter yield, average boron yield, and average nitrogen yield for the case of 100 eV ions at 45° incidence where the initial lattice is a perfect crystal of *h*-BN. The values shown are moving averages with a period of 5000 ion impacts. The wall time for this simulation was approximately four months running on an Nvidia Tesla C2075 GPU.

As Fig. 4.1 shows, there is a rapid increase in the sputter yield over the first 5000 or so ion impacts. This is driven entirely by the sputtering of nitrogen, which rises from a yield of 0.15 atoms per ion after 500 impacts to about 0.64 atoms per ion after 6000 impacts. After about 10,000 ion impacts, the nitrogen yield begins to decrease with increasing ion fluence, indicating that the near-surface layers are being depleted of nitrogen, and thus enriched in boron. In contrast, the boron yield changes much less rapidly and seems to increase in a nearly monotonic fashion, doubling from about 0.03 atoms per ion after 500 impacts to about 0.06 atoms per ion after 48,000 impacts. For reference, the longest sputtering simulation performed by Yim

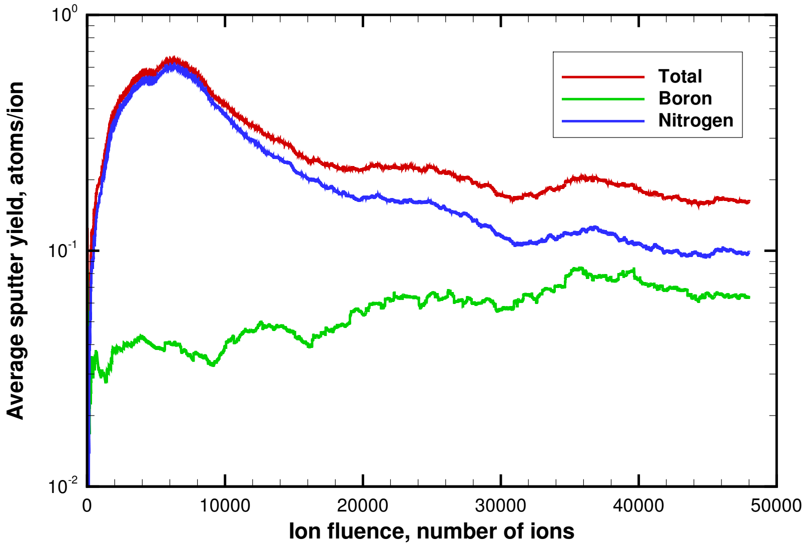

Figure 4.1: Average total sputter yield, average boron yield, and average nitrogen yield for 100 eV ions at 45° incidence, where the initial lattice is a perfect crystal of h-BN.

covered only 1500 consecutive ion impacts,[11,12] so Yim was unable to capture the non-monotonic behavior in the integrated sputter yield. Discovering this behavior was only made possible through the use of the massively parallel, GPU-based computing provided by CUDA and HOOMD-blue.

Figure 4.1 shows that the sputter yields of nitrogen and boron are converging towards one another, as would be expected in the steady state. However, as of 48,000 ion impacts, the nitrogen yield is still more than 50% greater than the boron yield, and it is not clear how many more ion impacts are required for complete convergence. Because the boron yield changes much less rapidly than the nitrogen yield, the sputter yield under steady-state conditions can be estimated from the yield of boron alone:

$$Y \approx \frac{2N_B}{N_{ions}}. \tag{4.1}$$

In this sense, the two criteria described in Sect. 3.3 for steady-state sputtering are reduced to the single criterion that the boron yield is constant with increasing ion fluence. For simulations starting from a pre-conditioned h-BN lattice, this is generally the case, as is demonstrated in Fig. 4.2. For each simulation case shown, the fluctuations in the boron yield stabilize after about 10,000 ion impacts, after which the only variations are due to statistical noise. Because of this, the sputter yield estimated by Eq. 4.1 is considered an accurate estimate of the steady-state sputter yield.

Since it has been established that the h-BN lattice becomes enriched in boron over the course of ion bombardment, we can now revisit the problem of the lattice depth. In Sect. 3.2.1, it was noted that under continuous ion bombardment, the surface of the lattice recesses due to the loss of surface atoms. To prevent the boundary conditions from modifying the surface dynamics, additional atoms are added at the lower z boundary as needed. The criterion used to determine when additional atoms are added is based on the ratio of boron to nitrogen atoms in the lattice, ${}^{N_N}/_{N_B}$. When this ratio is less than 0.3, the atoms remaining in the lattice are shifted upwards in z and two additional layers of atoms are added at the bottom. Then, the immobile and lattice atoms are reassigned to remain consistent with the boundary conditions defined in Sect. 3.2.2.

4.2.2 Dependence on Ion Energy

Figure 4.3 shows the integrated sputter yield of h-BN at normal ion incidence as a function of ion energy. The sputter yields labeled as “total” are calculated according to Eq. 3.22, whereas the estimated yields are computed according to Eq. 4.1. Also shown in Fig. 4.3 are the quartz crystal microbalance (QCM) measurements of Rubin *et al.* for HBC grade boron nitride.[66] This data set is chosen for comparison because it is very comprehensive, extending down to 60 eV incident ion energy and covering incidence angles from 0° to 45°. The data labeled QCM low correspond to the uncorrected QCM measurements and capture only condensible species. The data

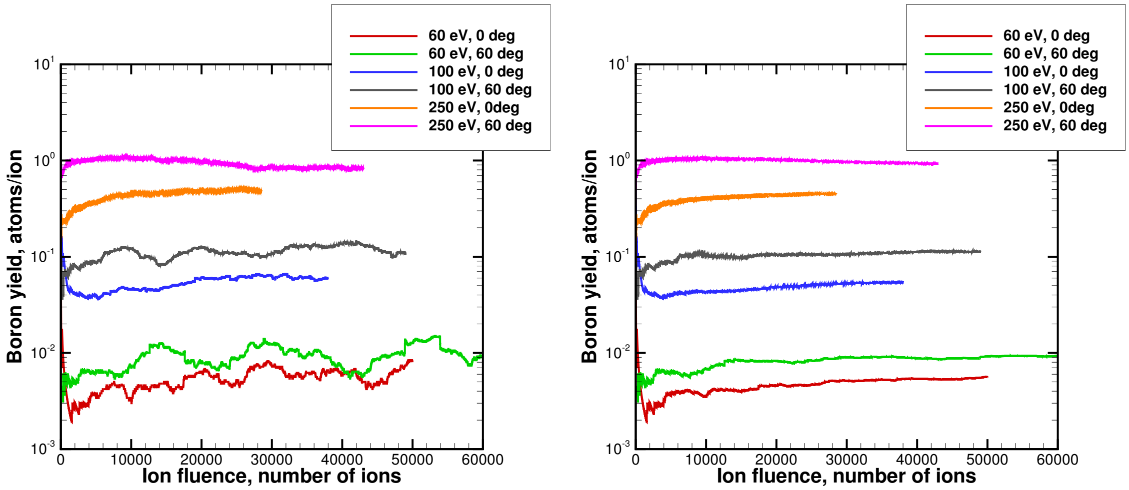

(a) Moving average, period of 5000

(b) Cumulative average

Figure 4.2: Average boron yield as a function of ion fluence for a subset of MD simulation cases.

labeled QCM high are the QCM measurements corrected to include non-condensible species. The error bars on the QCM measurements correspond to the estimated uncertainty of 30%. The uncertainty of the calculated sputter yields is estimated as $^{Y}/_{\sqrt{N_{ions}}}$, which is very small for most simulation cases.

Figure 4.3 indicates that the total and estimated sputter yields computed from the MD data agree very well, as would be expected under steady-state conditions. At ion energies of 100 eV and below, the calculated yields fall below the lower bound of the QCM measurements. For ion energies between 150 eV and 300 eV, the calculated yields fall within the bounds of the QCM measurements. However, extrapolating the yields past 300 eV suggests that the calculated yields will become greater than the QCM measurements. Overall, the calculated yields agree reasonably well with the measured values within the range of ion energies investigated here, suggesting that the MD model is largely capturing the appropriate physics.

The black curves in Fig. 4.3 are Bohdansky fits[22,69] to the estimated sputter yields.

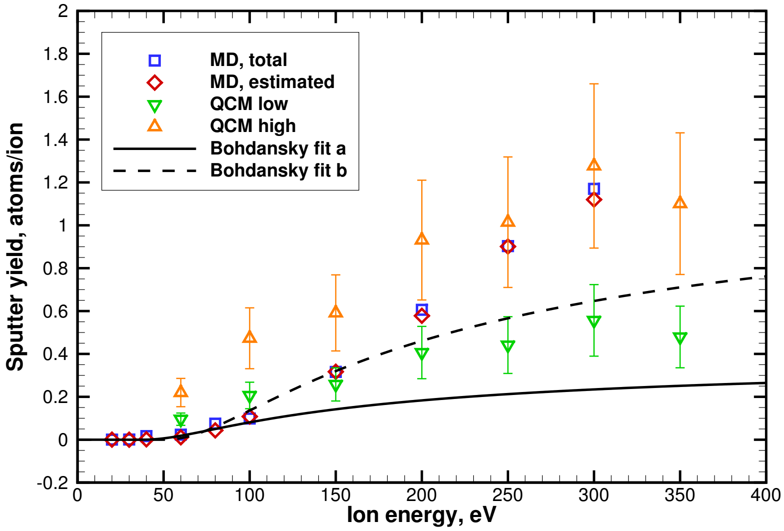

Figure 4.3: Sputter yield of h-BN at normal incidence as a function of incident ion energy. Error bars on the QCM data correspond to an estimated uncertainty of 30%.

Table 4.3: Bohdansky parameter values for normal ion incidence. Reported uncertainties are 95% confidence intervals determined from the fitting process.

	Y_∞, atoms/ion	E_{th}, eV
Fit A	0.4 ± 0.3	36 ± 3
Fit B	1.3 ± 1.1	48 ± 9

These fits are based on Eq. 2.15 and take the form

$$Y_B\left(\mathcal{E}_i\right) = Y_\infty \left[1 - \left(\frac{E_{th}}{\mathcal{E}_i}\right)^{2/3}\right] \left(1 - \frac{E_{th}}{\mathcal{E}_i}\right)^2, \tag{4.2}$$

with Y_∞ and E_{th} behaving as free fit parameters. Rather than minimizing $\sum\left(Y_B - Y\right)^2$, this equation is fit by minimizing

$$\sum\left(\frac{\left(Y_B - Y\right)}{Y}\right)^2. \tag{4.3}$$

This fitting process limits the bias towards larger values, making it more appropriate for cases such as this in which data points can vary widely in magnitude.

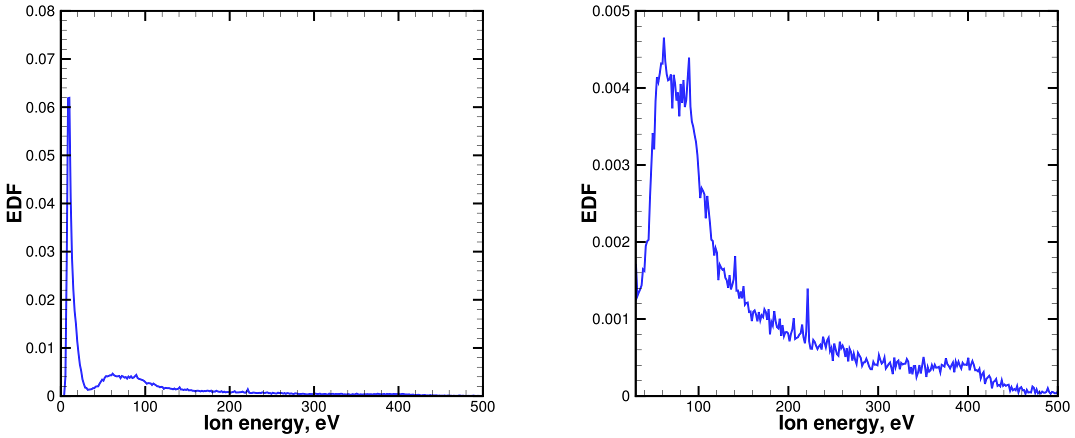

(a) (b)

Figure 4.4: Energy distribution function of ions striking the discharge channel walls in a Hall thruster operating at a discharge voltage of 400 V: (a) all ion energies, (b) energies 30 eV and greater.

The fit parameters Y_∞ and E_{th} are given random initial values during the least-squares fitting process, resulting in one of the two converged sets of parameters given in Table 4.3. The parameter Y_∞ is the sputter yield in the limit of $\mathcal{E}_i \to \infty$, whereas E_{th} is the threshold energy for sputtering. The threshold energy is of particular interest in Hall thrusters because most of the ions that strike the walls in a Hall thruster have kinetic energies near the threshold, i.e. less than about 100 eV. Consider Fig. 4.4, which shows the energy distribution function of ions striking the thruster walls in a Hall thruster operating at 400 V discharge voltage.* Approximately 50% of all ions striking the walls have a kinetic energy less than 30 eV, and about 75% have a kinetic energy less than 105 eV. Hence, accurately determining the threshold energy and the sputter yields in the near-threshold regime is of critical importance.

The two Bohdansky curve fits to the MD data give values of 36±3 eV and 48±9 eV for the threshold energy. The lowest ion energy for which the MD model gives a

---

*Calculated from a hybrid-PIC simulation of NASA's HiVHAc Hall thruster. Model and simulation details are described in Chapters V and VI finite sputter yield is 40 eV, suggesting a threshold energy between 30 and 40 eV. Similarly, a Bohdansky fit to the QCM data gives a threshold energy of 32 ± 6 eV, and Rubin claims that the QCM also detected BN sputtering at energies as low as 40 eV, although the data were not reported due to high uncertainty.[66] Thus, the MD model and Rubin's QCM measurements agree that the threshold energy for sputtering of *h*-BN sputtering most likely falls between 30 eV and 40 eV.

It is worth noting that the Bohdansky fits do not match the calculated sputter yields very well at energies above 100–150 eV. While this may be a result of the fitting process used, it may also be an indication that there is some bias in the simulation results at those energies. One possibility is that these cases are not domain independent, causing the calculated sputter yields to be artificially inflated. Establishing domain independence for cases of high ion energy is especially difficult because increasing the domain size also increases the computational cost of the simulation. Hence, the task of establishing domain independence at high ion energies is left for future studies. However, because a significant fraction of ions striking the walls may have an energy greater than 100 eV, this should be kept in mind as a significant source of uncertainty in the upcoming chapters.

4.2.3 Dependence on Incidence Angle

Figure 4.5 shows the calculated *h*-BN sputter yields as a function of ion incidence angle for 100 eV and 250 eV incident ion energy. The estimated sputter yields are defined as in Eq. 4.1 above. Also plotted are Rubin's QCM measurements and a Yamamura fit to the estimated yields:[27]

$$Y_Y\left(\theta_i\right) = Y\left(0^\circ\right)\cos^A\left(\theta_i\right)\exp\left[-B\left(\frac{1}{\cos\left(\theta_i\right)}-1\right)\right]\left[\frac{1-\sqrt{\frac{E_{th,Y}}{\mathcal{E}_i}}\cos\left(\theta_i\right)}{1-\sqrt{\frac{E_{th,Y}}{\mathcal{E}_i}}}\right], \quad (4.4)$$

where A, B, and E_Y are free fit parameters. The values for these parameters are

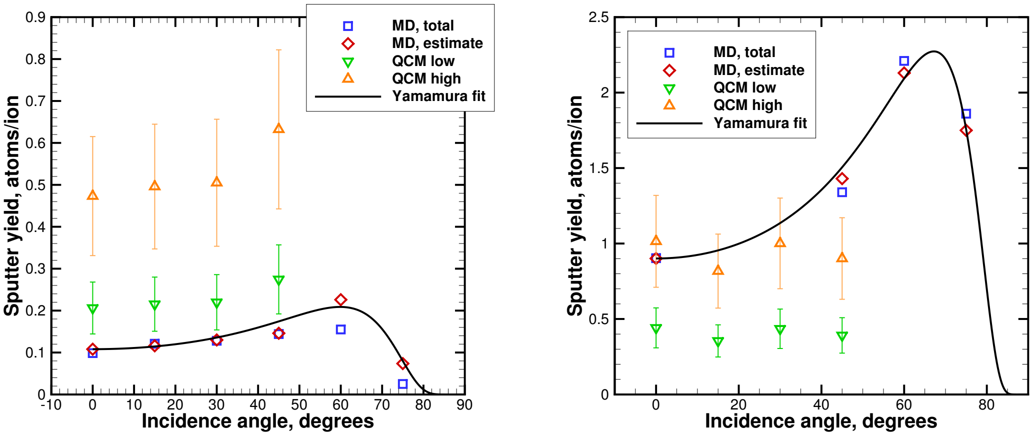

(a) 100 eV

(b) 250 eV

Figure 4.5: Sputter yield of *h*-BN as a function of ion incidence angle. Error bars on the QCM data correspond to an estimated uncertainty of 30%.

given in Table 4.4.

Table 4.4: Yamamura fit parameters for several ion energies.

Ion energy	A	B	E_Y, eV
60 eV	-3.7	2.2	0.0
80 eV	-2.8	1.6	0.0
100 eV	-3.5	1.7	0.0
200 eV	-2.9	1.2	0.0
250 eV	-2.8	1.1	0.0

Figure 4.5 indicates that for both 100 eV and 250 eV ion energy, the behavior of the calculated sputter yields is very well described by the Yamamura curve fit. The Yamamura curve reaches a peak between 60° and 70° incidence and then rapidly decreases towards zero for more oblique angles of incidence. Compared to the QCM measurements, the calculated sputter yields at 100 eV energy fall just below the experimental bounds. At 250 eV, the calculated yields fall within the experimental uncertainty for 0°–30° incidence, but the sputter yield at 45° incidence is somewhat larger than is measured. These observations are consistent with the trends seen in Fig. 4.3, so it still seems as through the sputtering model is capturing the appropriate

physics.

Note from Table 4.4 that the value of the fit parameter E_Y is zero for all ion energies shown. In the Yamamura function given by Eq. 2.22, E_Y is typically interpreted as the threshold energy for sputtering.[27] A threshold energy of zero is nonphysical, as it implies there are no forces binding the lattice atoms together. However, the physical significance of the threshold energy is not immediately apparent in the shape of the Yamamura function, as it is meant to capture the angular dependence of the sputter yields. So, for the purposes of this work, E_Y is interpreted as a simple fit parameter without any physical significance.

4.3 Differential Sputter Yields

To compare the differential sputter yields calculated from the MD model to Rubin's QCM measurements, a modified Zhang function is fit to the calculated values.[70] This function is based on Eq. 2.24 and takes the form

$$\begin{aligned} y_{MZ}\left(\theta,\phi\right) &= \frac{Y}{1-\sqrt{\frac{E^*}{\mathcal{E}_i}}\cos\left(\theta_i\right)} \times \frac{\cos\left(\theta\right)}{\pi} \\ &\quad \times \left[1-\frac{1}{4}\sqrt{\frac{E^*}{\mathcal{E}_i}}\left(\cos\left(\theta_i\right)\psi\left(\theta\right)+\frac{3\pi}{2}\sin\left(\theta_i\right)\sin\left(\theta\right)\cos\left(\phi\right)\right)\right], \quad (4.5) \\ \psi\left(\theta\right) &= \frac{3\sin^2\left(\theta\right)-1}{\sin^2\left(\theta\right)}+\frac{\cos^2\left(\theta\right)\left(3\sin^2\left(\theta\right)+1\right)}{2\sin^3\left(\theta\right)}\times\ln\left(\frac{1+\sin\left(\theta\right)}{1-\sin\left(\theta\right)}\right). \quad (4.6) \end{aligned}$$

In Ref. 66, the total yield Y was not known, and was thus treated as a free fit parameter alongside E^*. In the present work, Y is known and E^* acts as the sole fit parameter.

Figures 4.6 through 4.8 show the calculated differential sputter yields at 100 eV incident ion energy and the modified Zhang fits to those yields. Figures 4.9 and 4.10 show similar results for 250 eV ion energy. Note that these contours are for sputter yields of condensible (i.e., boron-containing) species only. Non-condensible species

Table 4.5: ${}^{E^*}/_{\mathcal{E}_i}$ from the modified Zhang fits to the calculated differential sputter yields and to the QCM measurements of HBC-grade BN from Ref. 66.

Ion energy, eV	Incidence angle	${}^{E^*}/_{\mathcal{E}_i}$ MD	${}^{E^*}/_{\mathcal{E}_i}$ QCM
100	0°	0.0	0.18
	15°	0.0	0.13
	30°	0.01	0.18
	45°	0.13	0.21
	60°	0.27	—
	75°	0.74	—
250	0°	0.0	0.25
	45°	0.15	0.34
	60°	0.37	—
	75°	1.0	—

are ignored to maintain consistency with Rubin's QCM measurements, which only detected condensible erosion products.[66] The values of ${}^{E^*}/_{\mathcal{E}_i}$ for the shown modified Zhang fits are given in Table 4.5 along with the values determined by Rubin *et al.* The values of ${}^{E^*}/_{\mathcal{E}_i}$ for other simulation cases are given in Appendix B.

The contours in Figs. 4.6–4.10 indicate that as the ion incidence angle becomes more oblique, the stronger the preference towards forward sputtering becomes, as one would expect. However, Table 4.5 shows that the changes in ${}^{E^*}/_{\mathcal{E}_i}$ differ greatly between the MD results and the QCM measurements. First, the MD results suggest that the sputtering at normal and near-normal incidence is purely diffuse, or cosine-like, whereas the QCM measurements show some non-diffuse behavior. Second, the MD results show a much stronger dependence of ${}^{E^*}/_{\mathcal{E}_i}$ on the ion incidence angle than the QCM measurements over the range of 0°–45° incidence. This may mean that there is some deficiency in the sputtering model, but it is also possible that this is related to the temperature of the QCM device, as the authors of Ref. 66 noted that the QCM temperature was highly sensitive to the measurement location. Further investigation is required to determine the exact reason for the disparity between the simulations and the experiments.

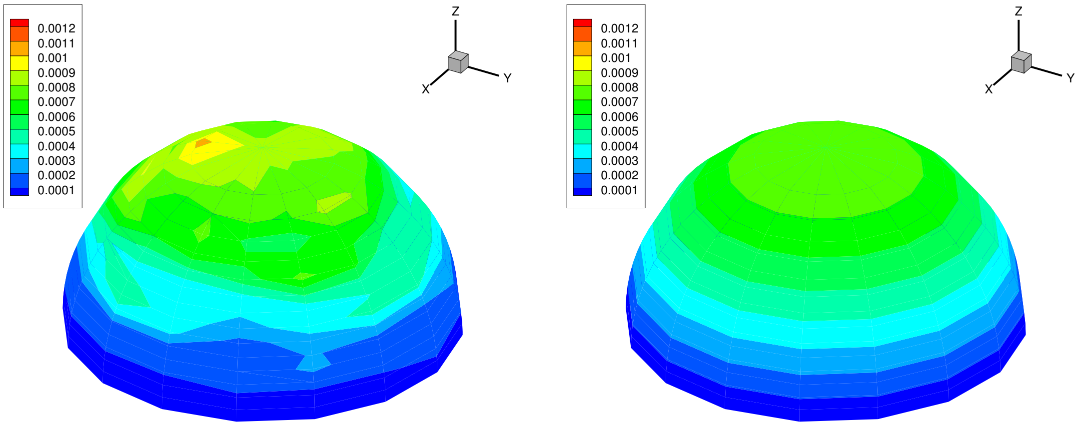

(a) 0° incidence

(b) 0° incidence

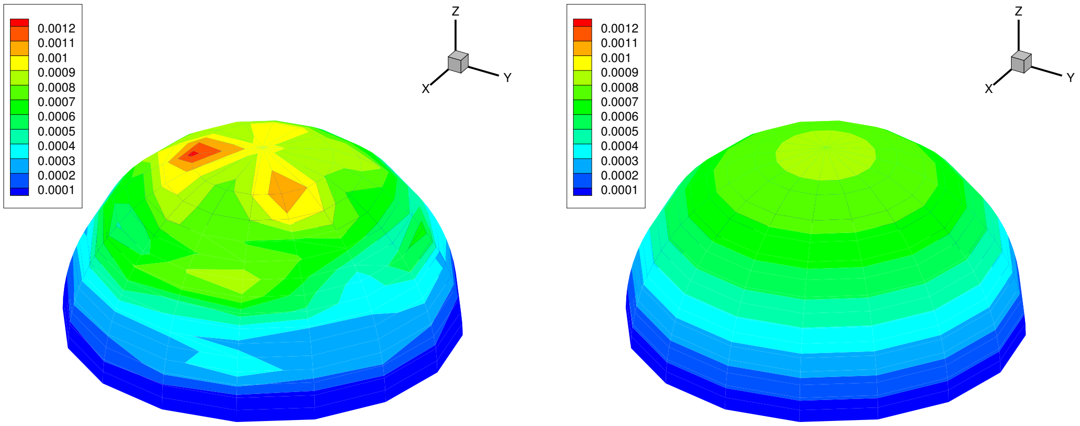

(c) 15° incidence

(d) 15° incidence

Figure 4.6: Differential sputter yields ($\mathrm{mm}^3/\mathrm{C}/\mathrm{sr}$) of condensible species at 100 eV ion energy, 0° and 15° incidence, (left) calculated sputter yields, (right) modified Zhang fits.

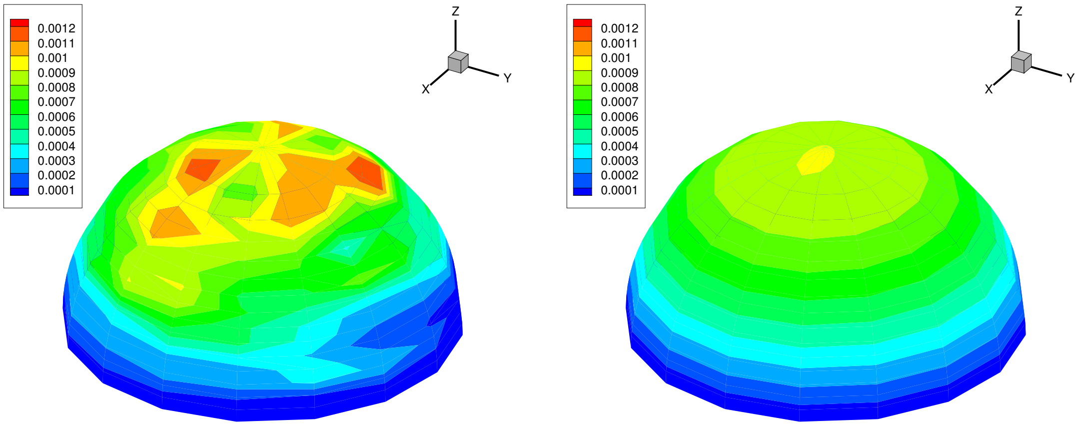

(a) 30° incidence

(b) 30° incidence

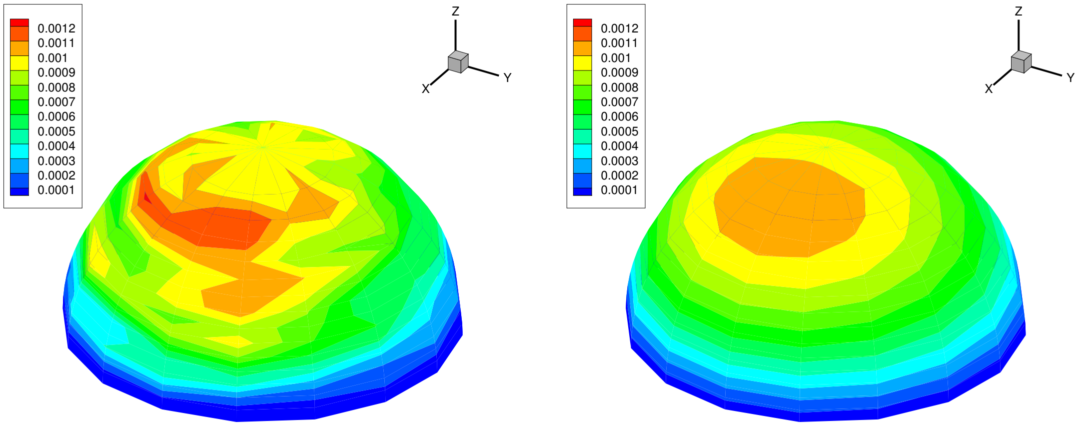

(c) 45° incidence

(d) 45° incidence

Figure 4.7: Differential sputter yields ($\text{mm}^3/\text{C}/\text{sr}$) of condensible species at 100 eV ion energy, 30° and 45° incidence, (left) calculated sputter yields, (right) modified Zhang fits.

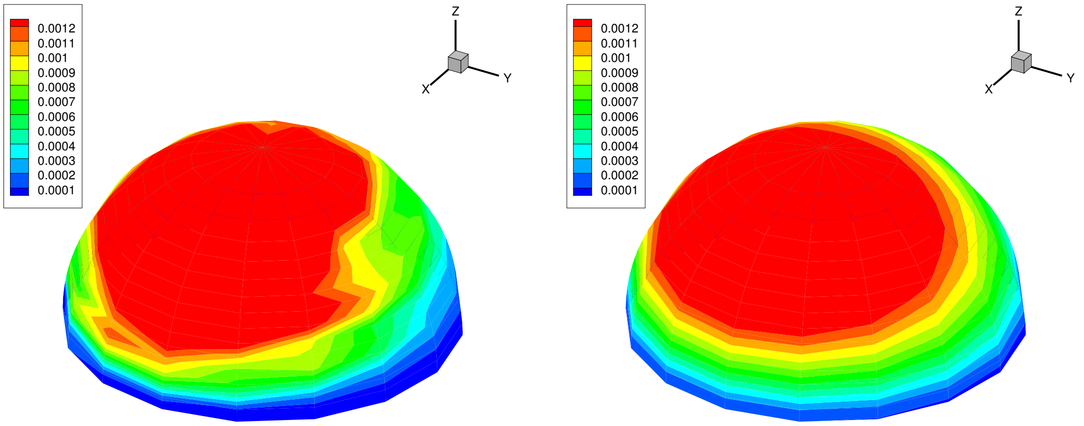

(a) 60° incidence (b) 60° incidence

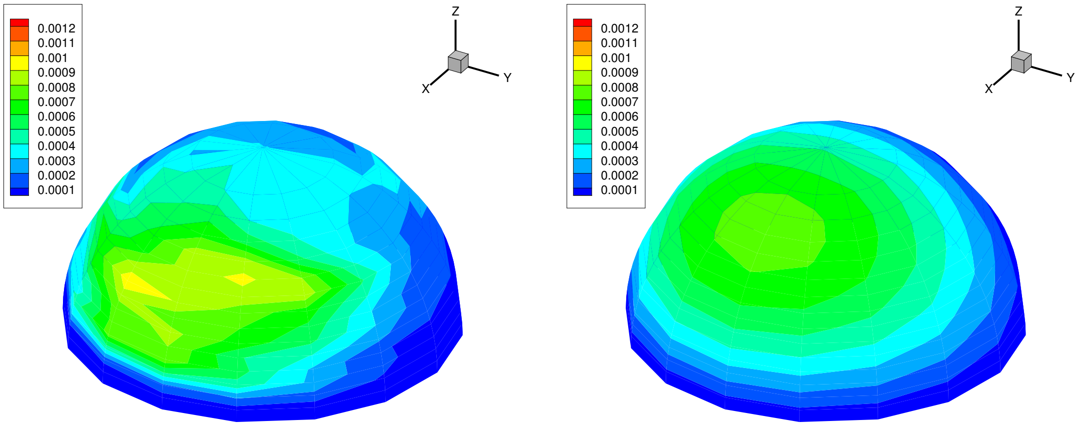

(c) 75° incidence (d) 75° incidence

Figure 4.8: Differential sputter yields ($mm^3/C/sr$) of condensible species at 100 eV ion energy, 60° and 75° incidence, (left) calculated sputter yields, (right) modified Zhang fits.

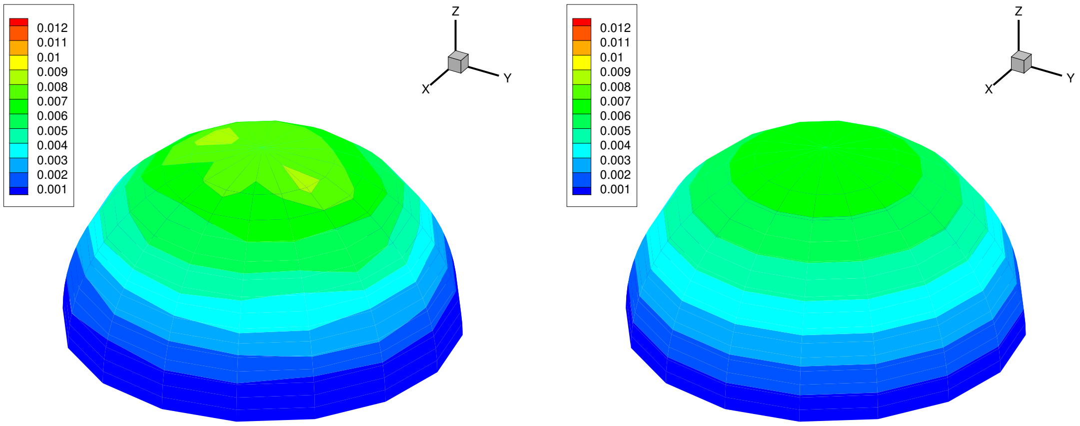

(a) 0° incidence (b) 0° incidence

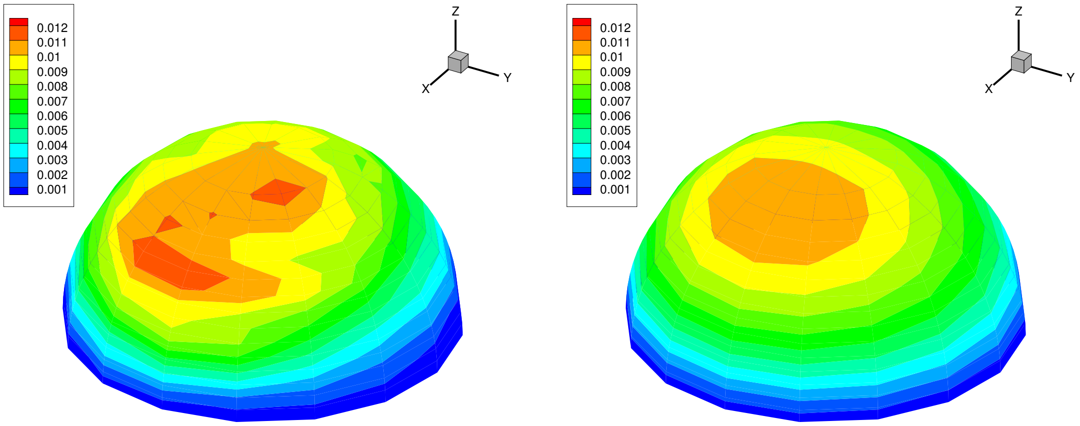

(c) 45° incidence (d) 45° incidence

Figure 4.9: Differential sputter yields ($\mathrm{mm}^3/\mathrm{C}/\mathrm{sr}$) of condensible species at 250 eV ion energy, 0° and 45° incidence, (left) calculated sputter yields, (right) modified Zhang fits.

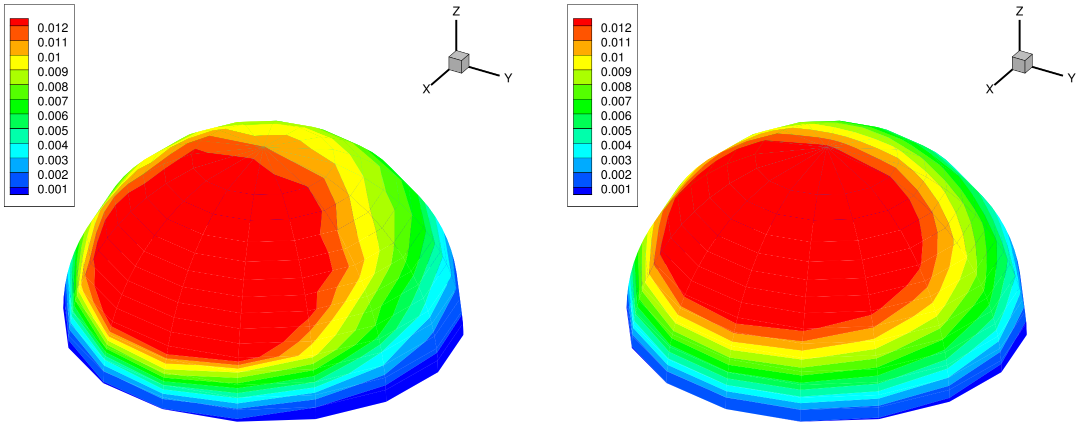

(a) 60° incidence (b) 60° incidence

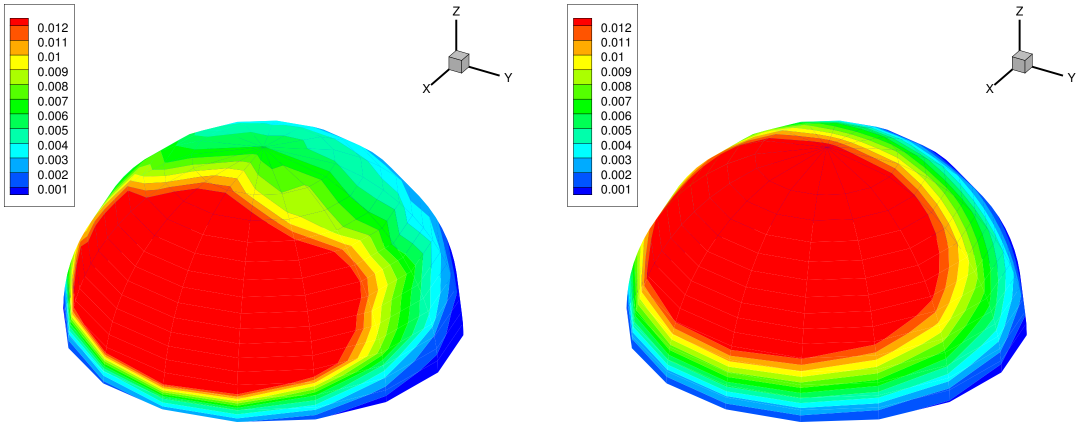

(c) 75° incidence (d) 75° incidence

Figure 4.10: Differential sputter yields ($\mathrm{mm}^3/\mathrm{C}/\mathrm{sr}$) of condensible species at 250 eV ion energy, 60° and 75° incidence, (left) calculated sputter yields, (right) modified Zhang fits.

4.4 Atomic Boron VDFs

4.4.1 Surface Normal Direction

The boron VDF in the direction of the surface normal is fitted with a Sigmund-Thompson velocity distribution function,[19,21] derived from Eq. 2.13:

$$f\left(v_n\right) \propto \frac{v_n^2}{\left(v_n^2 + v_b^2\right)^{3-2m}}, \tag{4.7}$$

where the effective binding velocity v_b is related to the surface binding energy U_b as

$$U_b = \frac{1}{2} m_B v_b^2. \tag{4.8}$$

The calculated VDFs and the fitted Sigmund-Thompson distributions are given in Fig. 4.11 for the cases of 100 eV ions at various incidence angles. Figure 4.12 shows the same data for cases of various ion energies at 60° incidence. The corresponding values of U_b and m are given in Table 4.6. The calculated boron VDFs are captured very well by the Sigmund-Thompson distribution, which is somewhat surprising because Sigmund's sputtering theory was derived for single-component, amorphous materials. As noted above, however, the sputtering of *h*-BN by xenon ions results in an amorphous, boron-enriched structure in the near-surface layers of the lattice. These conditions are similar to the conditions under which Sigmund's theory applies.

Looking at Table 4.6, we see that the surface binding energy falls between 4 eV and 5 eV for most of these simulation cases. At 100 eV ion energy, the results are very consistent between incidence angles, with the binding energy varying only slightly from 3.9 eV to 4.3 eV. For other ion energies at 60° incidence, the resulting binding energies are somewhat less consistent. To examine this behavior further, Fig. 4.13 shows the surface binding energy of boron as a function of incident ion energy. Disregarding the outlying value at 20 eV and 60° incidence, this plot indicates that the calculated bind-

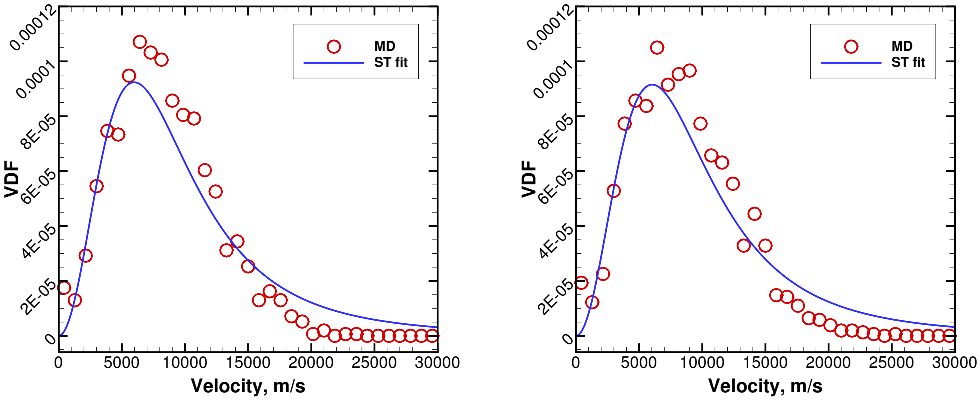

(a) 0° incidence

(b) 15° incidence

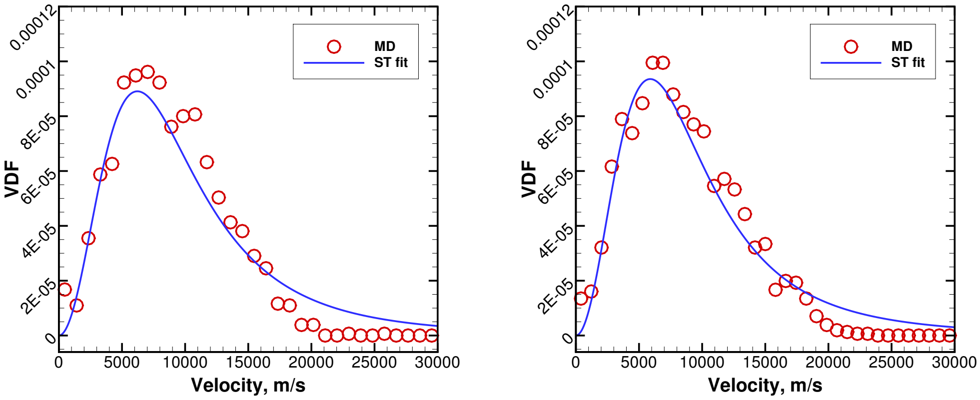

(c) 30° incidence

(d) 45° incidence

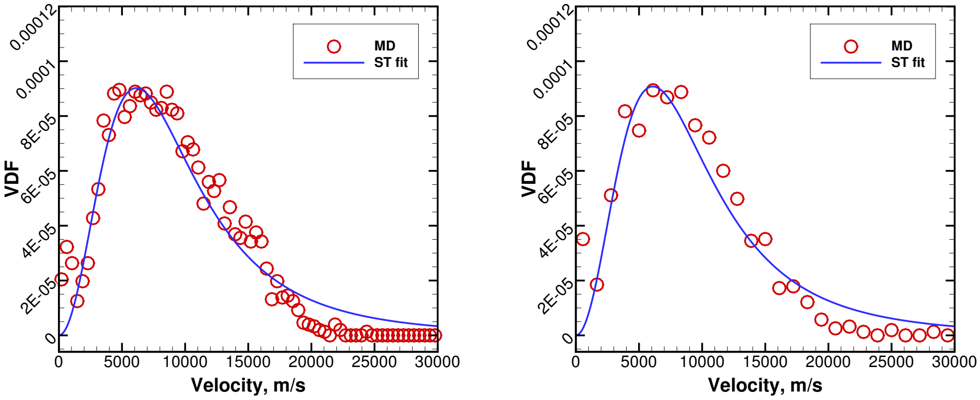

(e) 60° incidence

(f) 75° incidence

Figure 4.11: Velocity distribution functions of sputtered boron atoms normal to the h-BN surface for 100 eV incident ion energy.

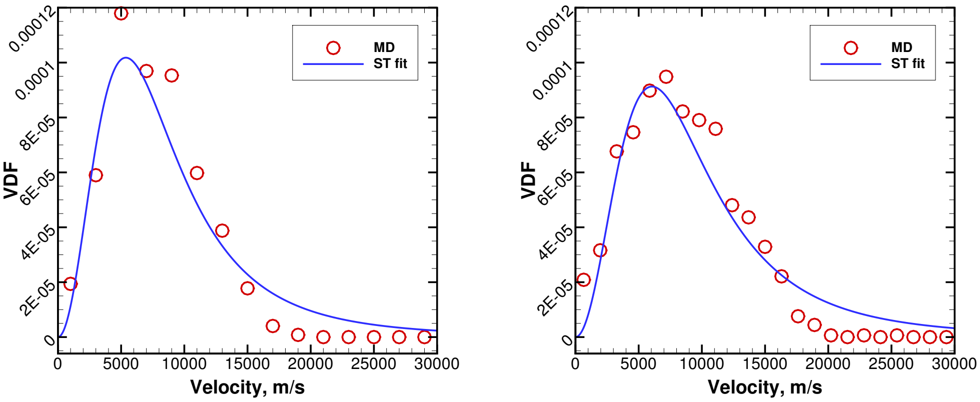

(a) 60 eV (b) 80 eV

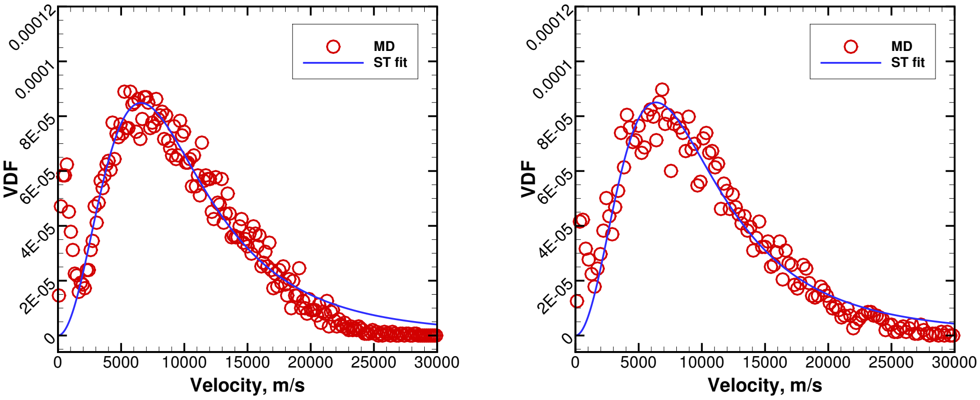

(c) 150 eV (d) 200 eV

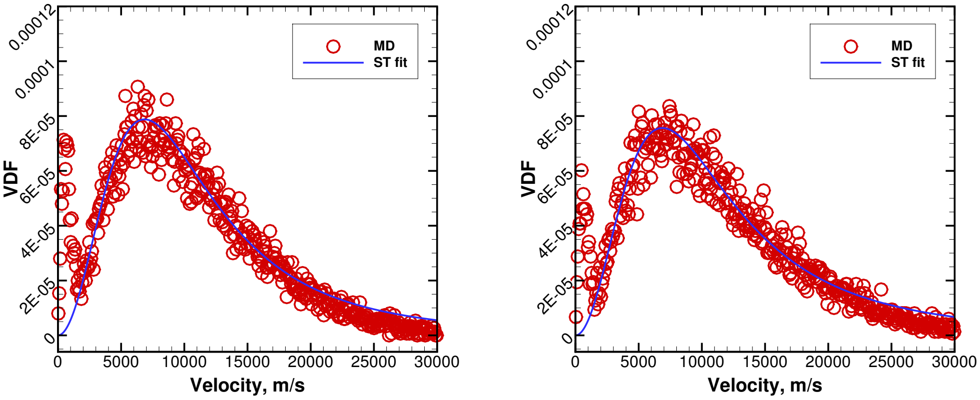

(e) 250 eV (f) 300 eV

Figure 4.12: Velocity distribution functions of sputtered boron atoms normal to the h-BN surface for 60° ion incidence.

Table 4.6: Sigmund-Thompson VDF fit parameters for a subset of MD simulation cases.

Ion energy, eV	Incidence angle	U_b, eV	m
100	0°	4.0	0.0
	15°	4.1	0.0
	30°	4.3	0.0
	45°	3.9	0.0
	60°	4.2	0.0
	75°	4.2	0.0
60	60°	3.2	0.0
80		4.1	0.0
150		4.8	0.0
200		4.2	0.07
250		4.7	0.11
300		4.2	0.21

ing energy decreases as the ion energy decreases starting at about 150 eV. In principle, the surface binding energy is a function only of the material and should be independent of the incident ion's energy, but because the binding energies presented here are calculated from fits to the sputtered particles, the observed dependence makes sense. For very low ion energies, there is less energy available to generate sputtered particles with high speeds. Thus, the VDF of the sputtered particles becomes more biased towards towards low energies, causing the fitted curve to shift as well. Alternatively, one can say that at energies approaching the threshold, the sputtering process no longer falls within the linear cascade regime, so the Sigmund-Thompson distribution is no longer valid and the calculated binding energy loses its physical meaning. Either way, the dependence of the calculated binding energy on the incident ion energy is not a cause for concern, although alternative VDFs may need to be considered for sputtering in the near-threshold regime in the future.

Returning to Table 4.6, we see that the fit parameter m is zero for all except 200–300 eV at 60°, where m increases with energy from 0.07 at 200 eV to 0.21 at 300 eV. Recall from Section 2.1.2 that m is assumed to be a function of the ion energy only.

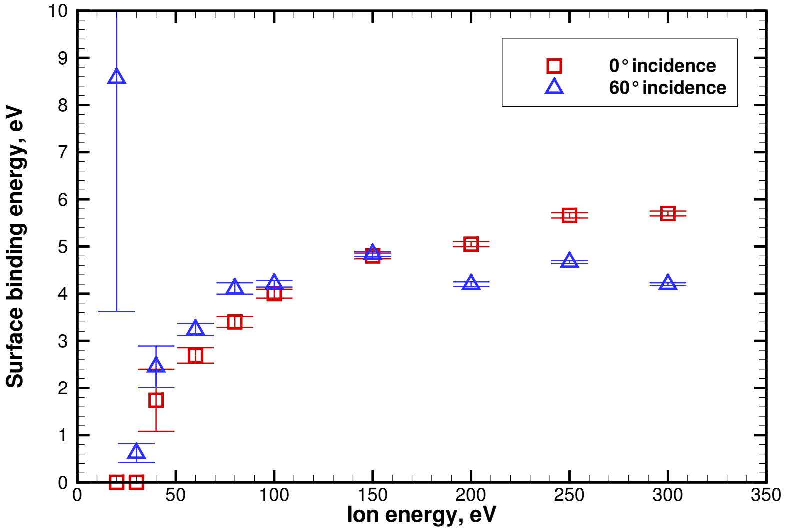

Figure 4.13: Calculated surface binding energy of boron in *h*-BN as a function of incident ion energy. Estimated uncertainty is $^{U_b}/_{\sqrt{N_B}}$.

m controls the decay rate for $v \to \infty$, with larger values of m corresponding to a slower decay rate. At higher ion energies, more energy is available to populate the high-velocity tail of the distribution, so it makes sense that higher energies result in larger values of m. Hence, the observed variation in m is not entirely surprising.

Returning to Figs. 4.11 and 4.12, note that there is a low-energy population of boron atoms that is not captured by the Sigmund-Thompson distribution. This is especially evident in Fig. 4.12 for 150 eV and greater energy. The origin of these particles is not clear, but regardless of the cause, the overwhelming majority of the boron atoms do follow the Sigmund-Thompson distribution, so the influence of these low-energy boron atoms with regards to material transport in Hall thrusters is likely negligible. The existence and possible source of these particles will hence be revisited later on in this chapter.

Tao and Yalin previously investigated the velocity distribution of boron sputtered from an HBR-grade *h*-BN target using laser-induced fluorescence (LIF).[35,36] Their work considered sputtering by both argon and xenon ions and found that the VDF in

Table 4.7: Sigmund-Thompson fit parameters as computed from the MD data and from the LIF measurements from Ref. 36. LIF measurements correspond to sputtering of HBR-grade BN under xenon ion bombardment.

Ion energy, eV	Incidence angle	U_b, eV MD	 LIF, test 1	 LIF, test 2
100	0°	4.0 ± 0.1	4.5 ± 0.6	5.0 ± 0.6
200	0°	5.1 ± 0.1	4.8 ± 0.3	4.8 ± 0.4
300	0°	5.7 ± 0.1	4.8 ± 0.4	4.8 ± 0.4
300	60°	4.2 ± 0.03	4.3 ± 0.4	—

the surface normal direction matched the Sigmund-Thompson distribution. The MD results for the surface binding energy are compared with Tao's results for sputtering by xenon in Table 4.7. The presented uncertainty in the calculated binding energies is evaluated as ${}^{U_b}/_{\sqrt{N_B}}$. Although the MD results appear less consistent than the LIF measurements, both sets of data agree that the binding energy of boron in *h*-BN is between 4 eV and 6 eV. In a parametric study, however, Tao found that the surface binding energy varied from 3.9 eV to 7.2 eV as m was varied from 0 to 0.3, and ultimately settled on $m \approx 0.2$.[35] The MD results fall within these bounds, but no parametric study with regard to the value of m has yet been performed.

It is also useful to consider the average surface binding energy computed from the MD data and from the LIF measurements. Tao reports an average binding energy of 4.8 eV from his measurements. The average value of U_b over all MD simulation cases is 3.9 eV, about 19% smaller than the experimental value. If cases where the ion energy is less than 100 eV are ignored, then the average binding energy from the MD simulations is 4.5 eV, or only 6% smaller than the experimental value. Tao did not investigate ion energies lower than 100 eV, so the latter comparison makes more sense. Thus, it seems that the MD model is resulting in surface binding energies for boron that are consistent with the experimental measurements.

4.4.2 Forward Sputtering Direction

The direction of forward sputtering is given by the unit vector $\hat{\mathbf{p}}$ such that $\mathbf{v}_i \cdot \hat{\mathbf{p}} = |\mathbf{v}_i| \sin\theta_i$. In other words, it is the axis in the plane of the *h*-BN surface that, along with the normal vector $\hat{\mathbf{n}}$, defines the plane in which the incident ion's velocity vector resides. The curve fit to the boron VDF along this direction is a Maxwell-Boltzmann distribution function.

Figure 4.14 shows the calculated VDFs and the Maxwellian fits for the cases of 100 eV at all tested angles of incidence. Similarly, Fig. 4.15 shows the VDFs for various ion energies at 60° incidence. The mean velocity and fit temperature for each case shown are given in Table 4.8. Note that the calculated VDFs are not perfectly Maxwellian. First, the low-velocity population seen in Figs. 4.11 and 4.12 appears here as well. These particles may follow their own Maxwell-Boltzmann distribution with a lower temperature, but their origin is still unknown. There is also some deviation from a Maxwellian in the tail for high positive velocity. This is particularly evident from Fig. 4.15 for ion energies 150 eV and greater. In those distributions, the tail decays in what appears to be a linear fashion compared to the $\exp(-v^2)$ decay in the Maxwellian. This results in more high-energy particles than would otherwise be expected. It is possible that a bi-Maxwellian fit would account for the populations near zero velocity and at high positive velocity, but for the sake of simplicity a plain Maxwellian is assumed to be adequate for this work.

From Fig. 4.14 and Table 4.8, we see that the mean velocity in the forward sputtering direction increases with the ion incidence angle. This was previously observed in the differential sputter yields, and is simply an indication that forward sputtering is preferred for oblique angles of incidence. The temperature also increases with ion incidence angle, suggesting that at higher ion energies, more of the incident ion's energy is transferred into the thermal energy of the sputtered particles. This makes sense simply because more energy is available at higher ion energies, and one would

Table 4.8: Maxwellian mean velocity and temperature along the forward sputtering direction for a subset of MD simulation cases.

Ion energy, eV	Incidence angle	$\bar{v}$, m/s	T, K
100	0°	-14.8	49,400
	15°	218	49,700
	30°	99.8	59,900
	45°	1260	78,300
	60°	2210	82,900
	75°	6240	113,000
60	60°	3390	68,400
80		3320	76,700
150		2800	100,000
200		3060	111,000
250		2980	112,000
300		2720	118,000

expect this to manifest as the ejection of additional particles, more massive particles, or particles with greater energy.

Looking at Fig. 4.15 and Table 4.8, we see that the mean velocity along the forward sputtering direction is approximately constant with energy for a fixed angle of incidence. This is certainly expected for normal incidence where the mean velocity should be approximately zero, but is somewhat surprising for oblique angles of incidence. The temperature, however, increases substantially with ion energy at a fixed incidence angle, nearly doubling between 60 eV and 300 eV. This suggests that the additional energy supplied by higher-energy ions is preferentially deposited into the thermal energy of the sputtered particles along the forward sputtering axis rather than into a bulk flow.

4.4.3 Transverse Sputtering Direction

The transverse sputtering direction is defined by the unit vector $\hat{\mathbf{t}}$ in the plane of the h-BN surface such that $\mathbf{v}_i \cdot \hat{\mathbf{t}} = 0$. As with the forward sputtering direction, the boron VDF in this direction is fit with a Maxwell-Boltzmann distribution. However,

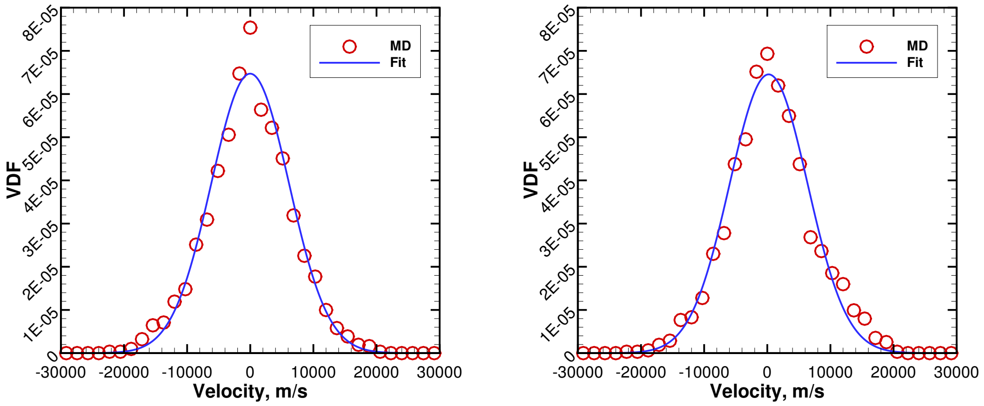

(a) 0° incidence

(b) 15° incidence

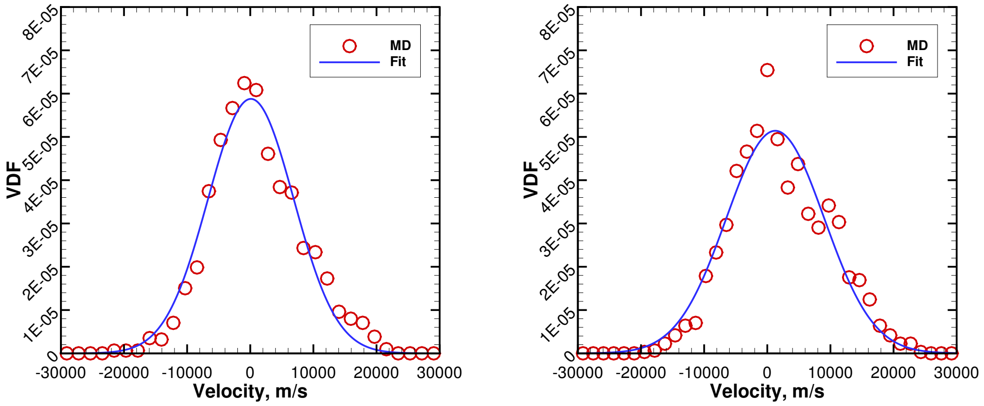

(c) 30° incidence

(d) 45° incidence

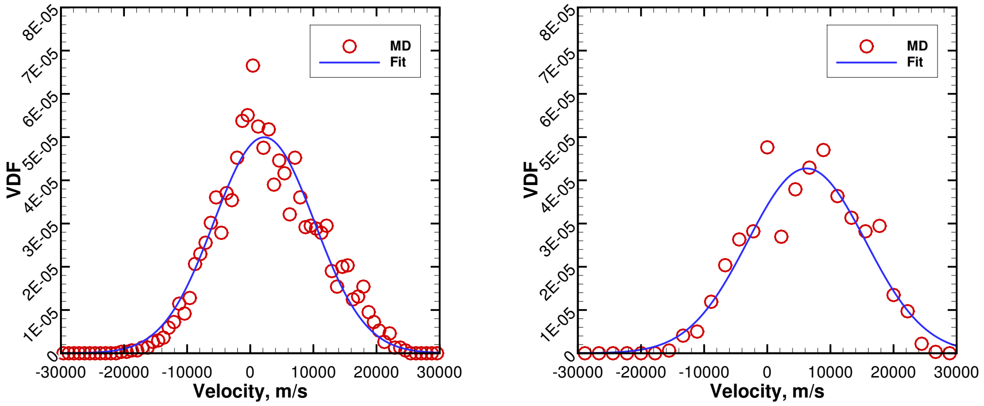

(e) 60° incidence

(f) 75° incidence

Figure 4.14: Velocity distribution functions of sputtered boron atoms along the forward sputtering axis for 100 eV incident ion energy.

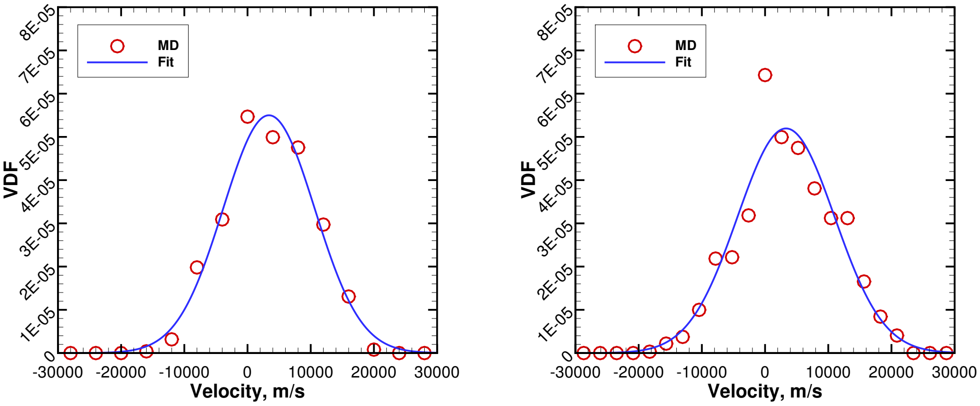

(a) 60 eV

(b) 80 eV

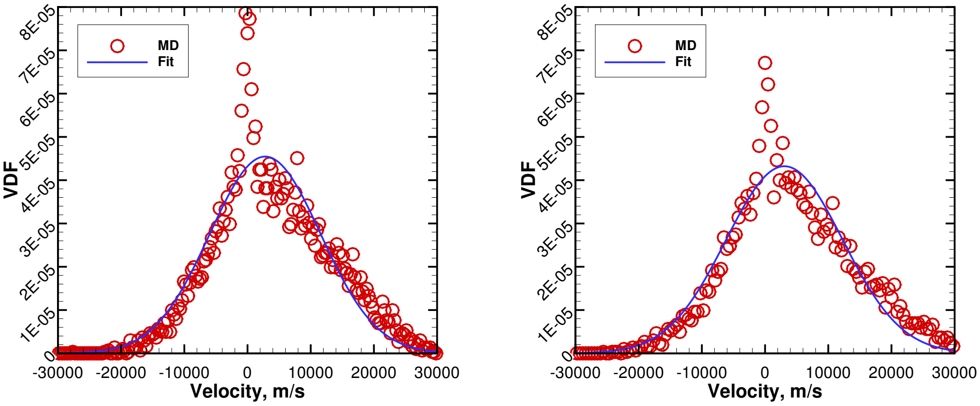

(c) 150 eV

(d) 200 eV

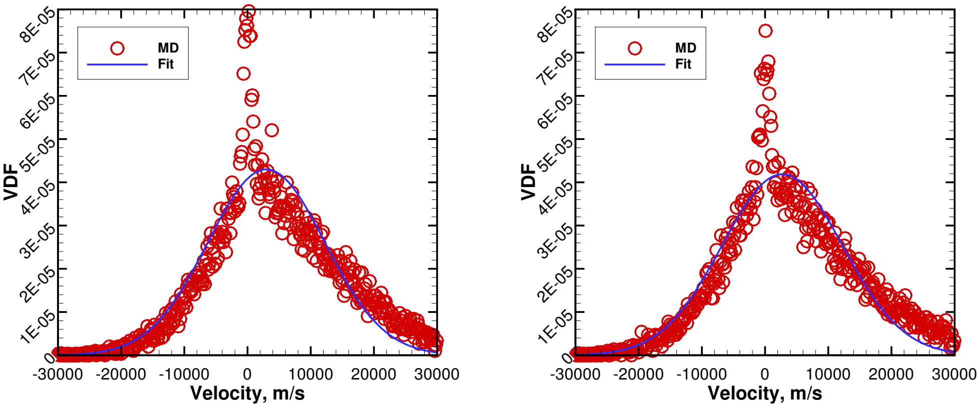

(e) 250 eV

(f) 300 eV

Figure 4.15: Velocity distribution functions of sputtered boron atoms along the forward sputtering axis for 60° ion incidence.

Table 4.9: Maxwellian mean velocity and temperature along the transverse sputtering direction for a subset of MD simulation cases.

Ion energy, eV	Incidence angle	$\bar{v}$, m/s	T, K
100	0°	-339	54,600
	15°	109	49,100
	30°	-38.3	53,300
	45°	346	63,500
	60°	57.5	63,300
	75°	17.9	79,900
60	60°	-225	64,400
80		87.9	61,500
150		89.0	67,100
200		-195	77,400
250		15.5	77,500
300		44.7	85,300

the mean velocity is expected to be zero in the transverse sputtering direction for all ion energies and angles of incidence.

Figure 4.16 shows the calculated VDFs and the Maxwellian fits in the transverse sputtering direction, and Fig. 4.17 shows the VDFs for various ion energies at 60° incidence. The corresponding fit parameters are given in Table 4.9. As in the surface normal and forward sputtering directions, there is a distinct population of boron atoms with very low velocities. At the extreme ends of the distribution, the fitted Maxwellian deviates from the calculated VDF, perhaps indicating that the temperature of the fit is too small. As with the forward sputtering direction, it is possible that a bi-Maxwellian fit could account for both the low-velocity and high-velocity populations, but a single Maxwellian is assumed to be adequate at present.

Looking at Table 4.9, we see that the mean velocity is within a few hundred meters per second of the expected value of zero for all displayed simulation cases. The temperature increases with both incidence angle and energy, although not quite as quickly as in the forward sputtering direction. This again suggests that more of the ion energy is deposited into the thermal energy of the sputtered boron atoms with

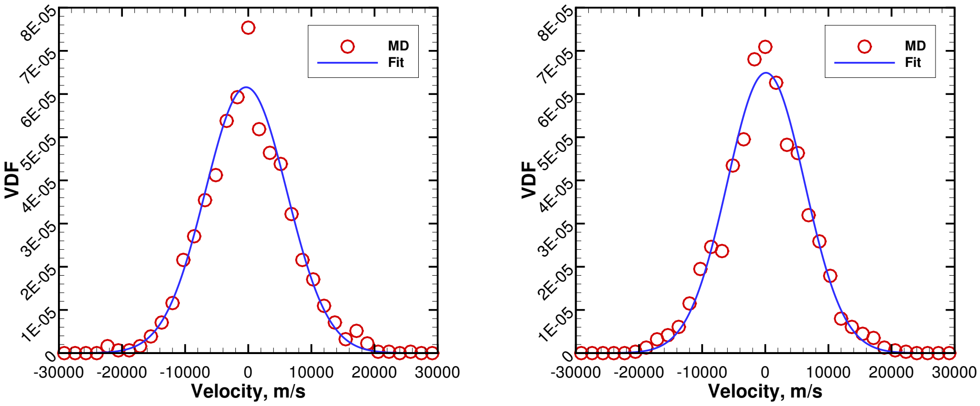

(a) 0° incidence (b) 15° incidence

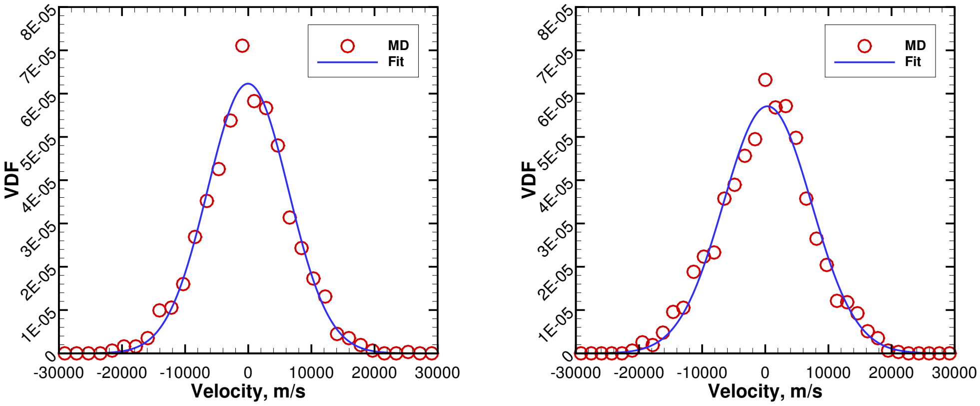

(c) 30° incidence (d) 45° incidence

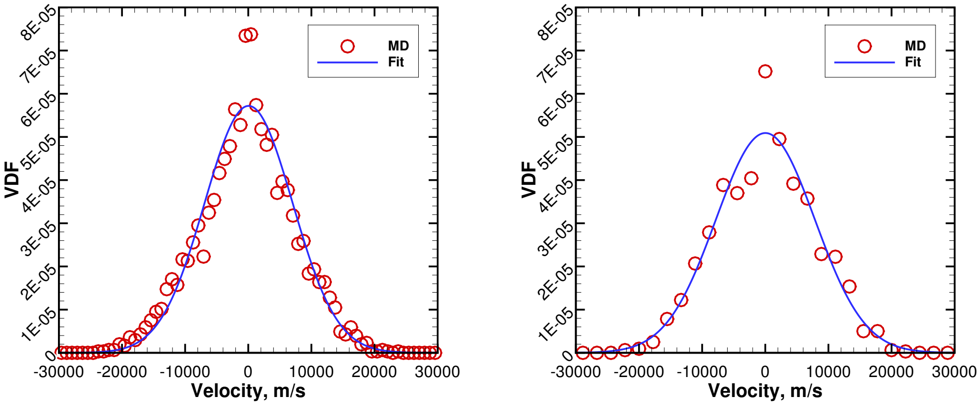

(e) 60° incidence (f) 75° incidence

Figure 4.16: Velocity distribution functions of sputtered boron atoms along the transverse sputtering direction for 100 eV incident ion energy.

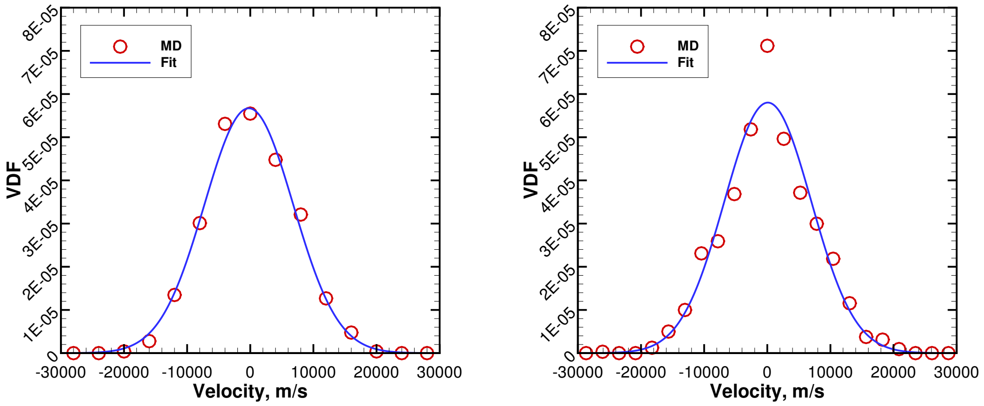

(a) 60 eV

(b) 80 eV

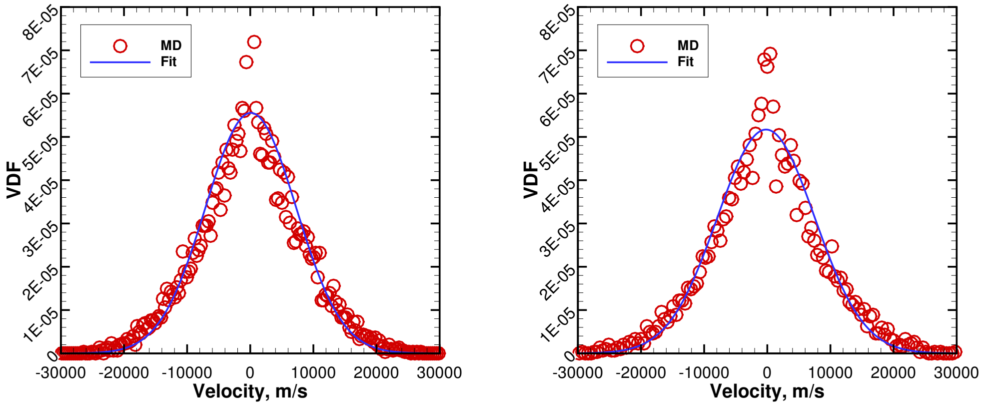

(c) 150 eV

(d) 200 eV

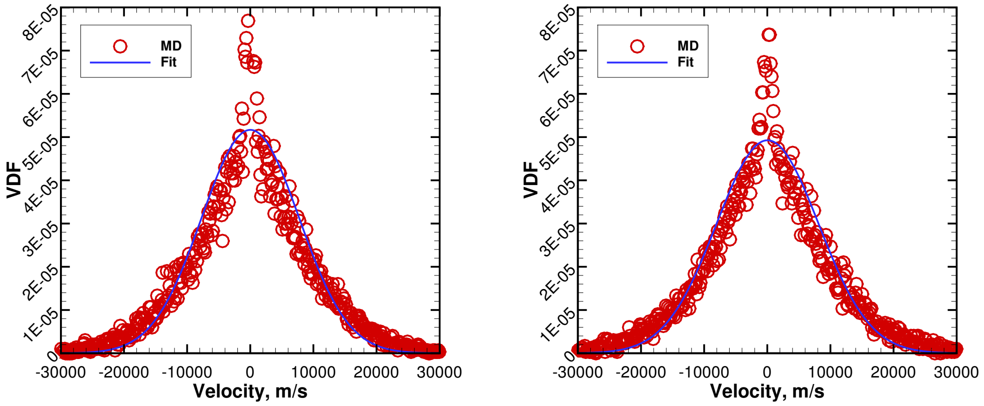

(e) 250 eV

(f) 300 eV

Figure 4.17: Velocity distribution functions of sputtered boron atoms along the transverse sputtering direction for 60° ion incidence.

increasing energy and incidence angle.

Although not necessarily a cause for concern at present, the consistent appearance of a population of low-energy boron atoms throughout the calculated VDFs is worth noting. Tao's LIF measurements provide no evidence of such a distinct population of atoms, so their appearance in the simulations is most likely nonphysical. The origin of these atoms is not known, but one possibility is that they are a consequence of the lattice pre-conditioning algorithm described in the previous chapter. Because this algorithm perturbs the lattice atoms stochastically in order to achieve a local minimum in the system potential energy, it is likely that the resulting surface structure is not entirely representative of a surface that has undergone persistent ion bombardment. For example, there may be some features that include some very loosely bound atoms that are easily removed from the lattice even with very little energy transfer, resulting in a free low-energy atom. This hypothesis can be easily tested by running several sputtering simulations starting from a perfect *h*-BN lattice, but given the computational cost of the simulations, this is left for future work.

4.5 Summary

In this chapter, we discussed the results of the MD model for sputtering of *h*-BN by xenon ions, including the chemical composition of the sputtered particles, the integrated sputter yields, the differential sputter yields, and the 3D VDF of the sputtered particles. It was determined that the most prevalent condensible product of *h*-BN sputtering is atomic boron. Furthermore, it was found that the sputtered boron atoms follow the Sigmund-Thompson velocity distribution predicted by Sigmund's linear cascade theory in the direction normal to the *h*-BN surface. The VDFs of the sputtered boron in the forward and transverse sputtering directions were found to obey Maxwell-Boltzmann distributions. A distinct population of low-energy boron atoms with unknown origin was also found to exist, but the cause and behavior of these atoms is left for future investigation.

The integrated sputter yields found from the MD model show good agreement with the available experimental data, but the model would benefit from further validation. It is particularly important to establish domain independence for ion energies 300 eV and greater, as there is an abundance of experimental data available for comparison in that range of energies. However, the present set of sputter yields is more than adequate for inclusion in a Hall thruster plasma model. The next chapter describes the numerical model used to simulate the thruster plasma and the implementation of the calculated sputter yields and sputtered boron properties.

CHAPTER V

Hall Thruster Plasma Model

In order to analyze the problem of material transport in Hall thrusters, the *h*-BN sputter yields and sputtered particle properties must be implemented within a plasma model. The model ultimately chosen for use in the present work is HPHall. Initially developed by Fife and Martínez-Sánchez in the late 1990s,[51] HPHall has been modified by several researchers over the past decade with the goal of expanding its capabilities.[71–78] It has also been applied many times to model wall erosion in Hall thrusters,[15,25,26,56] giving it a strong heritage and making it an ideal tool for use in this work.

What follows below is a brief description of HPHall and a detailed discussion of the updates made to the model. This is not meant as a comprehensive overview of HPHall and its implementation, but rather as a summary of the physics that are most relevant to the problem of wall erosion and material transport. For a more detailed description of HPHall, please see the referenced publications.

5.1 Governing Equations

In HPHall, the electrons are treated as a fluid whose conservation laws are solved on a coordinate system defined by the magnetic field, whereas the ions and neutral atoms are modeled using a 2D axisymmetric particle-in-cell (PIC) technique. The local plasma density is set by the PIC submodel with the assumption of quasineutrality, which takes the place of the electron continuity equation:

$$n_e = \sum_Z Z n_{i,Z+}, \tag{5.1}$$

where Z denotes the charge state of the ion species, and the number density of each ion species is computed from a first-order PIC weighting.[47,48,51,74] As of the start of this work, charge states up to $Z = 2$ were included in HPHall. The plasma potential and electron temperature are determined by solving the electron momentum and energy conservation equations and a generalized form of Ohm's law. The electric field can then be derived from the plasma potential and the heavy species' equations of motion can be integrated in time.

5.1.1 Magnetic Field

The magnetic field can be used to define a coordinate system for the electrons. In general, the magnetic field obeys Maxwell's equations:

$$\nabla \cdot \mathbf{B} = 0, \tag{5.2}$$

$$\nabla \times \mathbf{B} = \mu_0 \left(\mathbf{J} + \varepsilon_0 \frac{\partial \mathbf{E}}{\partial t} \right). \tag{5.3}$$

In Hall thrusters, the induced magnetic fields are much smaller than the applied field from the electromagnets, so Eq. 5.3 becomes

$$\nabla \times \mathbf{B} = 0. \tag{5.4}$$

Fife defines the magnetic potential function σ[51] such that

$$\mathbf{B} = \nabla \sigma. \tag{5.5}$$

Substituting this into Eq. 5.2 gives (in cylindrical polar coordinates)

$$\nabla^2 \sigma = \frac{\partial^2 \sigma}{\partial z^2} + \frac{\partial^2 \sigma}{\partial r^2} + \frac{1}{r}\frac{\partial \sigma}{\partial r} = 0. \tag{5.6}$$

Fife then defines a magnetic stream function λ with a gradient that is everywhere normal to $\mathbf{B}$:

$$\nabla \lambda = r\left(B_r \hat{\mathbf{z}} - B_z \hat{\mathbf{r}}\right). \tag{5.7}$$

Finally, if $\hat{n}$ and $\hat{t}$ define the coordinates normal and parallel to the magnetic field lines, respectively, then derivatives in $\hat{n}$ can be written as

$$\frac{\partial}{\partial \hat{n}} = \frac{\partial \lambda}{\partial \hat{n}}\frac{\partial}{\partial \lambda} = -rB\frac{\partial}{\partial \lambda}. \tag{5.8}$$

5.1.2 Electron Equations

5.1.2.1 Momentum Conservation Along Field Lines

Ignoring viscous effects, the momentum equation for the electron fluid can be written as

$$\frac{\partial\left(n_e \mathbf{u}_e\right)}{\partial t} + \nabla \cdot \left(n_e \mathbf{u}_e \mathbf{u}_e\right) + \nabla \frac{p_e}{m_e} = -\frac{n_e e}{m_e}\left(\mathbf{E} + \mathbf{u}_e \times \mathbf{B}\right). \tag{5.9}$$

The electrons have very low mass and thus respond very quickly to the electric and magnetic fields, so the inertia terms can be neglected. The momentum equation in the direction along magnetic field lines is then

$$\frac{\partial p_e}{\partial \hat{t}} = -e n_e E_{\hat{t}}. \tag{5.10}$$

Substituting $\mathbf{E} = -\nabla\phi$ and assuming $p_e = n_e k_B T_e$, one finds

$$\frac{\partial}{\partial \hat{t}} \left(n_e k_B T_e \right) = e n_e \frac{\partial \phi}{\partial \hat{t}}. \tag{5.11}$$

Finally, it is assumed that the electrons are in thermal equilibrium along magnetic field lines, so $T_e = T_e\left(\lambda\right)$. Integrating Eq. 5.11 then gives

$$\phi^* \left(\lambda\right) = \phi - \frac{k_B T_e \left(\lambda\right)}{e} \ln \left(\frac{n_e}{n_{e,0}} \right). \tag{5.12}$$

where $n_{e,0}$ is the electron density at some reference point along the magnetic field line given by λ.

Equation 5.12 is known as the *thermalized potential approximation*, and it allows the calculation of the electrostatic potential ϕ so long as the thermalized potential ϕ^*, electron temperature T_e, and electron density n_e are known. The electron density is determined from the assumption of quasineutrality. Hence, at least two more equations are needed to determine T_e, ϕ^*, and ϕ.

5.1.2.2 Ohm's Law Across Field Lines

The cross-field motion of the electrons is assumed to follow Ohm's law. In this formulation, the cross-field current density of electrons is given by

$$J_{e,\hat{n}} = -e n_e u_{e,\hat{n}} = \sigma_{e,\perp} \left(E_{\hat{n}} + \frac{1}{e n_e} \frac{\partial p_e}{\partial \hat{n}} \right), \tag{5.13}$$

where $\sigma_{e,\perp}$ is the cross-field electrical conductivity, from which one can derive the cross-field electron mobility:

$$\mu_{e,\perp} = \frac{\sigma_{e,\perp}}{e n_e}. \tag{5.14}$$

Substituting $p_e = n_e k_B T_e$ and $\mathbf{E} = -\nabla\phi$ gives

$$u_{e,\hat{n}} = -\mu_{e,\perp} \left(\frac{k_B T_e}{e n_e} \frac{\partial n_e}{\partial \hat{n}} + \frac{k_B}{e} \frac{\partial T_e}{\partial \hat{n}} - \frac{\partial \phi}{\partial \hat{n}} \right). \tag{5.15}$$

Differentiating Eq. 5.12 gives an expression for $\frac{\partial \phi}{\partial \hat{n}}$:

$$\frac{\partial \phi}{\partial \hat{n}} = \frac{\partial \phi^*}{\partial \hat{n}} + \frac{k_B \ln\left(\frac{n_e}{n_{e,0}}\right)}{e} \frac{\partial T_e}{\partial \hat{n}} + \frac{k_B T_e}{e n_e} \frac{\partial n_e}{\partial \hat{n}}. \tag{5.16}$$

So, Eq. 5.15 becomes

$$u_{e,\hat{n}} = \mu_{e,\perp} \left[\frac{\partial \phi^*}{\partial \hat{n}} + \frac{k_B}{e} \left(\ln\left(\frac{n_e}{n_{e,0}}\right) - 1 \right) \frac{\partial T_e}{\partial \hat{n}} \right], \tag{5.17}$$

or, using the identity given in Eq. 5.8:

$$u_{e,\hat{n}} = -\mu_{e,\perp} r B \left[\frac{\partial \phi^*}{\partial \lambda} + \frac{k_B}{e} \left(\ln\left(\frac{n_e}{n_{e,0}}\right) - 1 \right) \frac{\partial T_e}{\partial \lambda} \right]. \tag{5.18}$$

Because both ϕ^* and T_e are constant along magnetic field lines, their derivatives with respective to λ are also constant along field lines. This allows us to simplify any integrals along magnetic field lines by moving these derivatives outside of the integral.

5.1.2.3 Cross-Field Mobility

The cross-field mobility of the electrons in a Hall thruster is not very well known. A classical analysis suggests that the electrons are confined to the magnetic field lines until they undergo a collision event, causing the guiding center of the electron's motion to shift to another field line. The degree to which the electrons are confined is described by the Hall parameter:

$$\Omega_e = \frac{\omega_{ce}}{\nu_e} = \frac{eB}{m_e \nu_e}, \tag{5.19}$$

where ν_e is the total electron collision frequency. When the Hall parameter is large, the electrons complete many gyro cycles before a collision, indicating that the electrons are well-confined. The classical form of the cross-field electron mobility is given by

$$\mu_{e,\perp} = \frac{e}{m_e \nu_e} \frac{1}{1 + \Omega_e^2} \approx \frac{m_e \nu_e}{e B^2}, \tag{5.20}$$

when Ω_e is large, as is the case in Hall thrusters. However, this form of the mobility tends to underestimate the electron current collected by the anode in a real Hall thruster. The additional current observed in real thrusters is called the anomalous electron current, and its cause is presently unknown. Hence, Hall thruster models frequently attempt to capture the anomalous current by adding empirical terms to the electron governing equations.

HPHall seeks to capture the anomalous electron drift by including an additional term in the collision frequency:

$$\nu_e = \nu_{ei} + \nu_{en} + \nu_w + \nu_B, \tag{5.21}$$

where ν_{ei} is the electron-ion collision frequency, ν_{en} is the electron-neutral collision frequency, ν_w is the electron-wall collision frequency, and ν_B is the anomalous Bohm collision frequency. The anomalous collision frequency is given by

$$\nu_B = \frac{\alpha}{16} \frac{eB}{m_e}, \tag{5.22}$$

where α is an empirical parameter. In the original version of HPHall, the value of α was constant throughout the simulation domain, with $\alpha \in [0, 1]$. Hofer *et al.* added a two-region model where the value of α is set independently in each region,[15,72,75] and later extended this to a three-region model,[76] where

$$\alpha = \begin{cases} \alpha_c, & \lambda \leq \lambda_1 \\ \alpha_c f_{12}\left(\lambda_2, \lambda\right) + \alpha_e f_{12}\left(\lambda, \lambda_1\right), & \lambda_1 < \lambda \leq \lambda_2 \\ \alpha_e, & \lambda_2 < \lambda \leq \lambda_3 \\ \alpha_e f_{34}\left(\lambda_4, \lambda\right) + \alpha_p f_{34}\left(\lambda, \lambda_3\right), & \lambda_3 < \lambda \leq \lambda_4 \\ \alpha_p, & \lambda > \lambda_4 \end{cases}, \tag{5.23}$$

$$f_{12}\left(\lambda_a, \lambda_b\right) = \left|\frac{\lambda_a - \lambda_b}{\lambda_2 - \lambda_1}\right|, \tag{5.24}$$

$$f_{34}\left(\lambda_a, \lambda_b\right) = \left|\frac{\lambda_a - \lambda_b}{\lambda_4 - \lambda_3}\right|, \tag{5.25}$$

and the bounding values of λ are determined at runtime from user-specified reference points. The subscripts c, e, and p stand for channel, exit, and plume, respectively.

5.1.2.4 Current Conservation

Because quasineutrality is imposed in HPHall, charge cannot accumulate and the total current must therefore be conserved. In other words, the current collected by the anode must be equal to the sum of the bulk ion current, bulk electron current, and near-wall electron current at any location in the thruster:

$$I_a = I_i + I_a + I_w. \tag{5.26}$$

Written in terms of integrals alone magnetic field lines, this becomes

$$I_a = -2\pi e \int_0^{\ell} n_i u_{i,\hat{n}} r ds + 2\pi e \int_0^{\ell} n_e u_{e,\hat{n}} r ds + I_w, \tag{5.27}$$

where ds is a differential length element along the magnetic-field line. Substituting

Eq. 5.18 and rearranging terms gives the form[51]

$$\frac{\partial \phi^*}{\partial \lambda} = \frac{-I_a + I_w - 2\pi k_B \frac{\partial T_e}{\partial \lambda} \int_0^\ell n_e \mu_{e,\perp} B \left(\left(\ln \left(\frac{n_e}{n_{e,0}} \right) - 1 \right) \right) r^2 ds - 2\pi e \int_0^\ell n_i u_{i,\hat{n}} r ds}{2\pi e \int_0^\ell n_e \mu_{e,\perp} B r^2 ds}. \tag{5.28}$$

5.1.2.5 Energy Conservation

The electron energy equation is given by

$$\frac{\partial}{\partial t}\left(\frac{3}{2} n_e k_B T_e\right) + \nabla \cdot \left(\frac{5}{2} n_e k_B T_e \mathbf{u}_e + \mathbf{q}_e\right) - \mathbf{u}_e \cdot \nabla \left(n_e k_B T_e\right) = S_e - S_i, \tag{5.29}$$

where it is again assumed that $p_e = n_e k_B T_e$, $\mathbf{q}_e$ is the thermal conduction vector, and S_e and S_i are the elastic source term and inelastic sink term, respectively. The inelastic sink term is discussed in a later section, and the elastic source term is discussed in Ref. 51.

5.1.2.6 Wall Sheath

The presence of the wall sheath is of critical importance in erosion studies, as the potential drop through the sheath both accelerates the ions towards the wall and also shifts their trajectories towards normal incidence. The sheath model in HPHall is based on the work of Hobbs and Wesson.[79,80] This model calculates the sheath potential in the presence of secondary electron emission (SEE). The potential profile through the sheath comes from a solution of the Poisson equation:

$$\begin{aligned} \frac{1}{2\varepsilon_0 n_0 k_B T_e}\left(\frac{\partial \phi}{\partial x}\right)^2 = \frac{2\mathcal{E}_0}{k_B T_e}&\left[\left(1 - \frac{e\phi}{\mathcal{E}_0}\right)^{1/2} - 1\right] \\ &+ \frac{2\gamma}{1-\gamma}\left(-\frac{m_e}{m_i}\frac{\mathcal{E}_0}{k_B T_e}\frac{e\phi_0}{k_B T_e}\right)^{1/2}\left[\left(1 - \frac{\phi}{\phi_0}\right)^{1/2} - 1\right] \\ &+ \left[1 - \frac{\gamma}{1-\gamma}\left(-\frac{m_e}{m_i}\frac{\mathcal{E}_0}{e\phi_0}\right)^{1/2}\right]\left[\exp\left(\frac{e\phi}{k_B T_e}\right) - 1\right], \end{aligned} \tag{5.30}$$

where ϕ_0 is the potential at the wall, γ is the secondary electron yield, and $\mathcal{E}_0$ is the minimum ion energy at the sheath edge, set from the Bohm criterion. This equation has been solved numerically to determine the wall potential as a function of the secondary electron yield, and HPHall uses a curve fit to the numerical solution:[75]

$$\phi_0 = \frac{k_B T_e}{e}\left[\ln\left(A\left(1-\gamma\right)\right) - \frac{B}{\left(1-\gamma\right)^2} - \frac{C}{\left(1-\gamma\right)^3} - \frac{D}{\left(1-\gamma\right)^4}\right]. \tag{5.31}$$

Table 5.1: Fit parameters for Eq. 5.31.

A	B	C	D
195.744	1.28971×10^{-4}	-3.45464×10^{-6}	3.68507×10^{-8}

The values of the fit parameters are given in Table 5.1. The SEE yield is determined from one of two functional forms:

$$\gamma\left(T_e\right) = \Gamma\left(2+b\right) a \left(\frac{2k_B T_e}{e}\right)^b, \tag{5.32}$$

$$\gamma\left(T_e\right) = a + \frac{\left(1-a\right)\left(\frac{2k_B T_e}{e}\right)}{b}, \tag{5.33}$$

where $\Gamma\left(x\right)$ is the gamma function and a and b are given in Table 5.2.

Table 5.2: Fit parameters for the SEE yields as a function of electron temperature.

Equation	a	b
Eq. 5.32	0.123	0.528
Eq. 5.33	0.54	40.0

5.1.3 Heavy Species

The motion of the heavy species is governed by Newton's second law in cylindrical polar coordinates. However, it is assumed that the plasma flow is axisymmetric, so the θ component of the particle positions can be ignored. Thus, a 2D-3V approach is taken where

$$\frac{d}{dt}\begin{bmatrix} r \\ z \\ \dot{r} \\ h \\ \dot{z} \end{bmatrix} = \begin{bmatrix} \dot{r} \\ \dot{z} \\ \frac{F_r}{m} + \frac{h^2}{r^3} \\ \frac{rF_\theta}{m} \\ \frac{F_z}{m} \end{bmatrix}, \tag{5.34}$$

and h is the angular momentum per unit mass, $h = r^2\dot{\theta}$.

The form of the force depends on the species under consideration. Neutral atoms have no charge and are thus unaffected by the applied fields, so the force is zero. For ions of arbitrary charge state Z, the force is given by the Lorentz force law:

$$\mathbf{F} = Ze\left(\mathbf{E} + \mathbf{v} \times \mathbf{B}\right), \tag{5.35}$$

where the electric and magnetic fields are determined by first-order PIC weighting from the mesh onto the macroparticles.[47,48,51,74] If the propellant is xenon, then the ions are largely unmagnetized and the axial and radial components of the $\mathbf{v} \times \mathbf{B}$ term can be neglected. However, because the flow is assumed to be axisymmetric, $E_\theta = 0$ and the θ component of the $\mathbf{v} \times \mathbf{B}$ term cannot be neglected.

5.1.4 Collisions

5.1.4.1 Elastic Collisions

The elastic collisions most relevant to the problem of wall erosion are momentum-exchange and charge-exchange collisions between ions and neutral atoms. These two processes influence the 3D velocity distribution function of the particles striking the walls, and may thus affect the erosion rate. Elastic electron-ion and electron-neutral collisions, in contrast, have no effect on the VDF of the heavy particles because the electrons are so much lighter than the ions, making energy transfer between electrons and ions very inefficient. Thus, elastic collisions between electrons and the heavy particles can be neglected with regard to wall erosion.

Momentum-exchange collisions occur when two particles enter each other's force field and the repulsive forces shift the velocity vectors of the two particles. These events typically involve very little energy transfer between the colliding particles, and the overwhelming majority result in very small scattering angles. Momentum-exchange collisions are of critical importance in a bulk gas or plasma, as they are responsible for pushing the 3D VDF of the bulk gas towards the equilibrium Maxwell-Boltzmann distribution. In a Hall thruster, however, the propellant gas is Maxwellian upon injection into the discharge channel, so the momentum-exchange collisions will not have a significant effect on the 3D VDF of the neutrals or ions.

Charge-exchange collisions occur when a slow-moving neutral atom captures an electron from a fast-moving ion, resulting in a slow ion and a fast neutral. This has the effect of depopulating the high-energy region of the ion VDF while populating the low-energy region. However, the opposite process happens to the neutral VDF, with the high-energy region being populated and the low-energy region being depopulated. From the standpoint of sputtering, an energetic neutral atom is the same as an energetic ion, so the resulting sputter yields and erosion rates are unlikely to be affected significantly as a direct consequence of a charge-exchange collision. These collisions do affect the plasma density and potential profiles, however, so they may have some effect on the VDF of the ions striking the walls, albeit a small one.

5.1.4.2 Inelastic Collisions

Inelastic collisions play a very important role in Hall thruster operation, with electron impact ionization of the neutral propellant atoms being the process that both ignites and sustains the discharge plasma. Although many inelastic processes occur in a Hall thruster plasma, they all obey the same basic equations. As an example, consider the ionization of a neutral propellant atom to the first ionized state. The rate of production of singly-charged ions is given by

$$\dot{n}_{i,+} = n_e n_n \zeta_i, \tag{5.36}$$

where ζ_i is the forward rate coefficient for ionization. In general, the rate coefficient is a function of the energy distribution function (EDF) of each reactant species. However, because the electrons are much less massive than the atoms and ions, they also have a much greater thermal velocity, and the rate coefficient can be reduced to a function of the electron EDF only:

$$\zeta_i = \int_{\mathcal{E}_0}^{\infty} \left(\frac{2\mathcal{E}_e}{m_e} \right)^{1/2} \sigma_i \left(\mathcal{E}_e \right) f_e \left(\mathcal{E}_e \right) d\mathcal{E}_e, \tag{5.37}$$

where $\mathcal{E}_0$ is the activation energy and σ_i is the collision cross-section. If the electrons follow a Maxwell-Boltzmann distribution, then $\zeta_i = \zeta_i \left(T_e \right)$. If the collision cross-sections are known, then Eq. 5.37 can be integrated numerically to determine the rate coefficient.

The inelastic collisions also serve as sink terms in the electron energy equation. The energy loss rate can be computed from the reaction rate as

$$S_i = \mathcal{E}_0 \dot{n}_{i,+} = \mathcal{E}_0 n_e n_n \zeta_i \left(T_e \right). \tag{5.38}$$

This holds for both electron impact ionization and excitation. However, because excitation is not explicitly included in HPHall, an empirical sink term must be added to the electron energy equation to estimate the energy loss rate due to excitation. The details of the empirical term are given in Chapter II of Ref. 51.

5.2 Model Updates

Summarized below are the changes made to HPHall through the course of this work. These changes include updated collision cross-sections for 0 → I and 0 → II ionization of xenon, the addition of triply-charged xenon ions, and additions to the erosion submodel.

5.2.1 Ionization Cross-Sections

In the first version of HPHall, the collision cross-sections for 0 → I and 0 → II ionization reactions for xenon were based on Drawin curve fits[81] to the data of Mathur and Badrinathan.[82] The Drawin form is given by

$$\sigma_i\left(u\right) = 2.66\pi a_0^2 \xi \beta_1 \left(\frac{\mathcal{E}_H}{\mathcal{E}_i}\right)^2 \frac{u-1}{u^2} \ln\left(1.25\beta_2 u\right), \quad u = \frac{\mathcal{E}_e}{\mathcal{E}_i}, \tag{5.39}$$

where a_0 is the Bohr radius, ξ is the number of equivalent electrons in the valence subshell of the target species, $\mathcal{E}_H$ is the ionization potential of the hydrogen atom, and β_1 and β_2 are fitting coefficients. Substituting this and a Maxwellian electron energy distribution function (EEDF) into Eq. 5.37 gives

$$\zeta_i\left(T_e\right) = Q\beta_1\theta^{-3/2}\int_1^\infty \exp\left(-\frac{u}{\theta}\right)\left(\frac{u-1}{u}\right)\ln\left(1.25\beta_2 u\right)du, \quad \theta = \frac{k_B T_e}{\mathcal{E}_i}, \tag{5.40}$$

where Q is a constant given by

$$Q = 10.64 a_0^2 \left(\frac{\pi k_B \mathcal{E}_i}{2 m_e}\right)^{1/2} \left(\frac{\mathcal{E}_H}{\mathcal{E}_i}\right)^2 \xi. \tag{5.41}$$

In a work by Katz *et al.*,[83] the cross-sections for I → II ionization were updated to follow a separate form, so this reaction is not considered here. For single ionization, the ionization potential $\mathcal{E}_i$ is 12.1 eV, and the number ξ of equivalent electrons is 6. This gives $Q^{0\to\mathrm{I}} = 4.12 \times 10^{-12}\,\mathrm{m}^3/\mathrm{s}$. For double ionization, the ionization potential is 33.3 eV, but because two electrons are removed in this reaction, the “number of equivalent electrons” is somewhat ambiguous. Fife recommends[51] $\xi^{0\to\mathrm{II}} = 3$, but as of the start of this work the value of $Q^{0\to\mathrm{II}}$ implemented in HPHall is $1.11\times10^{-13}\,\mathrm{m^3/s}$, which corresponds to $\xi^{0\to\mathrm{II}} = 7.37$. If ξ is interpreted literally as the number of equivalent electrons in the valence subshell regardless of the reaction considered, then $\xi^{0\to\mathrm{II}} = 6$. If $\xi^{0\to\mathrm{II}}$ is interpreted as the number of equivalent electron *pairs*, then it takes a value of 15. However, because of the presence of the best-fit parameter β_1, the value chosen for $\xi^{0\to\mathrm{II}}$ makes no practical difference. Hence, a value of $\xi^{0\to\mathrm{II}} = 6$ is chosen for this work.

Fife proposed values of $\beta_1 = 1.0$ and $\beta_2 = 0.8$ for both the $0 \to \mathrm{I}$ and $0 \to \mathrm{II}$ reactions, and these values have been used up to the start of the present work.[51] However, there are some notable issues with these values.[78] Figure 5.1 shows the original fitted collision cross-sections alongside the experimental measurements of Mathur and Badrinathan,[82] Stephan and Märk,[84] and Wetzel *et al.*[85] For single ionization, the fitted curve underestimates the cross-section relative to the experimental measurements for electron energies above about 70 eV. For double ionization, the fitted curve matches Mathur’s measurements well over the available range of the data, but overestimates the cross-section compared to the other measurements. These data therefore suggest that HPHall underestimates the production rate of singly-charged ions and overestimates the production rate of doubly-charged ions from the $0 \to \mathrm{II}$ reaction.

As a first step towards revising the existing ionization cross-sections, the Drawin curve fits to the experimental data are recomputed. Rather than considering only the data of Mathur and Badrinathan, these curves are fit to all three data sets given in Fig. 5.1. In addition, a new curve fit is introduced that is based on the original Drawin form:

$$\sigma_i\left(u\right) = 2.66\pi a_0^2 \xi \beta_1 \left(\frac{\mathcal{E}_i^H}{\mathcal{E}_i}\right)^2 \frac{u-1}{u^{\beta_3}} \ln\left(1.25\beta_2 u\right), \quad u = \frac{\mathcal{E}_e}{\mathcal{E}_0}, \tag{5.42}$$

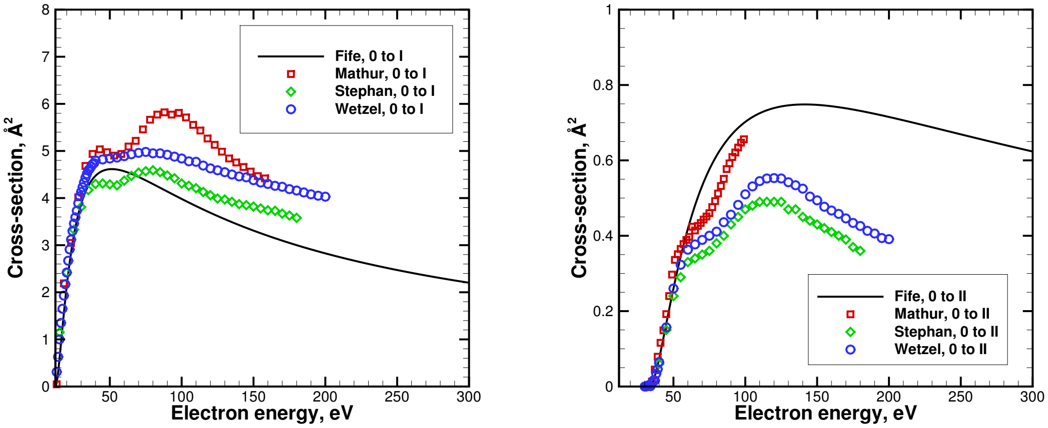

(a) (b)

Figure 5.1: Existing ionization cross-sections in HPHall compared to experimental data for (a) $0 \rightarrow$ I and (b) $0 \rightarrow$ II reactions.

where a third free fit parameter, β_3 is introduced. Equation 5.39 can be recovered by setting $\beta_3 = 2$. The addition of this free parameter is motivated by the behavior of the Drawin curves in Fig. 5.1 with increasing electron energy.[78] For single ionization, the fitted curve appears to decay too quickly with electron energy. If $\beta_3 < 2$, this decay rate will decrease and allow the fit to better match the experimental data. Conversely, the fitted curve for double ionization appears to decay too slowly, and setting $\beta_3 > 2$ will cause the decay rate to increase.

Figure 5.2 shows the recalculated curve fits alongside the experimental measurements, and Table 5.3 shows the resulting fit parameters. Note that these fits are performed in a least-squares sense to all three sets of measurements. Thus, the curves also serve as an average of the three datasets. For both ionization reactions, both the recalculated Drawin fit and revised Drawin fit follow the experimental measurements more closely than the original Drawin fit. Comparing the two curves for each reaction, we see that the differences are rather small except at very high electron energies, where the effects of the additional fit parameter in the revised Drawin form are evident.

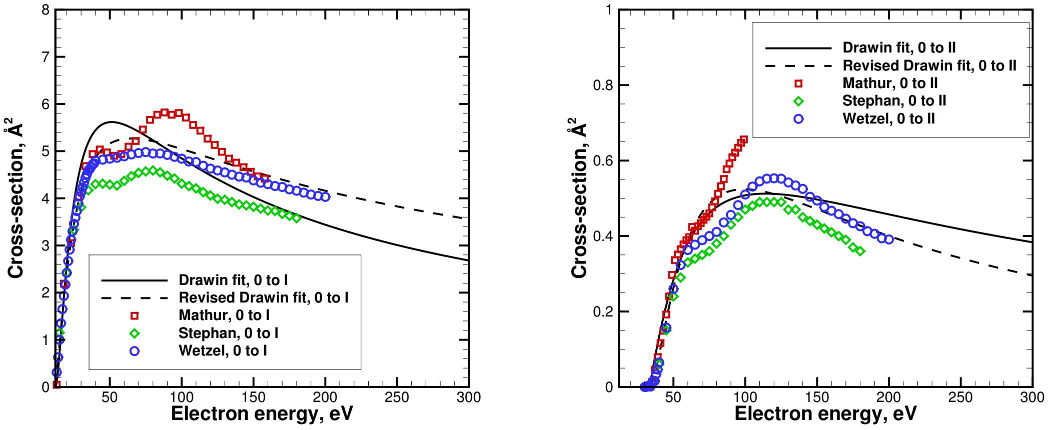

(a) (b)

Figure 5.2: Drawin and revised Drawin fits to experimentally-measured collision cross-sections for (a) 0 → I and (b) 0 → II reactions.

Table 5.3: Drawin and revised Drawin fit coefficients for 0→I and 0→II ionization.

Fit		Q, m^3/s	β_1	β_2	β_3
0→I	Drawin	4.13×10^{-13}	1.22	0.8	-
	Revised	4.13×10^{-13}	0.66	1.04	1.74
0→II	Drawin	9.04×10^{-14}	0.62	1.28	-
	Revised	9.04×10^{-14}	1.42	0.87	2.41

Although the revised Drawin form seems to improve the accuracy of the collision cross-sections, it is the integrated rate coefficients that are actually used to compute ionization rates in HPHall. The integrated rate coefficients are shown in Fig. 5.3. For 0 → I ionization, the updated curve fits result in a rate coefficient that is generally greater than that resulting from Fife's original fit. At an electron temperature of 20 eV the rate coefficient is 14% greater for the revised Drawin form, and at 30 eV it is 17% greater. Conversely, for 0 → II ionization, the updated fits generally result in a lower rate coefficient, with differences of 13% and 20% at electron temperatures of 20 eV and 30 eV, respectively. However, at an electron temperature of 5 eV, the updated rate coefficient for 0 → II ionization is 8% greater than the existing rate

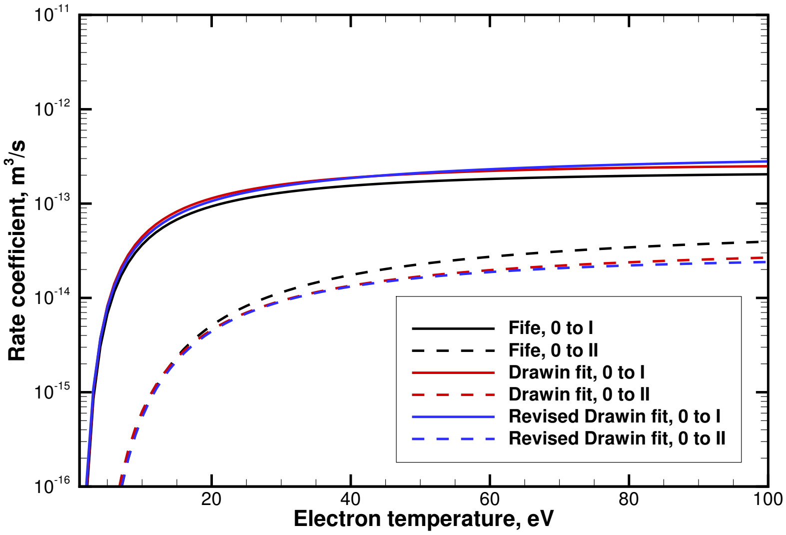

Figure 5.3: Integrated rate coefficients for 0 → I and 0 → II ionization reactions.

coefficient. Hence, an increased rate of double ionization should be expected in low-temperature regions such as the plume, but because the rate of ionization in those regions is already very small, this increase should have no effect on the predicted thruster performance or wall erosion rates.

One thing worthy of noting in Fig. 5.3 is that the two updated curve fits result in very similar rate coefficients for both reactions considered. This is to be expected because the differences in the collision cross-sections are quite small, and the convolution involved in Eq. 5.37 muddles those differences further. The differences are most pronounced at high electron temperatures, where the revised Drawin cross-sections better match the trends in the experimental data. For the purposes of this work, the revised Drawin cross-sections are used for both 0 → I and 0 → II ionization of xenon and are implemented within HPHall.

The differences between HPHall's original rate coefficients and those computed using the revised Drawin fit are only on the order of 10%, but it is expected that they will have a noticeable impact on the Hall thruster simulations. Particularly, since the rate coefficient for single ionization has increased and that for double ionization has decreased, the thruster efficiency predicted by the simulations should increase compared to simulations using the old cross-sections. This is because the momentum carried by an ion of charge state Z is proportional to $Z^{1/2}$, whereas the current carried by the same ion is proportional to $Z^{3/2}$. Hence, increasing the rate of 0→I ionization while decreasing the rate of 0→II ionization should increase the ratio F_{th}^2/I_d, thus increasing the anode efficiency for a given operating point.

5.2.2 Triply-Charged Xenon

Past versions of HPHall have included only singly- and doubly-charged xenon ions. Although triply-charged ions make up no more than a few percent of the total ion current in typical Hall thrusters, the presence of triple ions and even higher-order species becomes more important as discharge voltage and electron temperature increase. There is also evidence to suggest that such high charge states are prevalent in magnetically-shielded Hall thrusters.[86] Hence, the addition of these higher charge states, namely Xe^{3+}, may be valuable for modeling high-voltage and magnetically-shielded Hall thrusters. The three ionization reactions that can result in Xe^{3+} are:

$$\mathrm{e}^- + \mathrm{Xe} \rightarrow 4\mathrm{e}^- + \mathrm{Xe}^{3+}, \tag{5.43}$$

$$\mathrm{e}^- + \mathrm{Xe}^+ \rightarrow 3\mathrm{e}^- + \mathrm{Xe}^{3+}, \tag{5.44}$$

$$\mathrm{e}^- + \mathrm{Xe}^{2+} \rightarrow 2\mathrm{e}^- + \mathrm{Xe}^{3+}. \tag{5.45}$$

These three reactions are now included in HPHall. The cross-sections for the 0 → III ionization reaction come from the data of Mathur and Badrinathan,[82] Stephan and Märk,[84], and Wetzel *et al.*[85] The cross-sections for the I → III and II → III reactions come from the data of Achenbach *et al.*[87,88] All data are fitted using the revised Drawin form given in Eq. 5.42. The cross-sections and the integrated rate coefficients for each reaction are shown in Fig. 5.4, and the fit coefficients for the revised Drawin

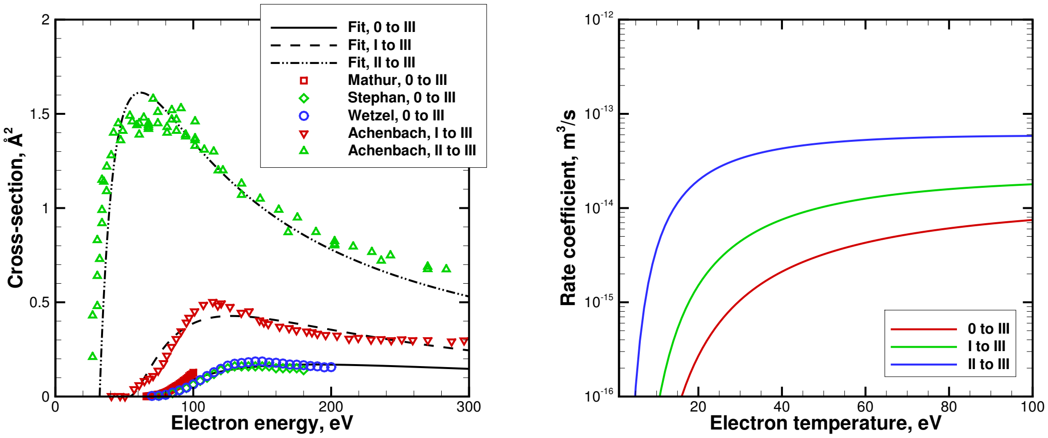

(a) (b)

Figure 5.4: Fitted cross-sections (a) and integrated rate coefficients (b) for 0 → III, I → III, and II → III ionization reactions.

Table 5.4: Revised Drawin fit coefficients for 0 → III, I → III, and II → III ionization reactions.

Fit	$\mathcal{E}_0$, eV	ξ	Q, m^3/s	β_1	β_2	β_3
0→III	65.4	6	3.28×10^{-14}	1.94	0.8	2.48
I→III	53.3	5	3.72×10^{-14}	5.57	0.8	2.85
II→III	32.1	4	6.37×10^{-14}	0.56	1096.5	2.21

curve fits are given in Table 5.4.

As one might expect, the reaction with the greatest activation energy (0 → III) has the smallest collision cross-section, whereas the reaction with the lowest activation energy (II → III) has the largest cross-section. This trend translates directly into the rate coefficients, where there is between one and two orders of magnitude difference between the 0 → III and II → III reactions. However, since $n_n \sim 10n_{i,+}$ and $n_{i,+} \sim 10n_{i,2+}$ in Hall thrusters, each of these reactions may make similar contributions to the population of triply-charged ions.

5.2.3 Erosion Submodel

Two major updates to the erosion submodel are required in order to model the transport of the erosion products. The first is the addition of dynamic sputter yield calculations, wherein the sputter yield is calculated for each ion macroparticle that strikes the walls as the simulation runs. The second is the addition of a new species and the generation of new macroparticles based on the sputter yield calculations. As demonstrated in Chapter IV, *h*-BN sputters primarily as B and N_2. Of those two species, only atomic boron is easily condensible, so it is atomic boron that is included in the updated erosion model.

5.2.3.1 Dynamic Sputter Yield Calculation

To compute the sputter yield—and thus the erosion rate—when an ion strikes the discharge channel wall, one must know the incidence angle and kinetic energy of the impacting ion. The incidence angle is calculated based on the ion's velocity vector at the sheath edge, the floating sheath potential, and the wall normal. If $\mathbf{v}_1$ is the velocity vector at the sheath edge and $\mathbf{v}_2$ is the velocity vector at the wall:

$$\begin{aligned}
\mathbf{v}_1 &= v_z\hat{\mathbf{z}} + v_r\hat{\mathbf{r}} + v_\theta\hat{\theta} \\
\mathbf{v}_2 &= (v_z + \Delta v_z)\,\hat{\mathbf{z}} + (v_r + \Delta v_r)\,\hat{\mathbf{r}} + v_\theta\hat{\theta}
\end{aligned}$$

where the geometry is assumed to be axisymmetric and the electric field in the sheath is assumed to act normal to the wall. We need to solve for both Δv_z and Δv_r in order to obtain the ion incidence angle. From energy conservation:

$$|\mathbf{v}_2|^2 - |\mathbf{v}_1|^2 = \frac{2q\phi_s}{m_i} \tag{5.46}$$

where the sheath potential ϕ_s is known from the Hobbs and Wesson sheath model.

One can define a spatial coordinate n that points in the direction of the inward-facing wall normal vector $\hat{\mathbf{n}}$. Momentum conservation then gives

$$\begin{aligned} -q\nabla\phi &= m\frac{d\mathbf{v}}{dt}, \\ -q\frac{d\phi}{dn}\hat{\mathbf{n}} &= m\frac{d\mathbf{v}}{dt}, \\ -q\frac{d\phi}{dn}\left(n_z\hat{\mathbf{z}} + n_r\hat{\mathbf{r}}\right) &= m\frac{d}{dt}\left(v_z\hat{\mathbf{z}} + v_r\hat{\mathbf{r}} + v_\theta\hat{\theta}\right). \end{aligned} \tag{5.47}$$

Manipulating the $\hat{\mathbf{z}}$ and $\hat{\mathbf{r}}$ components of Eq. 5.47 and combining them gives

$$\begin{aligned} n_r\frac{dv_z}{dt} &= n_z\frac{dv_r}{dt}, \\ n_r\Delta v_z &= n_z\Delta v_r. \end{aligned} \tag{5.48}$$

Substituting from Eq. 5.48 into Eq. 5.46 then gives a quadratic equation for either Δv_z or Δv_r. Solving for Δv_z gives:

$$\Delta v_z = \frac{-\left(v_z + \frac{v_r n_r}{n_z}\right) \pm \sqrt{\left(v_z + \frac{v_r n_r}{n_z}\right)^2 + \left(1 + \frac{n_r^2}{n_z^2}\right)\left(\frac{2q\phi_s}{m}\right)}}{1 + \frac{n_r^2}{n_z^2}}. \tag{5.49}$$

The term inside the square root is always positive. For $v_z < 0$ we take the negative root. For $v_z > 0$ we take the positive root. Δv_r is then found by substituting Δv_z into Eq. 5.48. In the limiting case of $n_z = 0$:

$$\begin{aligned} \Delta v_z &= 0, \\ \Delta v_r &= -v_r \pm \sqrt{v_r^2 + \frac{2q\phi_s}{m}}. \end{aligned} \tag{5.50}$$

Now $\mathbf{v}_2$ is known, so the incidence angle relative to the wall normal is simply

$$\theta_i = \cos^{-1}\left(\frac{\mathbf{v}_2 \cdot \hat{\mathbf{n}}}{|\mathbf{v}_2|}\right). \tag{5.51}$$

and the ion kinetic energy is

$$\mathcal{E}_i = \frac{1}{2} m_i \left| \mathbf{v}_2 \right|^2 . \tag{5.52}$$

With the kinetic energy and incidence angle of the ion known, one can compute the sputter yield. First, the sputter yield at normal ion incidence is calculated according to a Bohdansky curve fit to the MD data, as given by Eq. 4.2.[22,69,89] Then, the angular dependence of the sputter yield is calculated from a Yamamura curve fit to the MD data at 100 eV ion energy, as given by Eq. 4.4.[27,69,89] The sputter yield Y is then

$$Y\left(\mathcal{E}_i, \theta_i\right) = Y_B\left(\mathcal{E}_i\right) \hat{Y}_Y\left(\theta_i\right) . \tag{5.53}$$

Finally, if the numerical weight of the ion macroparticle is W_{ion}, then the instantaneous wall erosion rate (in units of atoms per second *per unit azimuthal length*) can be calculated as

$$\dot{N}_e = \frac{W_{ion} Y}{\Delta t} . \tag{5.54}$$

This quantity is mapped to the mesh using first-order PIC weighting, and the time-averaged value is recorded to a text file at the end of each simulation.

5.2.3.2 Boron Macroparticle Generation

Each time an ion macroparticle strikes the discharge channel wall, the sputter yield is computed according to Eq. 5.53. Boron macroparticles must then be generated such that the number of real boron atoms introduced matches the calculated sputter yield. If N_B boron macroparticles are produced each time an ion strikes the wall, then the numerical weight of each boron macroparticle is given by

$$W_B = \frac{W_{ion}}{N_B} \frac{Y}{2} , \tag{5.55}$$

where the factor of 2 is introduced because boron makes up only half of the sputtered atoms. For cases when the calculated yield Y is very small, W_B may be less than 1. This is nonphysical, so a minimum allowable sputter yield is set such that a minimum macroparticle weight of 100 is maintained. When the calculated yield is less than the minimum, a random number between 0 and 1 is generated and compared to the value

$$\frac{Y_{min} - Y}{Y_{min}}. \tag{5.56}$$

If the random number is less than this value, boron macroparticles are generated according to Eq. 5.55 with $Y = Y_{min}$. Otherwise, no boron macroparticles are generated.

The directions of forward and transverse sputtering in cylindrical polar coordinates must be known in order to assign the correct velocity vector to the ejected boron atoms. These are computed from the known surface normal vector and the incident ion's velocity vector, $\mathbf{v}_2$, as defined in the previous section. Given that the inward-pointing surface normal vector $\hat{\mathbf{n}}$ is known, the unit vector $\hat{\mathbf{p}}$ defining the forward sputtering direction is computed as

$$\hat{\mathbf{p}} = \frac{\sqrt{\left(v_z + \Delta v_z\right)^2 (1 - n_z^2)}\hat{\mathbf{z}} + \sqrt{\left(v_r + \Delta v_r\right)^2 (1 - n_r^2)}\hat{\mathbf{r}} + v_\theta \hat{\theta}}{|\mathbf{v}_2| \sin\left(\theta\right)}, \tag{5.57}$$

where $n_z = \hat{\mathbf{n}} \cdot \hat{\mathbf{z}}$ and $n_r = \hat{\mathbf{n}} \cdot \hat{\mathbf{r}}$. The unit vector defining the transverse sputtering direction is then

$$\begin{aligned} \hat{\mathbf{t}} &= \hat{\mathbf{p}} \times \hat{\mathbf{n}}, \\ \hat{\mathbf{t}} &= -p_\theta n_r \hat{\mathbf{z}} + p_\theta n_z \hat{\mathbf{r}} + \left(p_z n_r - p_r n_z\right) \hat{\theta}. \end{aligned} \tag{5.58}$$

Now, noting that $\hat{\mathbf{n}}$ points into the wall, we can define the velocity vector of an ejected boron atom as

$$\begin{aligned}
\mathbf{v}_B &= -v_n\hat{\mathbf{n}} + v_p\hat{\mathbf{p}} + v_t\hat{\mathbf{t}}, \\
\mathbf{v}_B &= \left(-v_n n_z + v_p p_z - v_t p_\theta n_r\right)\hat{\mathbf{z}} \\
&\quad + \left(-v_n n_r + v_p p_r + p_\theta n_z\right)\hat{\mathbf{r}} \\
&\quad + \left(v_p p_\theta + v_t\left(p_z n_r - p_r n_z\right)\right)\hat{\theta}.
\end{aligned} \tag{5.59}$$

The velocity components v_n, v_p, and v_t are determined by sampling from velocity distribution functions (VDFs) calculated from the MD data. The forward and transverse velocity components, v_p and v_t, are sampled from Maxwell-Boltzmann distributions. Along the surface normal direction, a flux-biased Sigmund-Thompson velocity distribution is used:[19,21,89]

$$f_{ST}\left(v_n\right) \propto \frac{v_n^3}{\left(v_n^2 + v_b^2\right)^{3-2m}}. \tag{5.60}$$

The effective binding velocity v_b is related to the surface binding energy as

$$U_b = \frac{1}{2} m_B v_b^2. \tag{5.61}$$

The VDF parameters are determined from the MD simulation results. As demonstrated in Chapter IV, these parameters may depend on the kinetic energy and incidence angle of the impacting ions. For ion energies above 100 eV, however, the surface binding energy U_b becomes approximately constant with increasing ion energy, and averages to about 4.5 eV. The factor m appears to be independent of the properties of the incident ion, and is approximately zero for all MD simulation cases. On the other hand, the Maxwellian mean velocity and temperature vary much more widely between cases than the Sigmund-Thompson parameters. For normal ion incidence, the mean velocity is zero, but for oblique incidence, the mean velocity in the forward sputtering direction can be as high as 7000 m/s. For the purposes of this work, a mean velocity of zero is assumed for both the forward and transverse sputtering di-

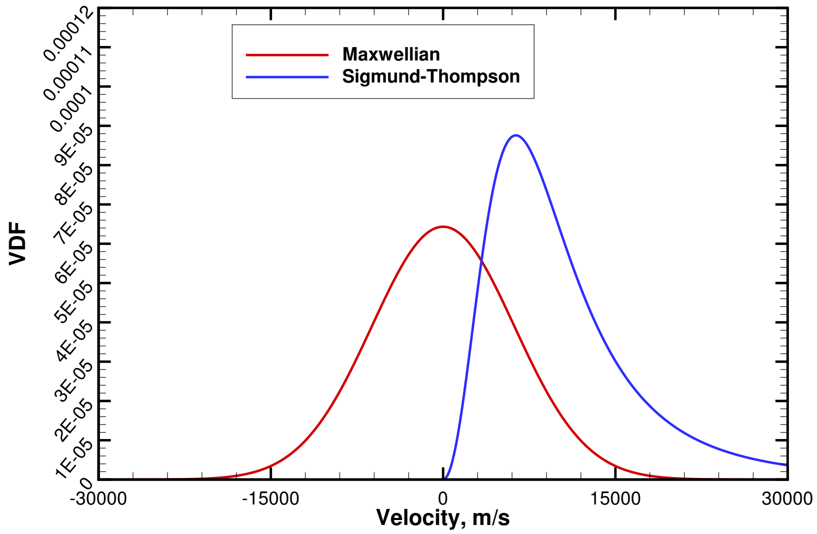

Figure 5.5: Maxwellian and Sigmund-Thompson VDFs of atomic boron used in the hybrid-PIC model.

rections. Likewise, the temperature is a strong function of the ion properties, ranging from 10,000 K up to over 100,000 K. In this work, an intermediate value of 50,000 K is chosen, which is roughly consistent with the case of 100 eV ions at normal incidence. The Sigmund-Thompson and Maxwellian distributions used in this work are shown in Fig. 5.5.

Once boron macroparticles are introduced at the channel walls, they are allowed to stream freely through the simulation domain. The effects of scattering collisions are neglected, so each macroparticle moves in a straight line from its point of origin until it exits the domain or strikes a surface. Any boron particles that strike a surface are assumed to condense and are thus removed from the system. The instantaneous redeposition rate associated with a condensing boron macroparticle is given by

$$\dot{N}_r = \frac{W_B}{\Delta t}. \tag{5.62}$$

As the boron atoms stream through the bulk plasma, it is possible for them to

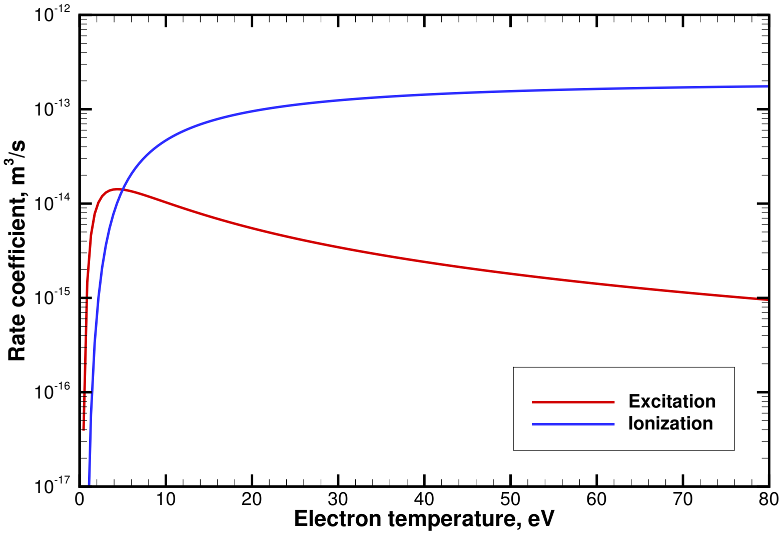

Figure 5.6: Rate coefficients for ionization and excitation of boron included in HPHall.

undergo electron impact ionization or excitation. A previous effort by Dragnea *et al.* using a direct simulation Monte Carlo (DSMC) technique showed a large disparity between the simulation results and cavity ring-down spectroscopy (CRDS) measurements in the SPT-70 Hall thruster.[45] Since the CRDS setup could only detect neutral, ground-state boron, it was hypothesized that excitation and ionization of boron may account for the differences between the simulations and experiment. Thus, single ionization of boron and excitation of ground-state neutral boron to the ^{4}P metastable state are included in the present work. The ^{4}P state is chosen because of its long life compared to other excited states[90] and because the collision cross-sections for excitation from the ground state are quite large. The collision cross-sections for ionization come from the calculations of Kim and Stone[91], whereas the cross-sections for excitation come from the calculations of Ballance *et al.*[92] These cross-sections are integrated numerically using a trapezoidal method and assuming a Maxwellian EEDF for inclusion as rate coefficients in HPHall. The rate coefficients are plotted in Fig. 5.6.

Note that while both ionization and excitation of boron are included, only excited boron atoms are tracked in the simulations. Boron ions are assumed to rapidly accelerate out of the thruster once they are created due to their very light weight compared to xenon. Hence, boron ionization serves only as a sink-term for ground-state boron in these simulations.

5.3 Simulation Setup

The thruster modeled in this work is NASA's 3.8 kW High-Voltage Hall Accelerator (HiVHAc).[93–96] The HiVHAc thruster development project is being conducted jointly by NASA Glenn Research Center (GRC) and Aerojet Rocketdyne. The present engineering development unit (EDU2) has demonstrated operation at discharge voltages of up to 650 V and discharge powers in excess of 4 kW. It is a highly throttleable device, with high-voltage modes achieving an I_{sp} approaching 2700 s and low-voltage modes achieving thrust-to-power ratios competitive with other state-of-the-art Hall thrusters.

The HPHall simulation mesh consists of 70×30 cells. The magnetic field topology is generated from a commercial magnetic field solver and is validated against experimental measurements. The base time step for each simulation is 5×10^{-8} s. The electron time step is $^{1}/_{1250}$ the base time step. The background gas pressure, corrected for xenon, is included in all presented simulation cases. A minimum of approximately 180,000 ion macroparticles and 130,000 neutral macroparticles were used in each simulation.

Simulations are performed by first populating the domain with neutrals for 20,000 time steps. Then, the simulation is run with the plasma species turned on for 5000–10,000 time steps to allow startup transients to stabilize. The simulation is then run for 40,000 time steps to collect performance data. The location of the cathode magnetic field line is determined by progressively moving its location downstream over a series of simulations until the calculated thrust becomes constant.

For each simulation case, the values of α from Eq. 5.23 are determined by first setting the value in each region to some baseline values established for the H6 Hall thruster.[76] Then, the location of each region is adjusted such that the calculated discharge current roughly matches the measured discharge current. Then, the Bohm coefficient in the plume, α_p, is fixed at 10, and the values of α_c and α_e are adjusted to more finely match the measured discharge current. If necessary, further iterations between adjusting the location of the discharge regions and adjusting the values of the Bohm coefficients are performed.

For boron transport simulations, the above steps for establishing a converged plasma simulation are performed. Then, the boron component of the erosion submodel is activated, and 20,000 additional time steps are simulated. The time-averaged 2D data from simulations are saved and then processed for further analysis and comparison to experimental data where available.

CHAPTER VI

Hall Thruster Simulation Results and Assessment

In this chapter, we discuss the results of the Hall thruster plasma simulations. First, the baseline simulations of NASA's HiVHAc thruster are presented. These simulations cover three operating points: 300 V, 400 V, and 500 V discharge voltage, at approximately 10 A, 8 A, and 7 A discharge current, respectively. The predicted thruster performance is compared to the measured performance at each operating point, and the plasma properties are briefly discussed. Then, the effects of the revised collision cross-sections for single and double ionization of neutral xenon are assessed for the baseline operating conditions by comparing the predicted performance and plasma properties to the results of the baseline simulations. Next, the influence of triply-charged xenon is analyzed via comparison to the data utilizing the revised cross-sections for single and double ionization. Finally, the results of boron transport simulations at operating points of 500 V discharge voltage at approximately 2 A, 4 A, and 6 A discharge current are presented. The effects of ionization and electronic excitation of boron on the density of neutral, ground-state boron are assessed. The plasma properties along the channel walls are compared to measurements obtained using wall-mounted Langmuir probes at the 500 V, 4 A operating condition,[97] and the ground-state boron density is compared to measurements obtained using cavity ring-down spectroscopy.[98]

6.1 Ionization Updates

6.1.1 Baseline Operating Conditions

The effects of the ionization updates described in Chapter V are assessed by simulating the HiVHAc at the three operating points given in Table 6.1.[99] All measurements were performed in Vacuum Facility 5 (VF-5) at NASA Glenn Research Center (GRC) in April to May of 2013. VF-5 is an 18.3 m long, 4.6 m diameter cylindrical vacuum chamber capable of sustaining a no-load background pressure of 1×10^{-7} Torr. The test diagnostics for these experiments included an inverted pendulum thrust stand and a Faraday probe that was swept downstream of the thruster to measure the ion beam current. The thrust-derived anode efficiency η_a is calculated as

$$\eta_a = \frac{F_{th}^2}{2\dot{m}_a V_d I_d}, \tag{6.1}$$

and the current utilization efficiency η_I is defined as

$$\eta_I = \frac{I_b}{I_d}. \tag{6.2}$$

6.1.2 Baseline Simulations

6.1.2.1 Thruster Performance

Shown in Table 6.2 are the calculated performance parameters for the baseline simulations of HiVHAc, i.e., before any updates were made to the model. The values of the Bohm coefficients are also given. Compared to the experimental measurements, the HPHall simulations consistently underestimate the thrust of the HiVHAc thruster by a few percent. Given that the simulation parameters are adjusted to match the discharge current, this also means that the simulations underestimate the anode efficiency. The calculated ion current matches the measured ion within a few percent at the 400 V and 500 V points, but overestimates the beam current at the

Table 6.1: HiVHAc EDU2 measured performance parameters for the baseline simulation cases.

V_d, V	$\dot{m}_a$, mg/s	I_d, A	I_b, A	F_{th}, mN	η_a	η_I	p_c, Torr
300.3	10.21	9.96	7.38	186	56.6%	74.1%	2.7×10^{-6}
400.8	8.29	8.00	6.40	173	56.3%	80.0%	2.2×10^{-6}
500.0	7.13	6.97	5.58	169	57.5%	80.1%	1.7×10^{-6}

Table 6.2: HiVHAc EDU2 baseline performance predicted by HPHall.

V_d, V	α_c	α_e	α_p	I_d, A	I_b, A	I_b^{2+}, A	F_{th}, mN	η_a	η_I
300.3	0.18	0.02	10.0	9.83	7.79	1.31	178	52.8%	79.2%
400.8	0.2	0.018	10.0	7.94	6.32	1.12	167	53.0%	79.6%
500.0	0.09	0.02	10.0	6.92	5.47	1.05	161	52.7%	79.1%

Table 6.3: HiVHAc EDU2 performance predicted by HPHall with revised cross-sections for 0 → I and 0 → II ionization.

V_d, V	I_d, A	I_b, A	I_b^{2+}, A	F_{th}, mN	η_a	η_I
300.3	9.81	7.82	1.24	181	54.5%	79.7%
400.8	8.00	6.35	1.05	171	54.4%	79.3%
500.0	7.02	5.50	0.99	165	54.3%	78.4%

Table 6.4: HiVHAc EDU2 performance predicted by HPHall with triply-charged xenon included.

V_d, V	I_d, A	I_b, A	I_b^{2+}, A	I_b^{3+}, A	F_{th}, mN	η_a	η_I
300.3	9.84	7.86	1.21	0.07	182	54.8%	80.0%
400.8	8.08	6.42	1.03	0.07	171	54.7%	79.5%
500.0	7.07	5.56	0.96	0.09	166	54.5%	78.7%

300 V point. Comparing the current utilization efficiency at each point, we see that the 400 V and 500 V points are consistent with the measurements, but the model overestimates the current utilization efficiency at 300 V. Given that the total anode efficiency is underestimated, this means that at the 300 V operating point, a decrease in some other partial efficiency outweighs the increase in current utilization in the simulation. Looking at the fraction of the current carried by doubly-charged ions, we see that it increases as the discharge voltage increases. This is expected because the electron temperature tends to increase with discharge voltage, causing the production rate of doubly-charged ions to increase.

Note that the values of the three Bohm coefficients are not consistent between simulations. The determined values for the 300 V and 400 V operating points are very similar, but at 500 V the value of α_c is about half the value for the other two operating points. It is not clear whether this is an issue, as the Bohm coefficients are simply empirical parameters that are meant to capture the anomalous electron mobility. However, it is worth noting simply because the anomalous mobility has a significant effect on the resulting plasma properties.

6.1.2.2 Plasma Properties

Figure 6.1 shows the plasma potential normalized by the discharge voltage and the electron temperature along the channel centerline for the three baseline simulations. The axial position z is normalized by the channel length L, with ${}^{z}/_{L} = -1$ corresponding to the anode location and ${}^{z}/_{L} = 0$ corresponding to the channel exit plane. The normalized potential profile is very similar between the three operating points, although the 500 V condition does show a more gradual decrease in the potential upstream of the primary acceleration region. This is likely a consequence of the aforementioned difference in the Bohm mobility coefficient in the near-anode region of the channel. For all operating points, there is a small, nearly constant gradient in

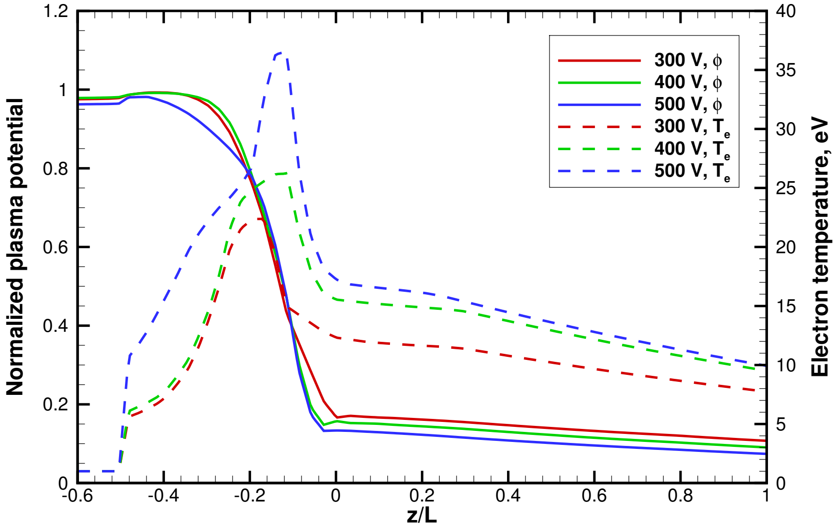

Figure 6.1: Plasma potential normalized by discharge voltage and electron temperature along the channel centerline for the baseline simulations of HiVHAc.

the plasma potential in the plume. Although this is not observed in real thrusters, it is a common characteristic of the results from HPHall simulations.[76] Eliminating this gradient would likely require extensive modification of the electron transport model in HPHall, and hence falls outside the scope of this work.

Looking at the electron temperature, we see the expected increase in the peak value with increasing discharge voltage. Furthermore, the location of the peak electron temperature appears to move downstream with increasing discharge voltage. The magnetic field topology is the same for all three of these operating points, albeit with different magnitudes, so the change in the location of the peak electron temperature is most likely a result of the change in the discharge voltage and in the Bohm mobility parameters.

Figure 6.2 shows 2D contours of plasma potential, electron temperature, and electron density for the baseline case of 400 V discharge voltage and 8 A discharge current. Although there are some differences in the 2D contours for the 300 V and 500 V operating conditions, they are difficult to see, and the general behavior of the plasma potential and electron temperature is consistent between operating points. Thus, the contours in Fig. 6.2 are considered representative of all the baseline cases, at least for the purpose of identifying important regions in the thruster. These contours show that the acceleration zone, where the electric field and electron temperature are greatest, lies just upstream of the channel exit. It is in this region that the wall erosion rates are expected to be greatest. Hence, in the boron transport simulations, the largest concentration of boron should be located near the walls just upstream of the channel exit plane.

6.1.3 Revised Ionization Cross-Sections

6.1.3.1 Thruster Performance

Table 6.3 shows the predicted performance parameters for HiVHAc after updating the collision cross-sections for 0 → I and 0 → II ionization to the revised Drawin form described in Eq. 5.42. No other changes were made to the simulation parameters. Compared to the baseline simulations, the thrust and anode efficiency increase for all three operating conditions. This is consistent with the predictions made in Sect. 5.2.1. The ion beam current is about the same as that predicted by the baseline simulations, but the current carried by doubly-charged ions decreases by about 5–6% for all operating points. This suggests that more current is being carried by the singly-charged ions, again consistent with the predictions made in Sect. 5.2.1. Overall, the results of the updated ionization cross-sections fall entirely within expectations, and show improved agreement with the experimental measurements.

6.1.3.2 Plasma Properties

Figure 6.3 shows the plasma potential and electron temperature along the channel centerline for the baseline operating conditions using both the original and the revised cross-sections for 0 → I and 0 → II ionization of xenon. The plasma potential

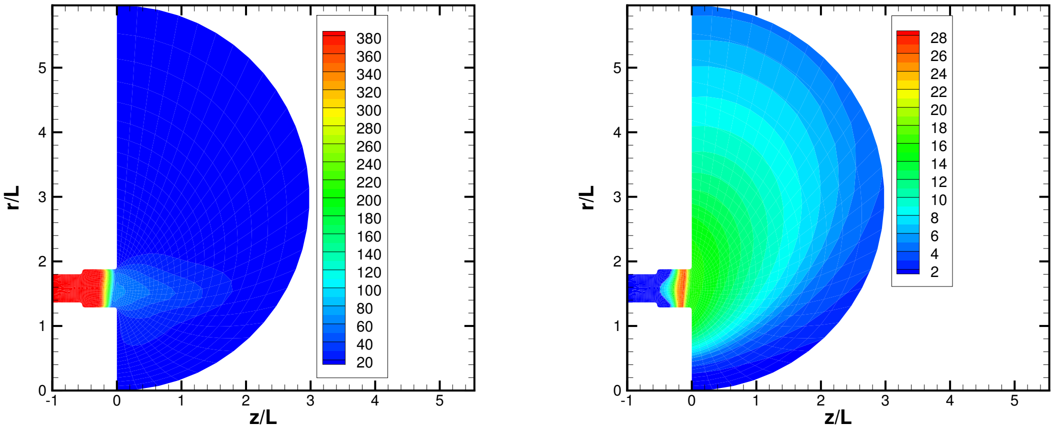

(a) Plasma potential, V

(b) Electron temperature, eV

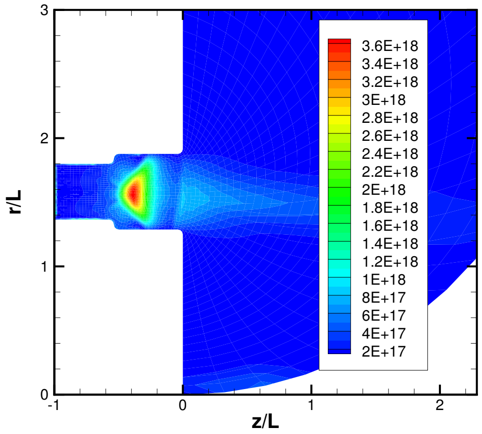

(c) Electron density, m^{-3}

Figure 6.2: 2D contours of plasma potential, electron temperature, and electron density for the baseline case of 400 V, 8 A.

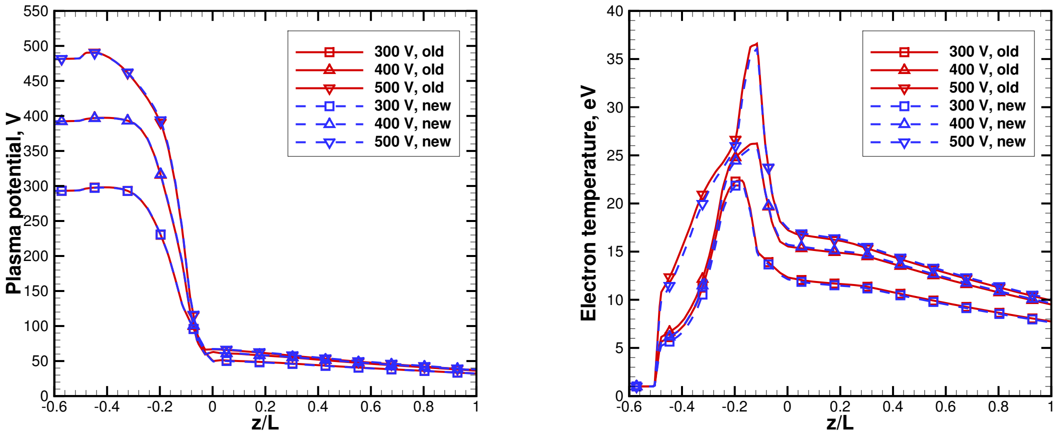

(a) Plasma potential

(b) Electron temperature

Figure 6.3: Plasma potential and electron temperature along the HiVHAc channel centerline using the original and revised cross-sections for ionization.

influences the 3D VDF of the ions striking the channel walls and the location of the erosion band, and is thus extremely important in regards to erosion modeling. Likewise, the electron temperature strongly affects the wall sheath potential, and, thus, is also very important to erosion modeling.

The potential profiles shown in Fig. 6.3 suggest that the changes made to the cross-sections have no noticeable effect on the plasma potential profile. Conversely, the electron temperature profiles show that the electron temperature inside the discharge channel decreases slightly for each operating point, suggesting a decrease in the local sheath potential. The changes in temperature are small, but it is still possible that the effects on the wall erosion rates are non-negligible. Given that the revised cross-sections more accurately reproduce the cross-sections measured experimentally, it is likely that the calculated erosion rates will be more accurate, if they change significantly at all.

6.1.4 Triply-Charged Xenon

6.1.4.1 Thruster Performance

The predicted performance of HiVHAc is shown in Table 6.4 for the baseline operating conditions when triply-charged xenon is included. The thrust increases slightly at 400 V and 500 V due to the additional momentum carried by the triply-charged ions. The discharge current and ion current also tend to increase. This is a consequence of the $Z^{3/2}$ dependence of the current carried by an individual particle. Indeed, at 400 V and 500 V in particular, the increase in ion current seems to correspond very well to the current carried by triple ions. There is a slight reduction in the current carried by double ions at all operating points, most likely as a consequence of II → III reactions. The fraction of current carried by triple ions tends to increase with discharge voltage, which is expected given that electron temperature also tends to increase with discharge voltage. However, the anode efficiency increases slightly at 400 V and 500 V operation, which is unexpected given the arguments outlined in Section 5.2.1. However, since anode efficiency is a derived quantity and is extremely sensitive to other performance parameters, this change is not considered to be significant.

6.1.4.2 Plasma Properties

Based on the rate coefficients alone, one would expect triply-charged ions to have very little effect on the plasma properties under the conditions typical of Hall thrusters. Figure 6.4 shows that this is indeed the case: The addition of triple ions has virtually no effect on the plasma potential or the electron temperature along the channel centerline. This holds true even at the 500 V operating point, where the electron temperature is greater in general and triply-charged ions are expected to have the greatest influence.

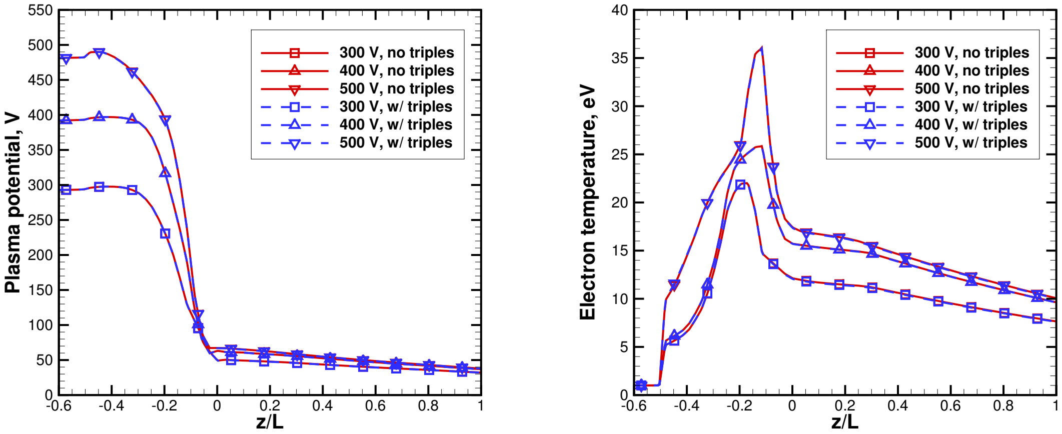

(a) Plasma potential

(b) Electron temperature

Figure 6.4: Plasma potential and electron temperature along the HiVHAc channel centerline without and with triply-charged ions.

Figure 6.5 shows 2D contours of the density of singly- and triply-charged ions for the 500 V operating point. The density of triple ions is at least two orders of magnitude smaller than the density of single ions throughout the simulation domain. This supports the previous observation that triply-charged ions have very little effect on the plasma properties. Note, however, that the triple ion density is strangely high near the walls, particularly in the region upstream of the acceleration zone where the overall ion density should be relatively small. This is believed to be associated with numerical instabilities relating to ionization. Due to the small rate coefficients for the reactions that produce triple ions, the simulations can become unstable if there are insufficiently many reactant macroparticles in any given PIC cell. The II → III ionization reaction is especially difficult to accommodate, as the number of Xe^{2+} macroparticles is generally much smaller than the number of Xe and Xe^{+} macroparticles. In order to achieve simulation stability, the number of macroparticles is increased for simulations that include triple ions, with about 860,000 total ion macroparticles used for the 500 V case. Of these 860,000 ion macroparticles, approx-

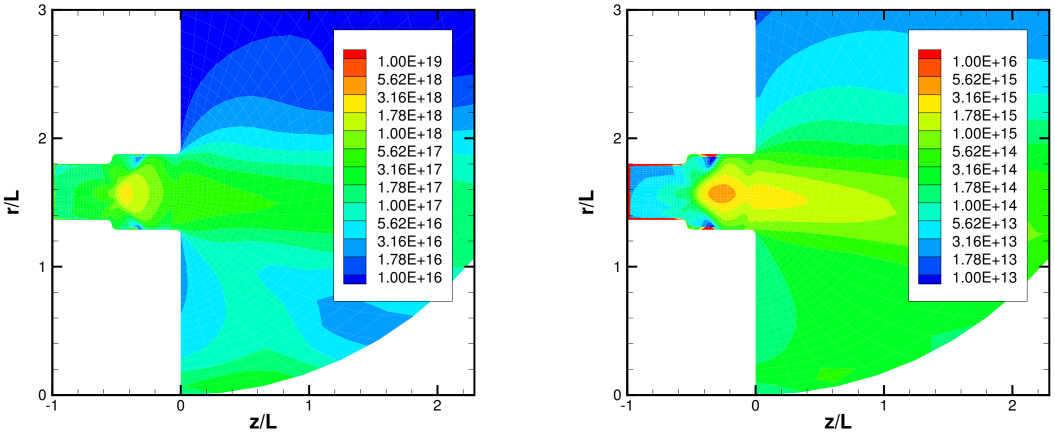

(a) Single ion density, m^{-3} (b) Triple ion density, m^{-3}

Figure 6.5: Number density of singly- and triply-charged ions in HiVHAc operating at 500 V, 6 A.

imately 290,000 are doubly-charged ions and about 220,000 are triply-charged ions. However, it appears that local instabilities still exist in these simulations, indicating that even more macroparticles are required to achieve complete system stability. Given the increased computational cost associated with additional macroparticles, and given that the triple ions have a negligible impact on the properties of the bulk plasma, determining the optimum macroparticle count for inclusion of triple ions is a task left for future work, and all boron transport simulations are performed without triply-charged xenon.

6.2 Boron Transport Simulations

The HiVHAc operating conditions chosen for the boron transport simulations are selected from the operating points studied by Lee *et al.* using cavity ring-down spectroscopy (CRDS).[98] CRDS is a type of absorption spectroscopy in which a laser is fired into a cavity bounded by two high-reflectivity mirrors. The laser frequency is set to match one of the spectroscopic lines of a target species. As the laser is reflected

Table 6.5: Discharge voltage, propellant mass flow rate, and discharge current for the operating points studied in the boron transport simulations.

V_d, V	$\dot{m}_a$, mg/s	I_d, A Exp.	I_d, A Sim.
500.5	2.36	1.99	2.00
500.1	4.26	3.94	4.02
500.6	6.04	6.04	6.08

back and forth in the cavity, some of the target particles absorb photons to undergo electronic excitation, causing the intensity of the light in the cavity to decay. By monitoring the decay rate, the density of the target species integrated along the laser path can be determined. In Lee's experiment, the target species was ground-state, atomic boron, and the measurement location was 6 mm downstream of the channel exit. These conditions fall well within the capabilities of HPHall.

The three operating points studied in the boron transport simulations are given in Table 6.5. As with the previous simulations, the Bohm mobility coefficients are adjusted to match the measured discharge current for each operating point. However, for these simulation cases, a fourth empirical parameter is adjusted:

$$\hat{T}_e \equiv \frac{T_{e,\parallel}}{T_{e,\perp}}, \tag{6.3}$$

where $T_{e,\parallel}$ is the electron temperature in the direction parallel to the magnetic field lines and $T_{e,\perp}$ is the electron temperature in the direction normal to the field lines. As its form suggests, this parameter attempts to capture the anisotropic effects in the electron temperature. By varying this parameter between operating points, consistent values of $\alpha_c = 0.2$, $\alpha_e = 0.02$, and $\alpha_p = 10$ are achieved for the Bohm coefficients. The resulting values of $\hat{T}_e$ are 0.56, 0.62, and 0.72 for the 2 A, 4 A, and 6 A operating points, respectively. Note that $\hat{T}_e$ increases with increasing discharge current (or propellant mass flow rate). This makes sense, as an increase in mass flow rate results in a corresponding increase in pressure and collisionality in the discharge channel. The increase in collisionality causes some of the electron thermal energy directed normal to the magnetic field lines to be transferred to the direction parallel to the field lines, thus reducing the expected degree of anisotropy in the electron temperature.

Each operating point given in Table 6.5 is simulated twice, once for each of the Bohdansky fits shown in Table 4.3. The simulation mesh, time step, and other numerical quantities are the same as those used in the previous simulations. Approximately 50,000 boron macroparticles are present at any given time in all simulations.

6.2.1 Wall Probe Comparison

The operating conditions given in Table 6.5 been investigated using wall-mounted Langmuir probes,[97] providing a means to assess the accuracy of some of the computed plasma properties at the walls. At present, only the data for the 500 V, 4 A condition are available, so those data are used to provide a qualitative assessment of the accuracy of the numerical model.

The plasma potential at the wall for the 4 A operating point is plotted in Fig. 6.6. Because the HPHall domain boundaries mark the sheath edge rather than the wall, the plasma potential presented for the HPHall simulation is given by

$$\phi_w = \phi - \phi_s, \tag{6.4}$$

where ϕ_s is the *positive* sheath potential determined from the Hobbs and Wesson sheath model. As Fig. 6.6 indicates, the potential profile from the simulation shows good qualitative agreement with the experimental measurements, suggesting that the simulation accurately predicts the position of the acceleration zone. Quantitatively, the simulation appears to slightly underestimate the potential at the wall, although the difference is substantially greater for the inner wall than for the outer wall. This

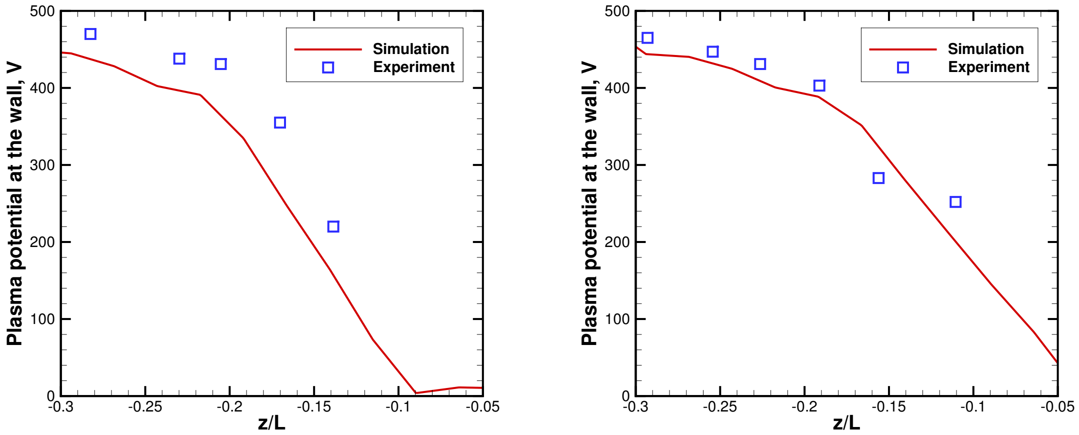

(a) Inner wall (b) Outer wall

Figure 6.6: Plasma potential at the walls with respect to ground for HiVHAc operating at 500 V, 4 A.

may indicate that there are some physical phenomena that are more significant near the inner channel wall than near the outer channel wall, and that the model is not adequately capturing those phenomena. Overall, however, the agreement between the wall probe measurements and the simulation results is fairly good, and along with the performance results, these data suggest that the numerical model is capturing many of the relevant physics.

6.2.2 Excitation and Ionization

Figure 6.7 shows calculated number density contours of ground-state boron and ^{4}P-state boron in HiVHAc operating at 500 V, 1 kW. The contours show that the peak density of the excited state is approximately three orders of magnitude smaller than that of the ground state for this operating point. For reference, the peak electron density is about a factor of 30 greater than the peak ground-state boron density computed using Bohdansky Fit B. This suggests that electronic excitation does not significantly affect the density of ground-state boron in the thruster discharge channel and near-field plume. Comparing the simulation results, we see that Bohdansky Fit B results in a greater boron density overall, as one would expect based its behavior in the limit of $\mathcal{E}_i \to \infty$.

Figure 6.8 shows contours of boron excitation rate and ionization rate for the 2 A operating point. Regardless of the Bohdansky fit used, the peak ionization rate is at least an order of magnitude greater than the peak excitation rate, indicating that ionization plays a much greater role than excitation in depleting the population of ground-state, neutral boron. However, the effects of ionization are likely still insignificant, as the reaction rate is too small to affect the ground-state boron density by more than a few percent.

Another point worth noting in Fig. 6.8 is that the boron excitation and ionization rates display some behavior that seems odd at first glance. Namely, the reaction rates are large both in the bulk plasma and in the immediate vicinity of the walls, with some minimum value in between. Ignoring the rate coefficient, the reaction rates are expected to be high in regions where the electron density and boron density are high. The electron density is expected to be high in the bulk plasma, just upstream of the acceleration zone, so the reaction rates are also high in that region. The boron density is greatest near the walls in the acceleration zone, causing the reaction rates to be large in those regions as well. Thus, the observed behavior in the reaction rates is to be expected and is not a cause for concern.

Because the discharge voltage is constant across the three operating points studied, one might predict that the electron temperature and the reaction rate coefficients are also constant. Based on the evidence presented above, this would also mean that excitation and ionization of boron are negligible for all three operating points. To verify this, Figs. 6.9 and 6.10 show the density of the ground and excited states of boron for the 4 A and 6 A operating points, respectively. As is the case for the 2 A point, the ground-state boron density is approximately 3 orders of magnitude greater

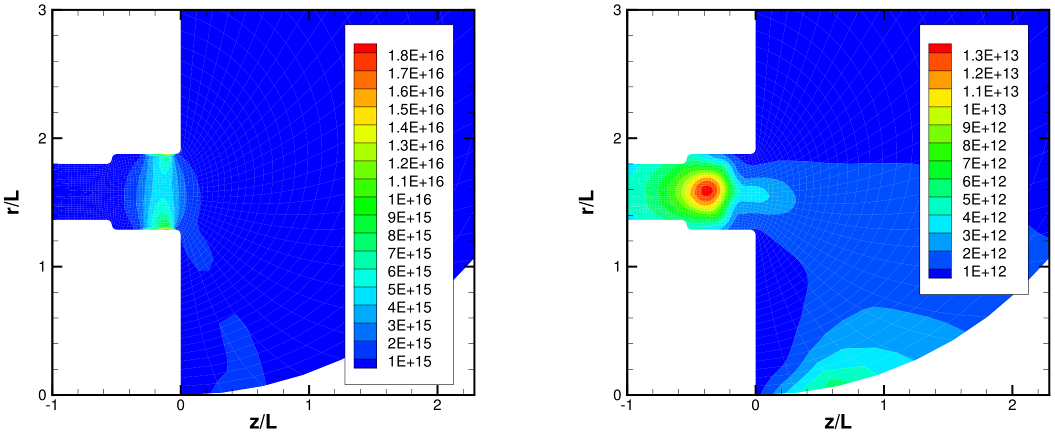

(a) Ground-state boron density, m^{-3}, Fit A. (b) ^{4}P-state boron density, m^{-3}, Fit A.

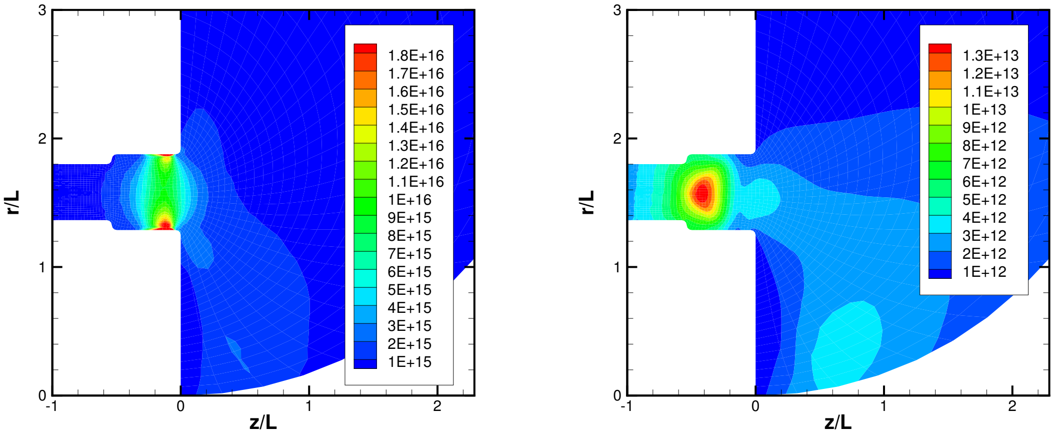

(c) Ground-state boron density, m^{-3}, Fit B. (d) ^{4}P-state boron density, m^{-3}, Fit B.

Figure 6.7: Contours of boron density for HiVHAc operating at 500 V, 2 A, for simulations using each of the two Bohdansky fits to the sputter yields.

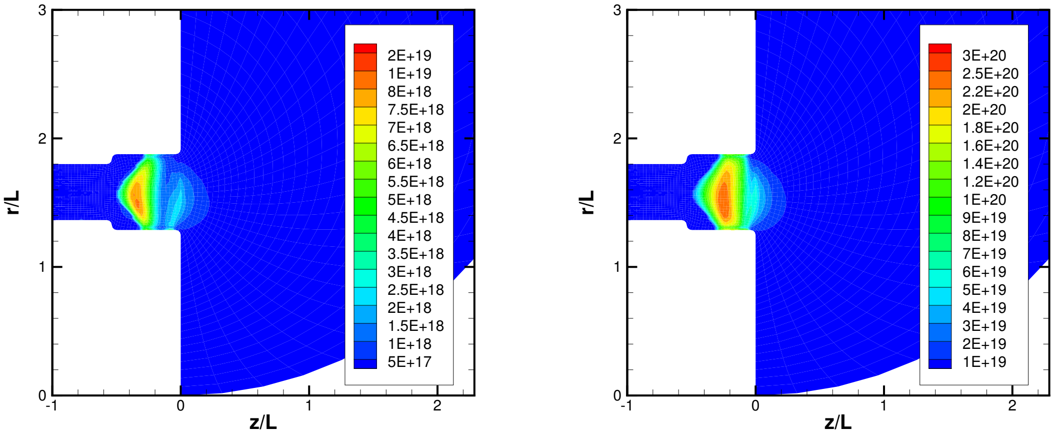

(a) Boron excitation rate, $\mathrm{m}^{-3}\mathrm{s}^{-1}$, Fit A (b) Boron ionization rate, $\mathrm{m}^{-3}\mathrm{s}^{-1}$, Fit A

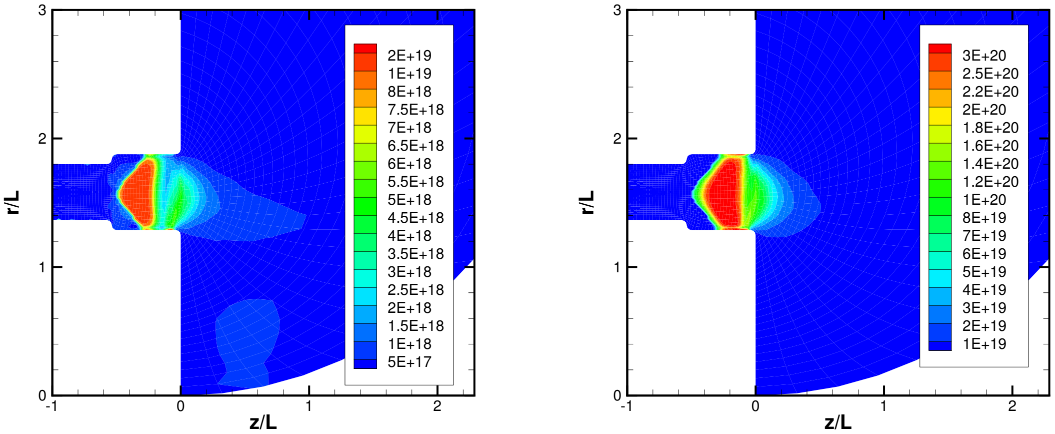

(c) Boron excitation rate, $\mathrm{m}^{-3}\mathrm{s}^{-1}$, Fit B (d) Boron ionization rate, $\mathrm{m}^{-3}\mathrm{s}^{-1}$, Fit B

Figure 6.8: Excitation and ionization rate of atomic boron in HiVHAc operating at 500 V, 2 A, for simulations using each of the two Bohdansky fits to the sputter yields.

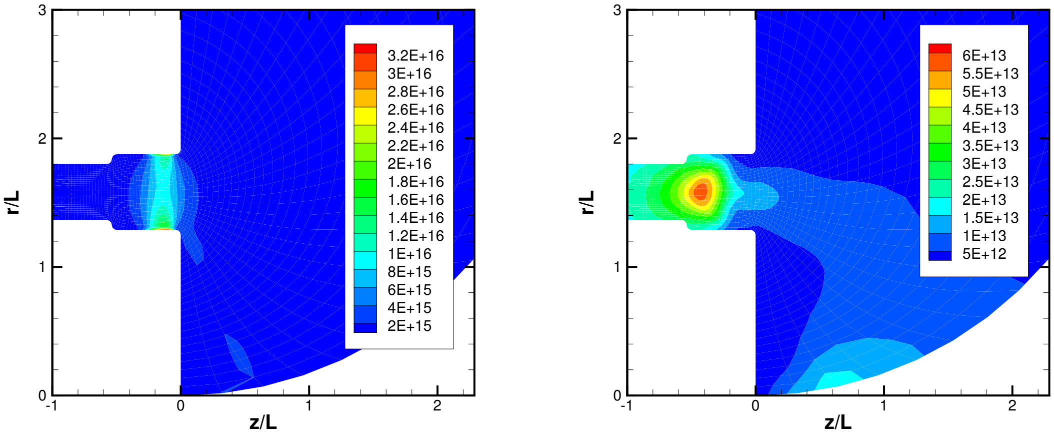

(a) Ground-state boron density, m^{-3}, Fit A.

(b) ^{4}P-state boron density, m^{-3}, Fit A.

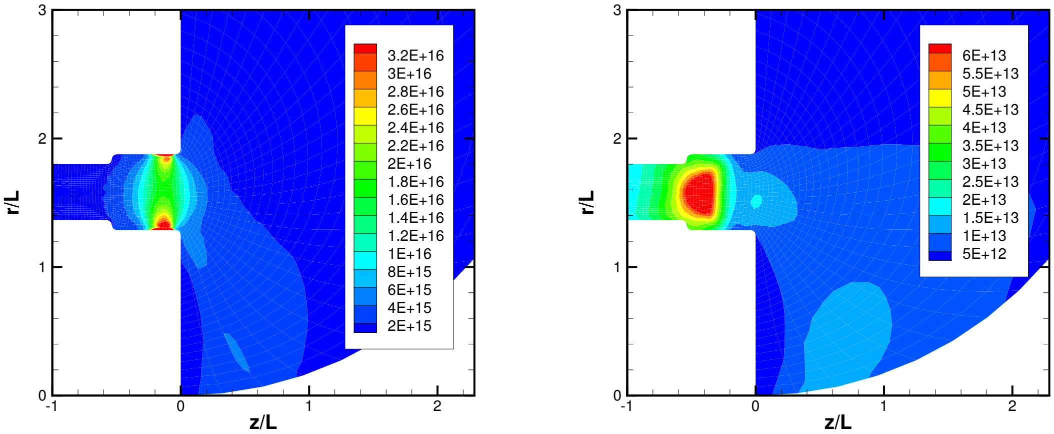

(c) Ground-state boron density, m^{-3}, Fit B.

(d) ^{4}P-state boron density, m^{-3}, Fit B.

Figure 6.9: Contours of boron density for HiVHAc operating at 500 V, 4 A, for simulations using each of the two Bohdansky fits to the sputter yields.

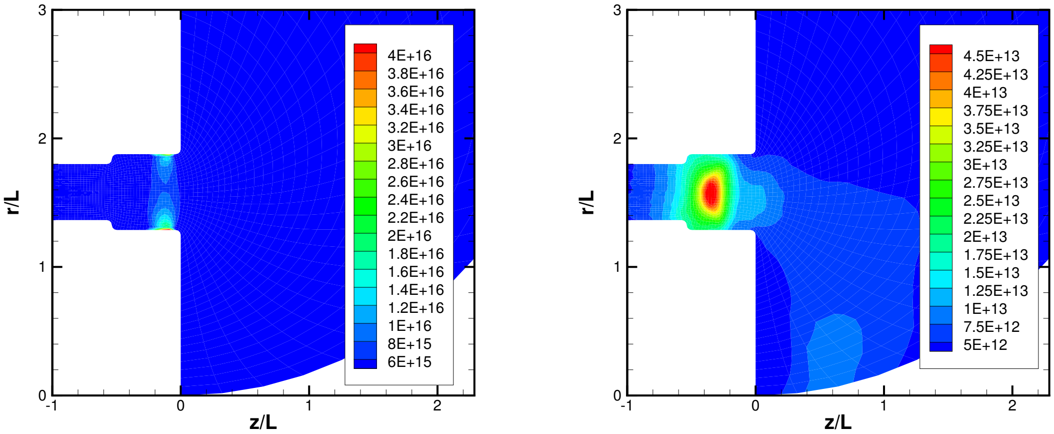

(a) Ground-state boron density, m^{-3}, Fit A. (b) ^{4}P-state boron density, m^{-3}, Fit A.

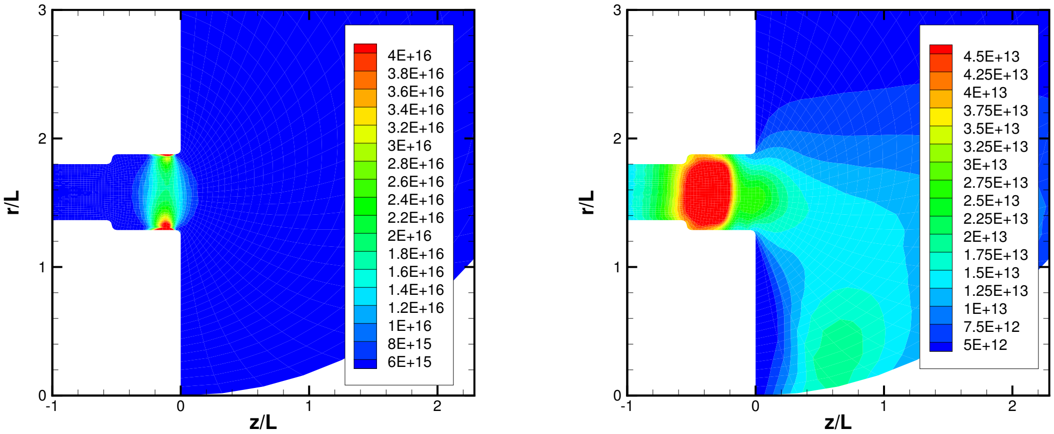

(c) Ground-state boron density, m^{-3}, Fit B. (d) ^{4}P-state boron density, m^{-3}, Fit B.

Figure 6.10: Contours of boron density for HiVHAc operating at 500 V, 6 A, for simulations using each of the two Bohdansky fits to the sputter yields.

than the excited-state density for these two operating points. Hence, excitation of boron is negligible for these operating conditions. One can then conclude that ionization of boron, although more significant than excitation, is also negligible based on the arguments made for the 2 A operating condition.

From the above observations, we can draw a very important conclusion: For Hall thrusters operating at 500 V discharge voltage or less, almost all boron atoms that are sputtered from the walls in the neutral, ground state remain in the neutral, ground state as they travel through the thruster and plume. This partially validates CRDS as a tool for measuring the density of sputtered boron in a Hall thruster plume, as investigation of the ground electronic state is sufficient to capture all boron atoms. However, based on the redeposition rate of boron macroparticles in the simulations, 56–61% of sputtered boron ultimately redeposits on a thruster surface. To fully validate CRDS as an *in situ* diagnostic for measurement of wall erosion in Hall thrusters, it must first be established that the fraction of boron that redeposits in the thruster is independent of the thruster operating condition. This falls within the present capabilities of the numerical model, but is left as a task for future investigation. Furthermore, it is possible that the sputtered boron atoms undergo electronic excitation or ionization during the sputtering event itself, in which case CRDS must investigate multiple electronic states in order to capture all of the eroded boron. Unfortunately, quantifying the fraction of boron that is excited or ionized during sputtering events is infeasible using MD, so this task is also left for future work.

6.2.3 Wall Recession Rate

In order to perform a simulated life test of a Hall thruster, one must know the linear recession rate of the discharge channel walls. This is computed from the erosion

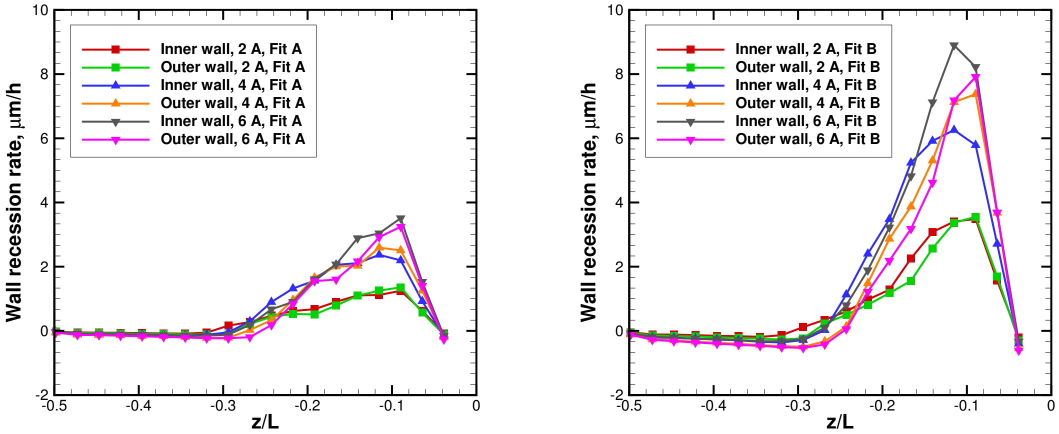

(a) Bohdansky Fit A

(b) Bohdansky Fit B

Figure 6.11: Calculated recession rate of the HiVHAc channel walls.

rate due to sputtering and the redeposition rate of boron:

$$\dot{N}_w = \dot{N}_e - \dot{N}_r, \tag{6.5}$$

where the erosion and redeposition rates are given in units of atoms per ion per unit azimuthal length. The linear recession rate of the walls can then be calculated on a per-cell basis as

$$\dot{r}_w = \frac{\dot{N}_w}{\Delta z} \frac{\mu_{BN}}{\rho_{BN}}, \tag{6.6}$$

where Δz is the axial width of the cell, μ_{BN} is the average molecular mass of h-BN, and ρ_{BN} is the mass density of h-BN.

The wall recession rate is plotted for both the inner and outer walls of HiVHAc in Fig. 6.11. The boron nitride density used is $1.95\,\mathrm{g/cm^3}$, the density of the HBC-grade BN produced by Momentive Performance Materials, Inc.[100] Several features are immediately evident from these plots:

1. The recession rates of the inner and outer walls are very similar, indicating that the plasma properties near the inner and outer walls are also similar. This is

consistent with the observations made in Sect. 6.2.1.

2. The overwhelming majority of the wall erosion occurs in the last 30% of the discharge channel's axial extent.

3. The recession rate has a maximum around $0.1\,L$ upstream of the channel exit, and decreases rapidly downstream of this point.

4. Between about $-0.5\,L$ and $-0.3\,L$, redeposition of boron is more significant than the sputter erosion of the h-BN walls, resulting in a negative recession rate.

All of these observations are more or less consistent with expectations: The majority of wall erosion should occur in the region of high electric field and electron temperature near the channel exit, where there is a population of energetic ions and the wall sheath potential is large. Upstream of this region, the ion density and wall sheath potential are much smaller, so there are very few ions with energies above the sputtering threshold, and boron deposition can outweigh what little erosion occurs.

With the method for determining the wall recession rate established, it is now possible to perform a simulated life test. The basic procedure for such a test is as follows:

1. Generate a mesh corresponding to the original, uneroded thruster geometry. This is the geometry at time $t = 0$.

2. Perform a simulation to calculate the time-averaged wall recession rate, $\dot{r}_w$.

3. Advance the mesh boundary nodes corresponding to the discharge channel walls by a distance $\dot{r}_w \Delta t$ to find the thruster geometry at time $t + \Delta t$.

4. Repeat steps 2 and 3 until the total recession of the inner or outer wall equals the initial thickness of the wall. At this point, the magnetic circuit is exposed to the plasma, and the time t at which this occurs is the operational life of the thruster.

Performing a simulated life test falls well within the model's present capabilities. All that is needed is an appropriate mission throttling table and time to perform the simulations. However, recall from Sect. 3.2.2.1 that the equilibrium temperature in the MD sputtering model is set to 150°C, a few hundred °C lower than the expected wall temperature in Hall thrusters. Because the sputter yield increases with temperature, the calculated wall erosion rates from the plasma model are likely less than what is expected during operation of a real thruster, and the calculated operational life from a simulated life test would likely be greater than the thruster's actual operational life. There is also substantial uncertainty regarding the boron redeposition, as the sticking coefficient for free boron may not be one, and the redeposited boron likely has a lower density than bulk BN. For these reasons, and because of the time investment involved, the task of performing a simulated Hall thruster life test is left for future work.

6.2.4 CRDS Comparison

To compare the 2D axisymmetric data produced by HPHall to the CRDS data directly, one must first integrate the boron density over the path of a virtual laser. Figure 6.12 shows a schematic of a virtual CRDS setup. The green line represents the laser, placed at a perpendicular distance r^* from the thruster centerline. The coordinate x follows the path of the laser, so the path-integrated boron density is

$$n_{PI} = \int_{-\infty}^{+\infty} n_B\left(r\right) dx. \tag{6.7}$$

One can define x in terms of r^* and the angle ψ as

$$x = r^* \tan\left(\psi\right). \tag{6.8}$$

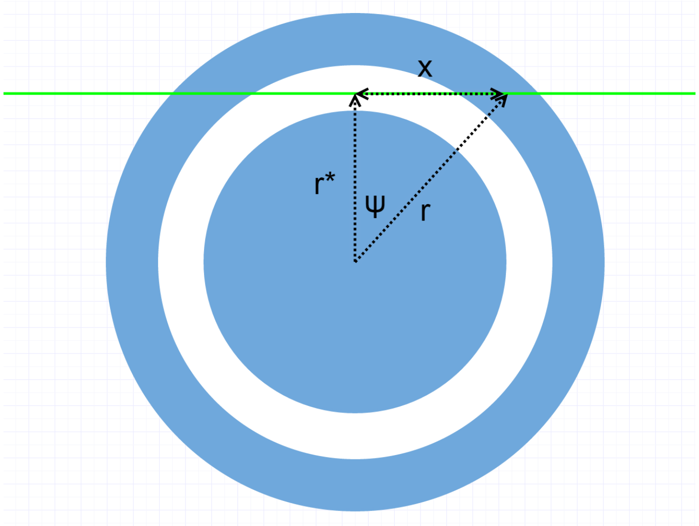

Figure 6.12: Schematic of a virtual CRDS setup, face-on view.

Similarly, the radial coordinate r can be defined as

$$r = \frac{r^*}{\cos\left(\psi\right)}. \tag{6.9}$$

Thus, Eq. 6.7 becomes

$$n_{PI}\left(r^*\right) = r^* \int_{-90^\circ}^{+90^\circ} \frac{n_B\left(\frac{r^*}{\cos(\psi)}\right)}{\cos^2\left(\psi\right)} d\psi. \tag{6.10}$$

In a real CRDS setup, the mirror cavity has a finite length. Lee reports a distance of 54 cm between mirrors[98], so the integration limits of Eq. 6.7 become ±27 cm, with corresponding angular bounds in Eq. 6.10. The integral is then evaluated numerically using a trapezoidal method to find the path-integrated boron density.

Figure 6.13 shows the path-integrated number density of ground-state boron as a function of the non-dimensional laser beam position P for each simulation case and for the CRDS measurements by Lee *et al.*[98] Simulations using each of the Bohdansky

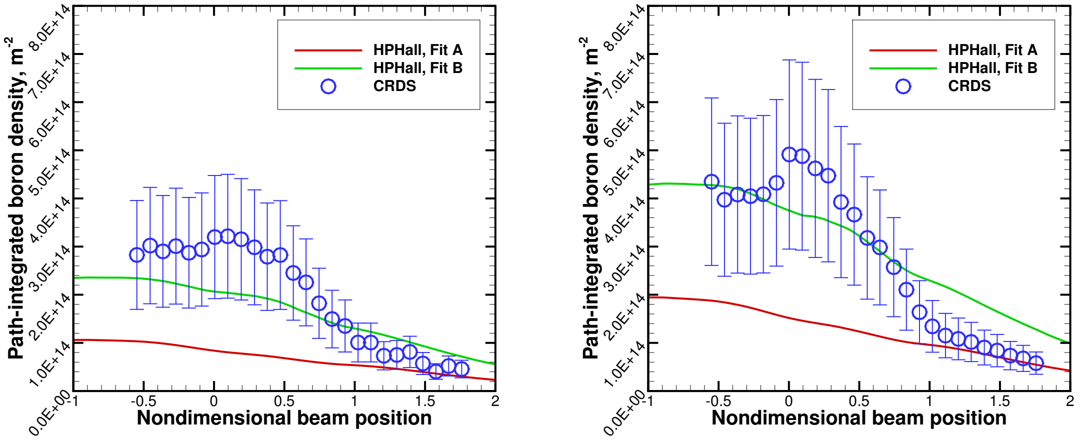

(a) 500 V, 2 A

(b) 500 V, 4 A

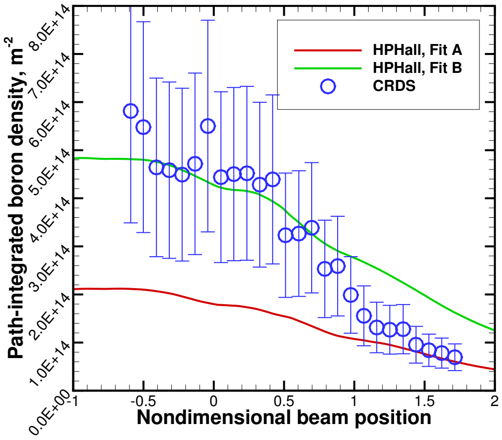

(c) 500 V, 6 A

Figure 6.13: Path-integrated density of ground-state atomic boron as found from the HPHall simulations and from the CRDS measurements.[98]

fits are presented. The non-dimensional beam position is defined as

$$P = \frac{r^* - r_{inner}}{r_{outer} - r_{inner}}. \tag{6.11}$$

The path-integrated boron density is computed 6 mm downstream of the thruster exit plane, consistent with Lee's experimental setup. The uncertainty in the CRDS measurements is estimated as 40% based on the work of Huang,[101] who found that the uncertainty in CRDS measurements of the path-integrated boron density decreases with increasing discharge voltage and propellant mass flow rate. For a mass flow rate of 10 mg/s in a 6 kW-class laboratory Hall thruster, Huang determined an uncertainty of about 40% for 300 V operation and 20% for 600 V operation. Although the discharge voltage considered here is quite high at 500 V, the propellant flow rate is less than 10 mg/s for all operating points studied, so the more conservative value of 40% is assumed.

The simulation results predict a more uniform distribution of boron overall, but otherwise they match the experimental measurements quite well, especially when Bohdansky Fit B is used. For $P \in (0, 1)$, the error relative to experiment does not exceed 60%. For the cases of 4 A and 6 A discharge current, the error is even smaller. This implies that the HPHall simulations are predicting the amount of sputtered boron that escapes into the plume with reasonable accuracy.

To further analyze the boron behavior, Fig. 6.14 shows the calculated boron number density as a function of nondimensional thruster radius R, defined in a manner similar to Eq. 6.11. Also shown are the CRDS data after being deconvolved using an "onion peeling" technique.[98,101] These plots more clearly demonstrate that the simulations predict a more uniform distribution of boron than is indicated by the CRDS measurements. However, both the simulations and measurements show a maximum in the boron density in the region of $R \in (0, 1)$, which corresponds to the region

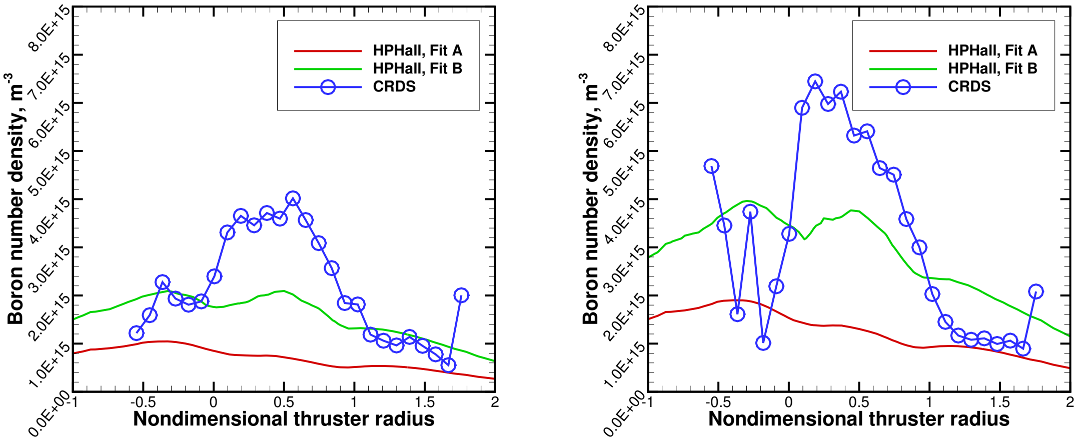

(a) 500 V, 2 A

(b) 500 V, 4 A

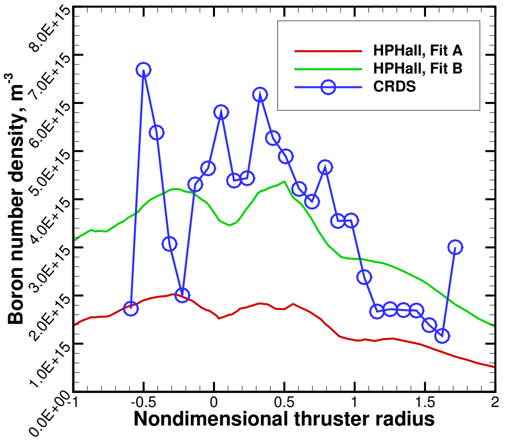

(c) 500 V, 6 A

Figure 6.14: Number density of ground-state atomic boron from the HPHall simulations and from the deconvolved CRDS measurements.[98] The CRDS data points are connected by straight lines to guide the reader.

immediately downstream of the discharge channel. A peak in the boron density is expected in this region, as the boron atoms sputtered from the inner and outer channel walls must cross paths at some point radially between the walls as they travel downstream. However, the simulation data also suggest that there is an additional peak in the boron density in the region of $R \in (-0.5, -0.2)$. There is some indication of a similar peak in the experimental data, but considerable scatter in the experimental data points in that region makes it difficult to draw a firm conclusion. A peak in this region is not expected, as there is no clear physical mechanism by which boron atoms should be concentrated there. This may be a numerical anomaly, as the number of boron macroparticles used in these simulations is quite small compared to the number of ion and neutral xenon macroparticles. Without additional evidence, however, it is difficult to investigate this phenomenon any further.

Although the agreement between the calculated and measured boron density is reasonably good given the numerous layers of assumptions in the numerical model, there are many sources of uncertainty in the simulation results that are difficult to quantify. Recall from Sect. 4.2.2 that the minimum ion energy for which sputtering was detected by the molecular dynamics model was 40 eV, so it was concluded that the threshold energy for sputtering of *h*-BN is between 30 eV and 40 eV. In that regard, and disregarding the previously noted uncertainty in the sputter yields at high ion energies, Bohdansky Fit A, with its corresponding threshold energy of 36 eV, could be considered more physically realistic than Bohdansky Fit B and its corresponding threshold energy of 48 eV. Yet, Bohdansky Fit A results in a significantly smaller boron density than is measured using CRDS. One likely explanation for this is the temperature of the BN walls. Recall from Sect. 3.2.2.1 that the prescribed equilibrium temperature of the *h*-BN lattice in the sputtering simulations was 150°C. In a Hall thruster, however, the walls are expected to reach temperatures of several hundred °C. The MD model has not yet been applied to characterize the temperature dependence of the total sputter yield, but it is certain that the sputter yield will increase in some fashion with increasing temperature. Based on this argument alone, using sputter yields that correspond to a higher wall temperature would likely improve the agreement between the simulation results and the measurements.

Another possible explanation for the relatively low boron density predicted when Bohdansky Fit A is used is the VDF of the sputtered boron atoms, particularly along the direction of forward sputtering. Recall from Sect. 5.2.3.2 that the mean velocity of the boron atoms along the forward sputtering direction is assumed to be zero regardless of ion energy or incidence angle. However, as was demonstrated in Sect. 4.4.2, the mean velocity in the forward sputtering direction is actually a strong function of the ion incidence angle, with more oblique incidence resulting in a greater mean velocity. If this preference for forward sputtering were included in the plasma model, then it is likely that more boron atoms would have trajectories that lead them into the plume rather than deeper into the discharge channel, thus increasing the boron density in the plume. Furthermore, including the preference for forward sputtering would also cause the predicted spatial distribution of boron to become less uniform immediately downstream of the channel exit, as a greater fraction of sputtered boron would be directed axially downstream.

6.2.5 Boron Transport in the Plume

A detailed analysis of the boron transport in the far-field plume falls outside the scope of this work, but it is still useful to consider the immediate behavior of the boron atoms as they exit the thruster. To this end, Fig. 6.15 shows contours of ground-state boron number density and streamlines of boron velocity for the 2 A and 6 A operating points, each using Bohdansky Fit B. The boron atoms of greatest interest are those with near-radial velocity vectors. These atoms are more likely to come into contact with spacecraft surfaces as a result of scattering collisions than

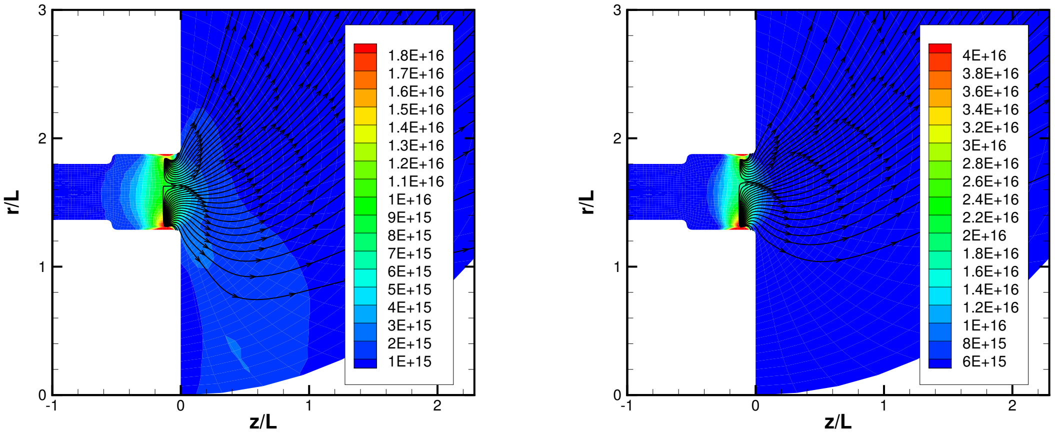

(a) 500 V, 2 A

(b) 500 V, 6 A

Figure 6.15: Contours of ground-state boron number density and streamlines of boron velocity in the near-field plume of HiVHAc.

those atoms that travel axially downstream. Boron that condenses on mission-critical components such as solar panels or optical lenses can impair proper function of those components and ultimately compromise the mission.

As Fig. 6.15 shows, there appear to be some boron atoms that travel almost purely in the outward radial direction. In order to properly capture the behavior of these particles in the far-field plume and around a spacecraft, a simulation with a much larger domain is required. The effects of scattering collisions involving boron must also be included, as these effects are likely much more significant in the plume given the long characteristic length scales of the plume and spacecraft. If bulk ionization of boron in the plume is negligible, then a rarefied gas simulation technique such as direct simulation Monte Carlo (DSMC)[44] would likely be able to capture the boron behavior. Otherwise, a DSMC-PIC method would be required. However, the development and application of such a model is a substantial undertaking, and is thus saved for later studies.

6.3 Summary

Presented in this chapter were the results of the HPHall simulations of NASA's HiVHAc thruster. The effects of the revised cross-sections for 0 → I and 0 → II ionization of xenon were assessed. The revised reactions were found to increase the predicted thrust and anode efficiency of HiVHAc at the operating points investigated, improving the agreement relative to experimental performance measurements. The plasma potential along the channel centerline was unaffected by the updated cross-sections, but the electron temperature was found to decrease slightly. The effects of triply-charged xenon were also investigated, and it was found the triple ions have no significant impact on either the thruster performance or the centerline plasma properties. Finally, the results of simulations including sputtered boron atoms were analyzed. Ionization and electronic excitation of boron in the bulk plasma were found to have a negligible effect on the density of neutral, ground-state boron, indicating that diagnostics such as CRDS need only probe the ground state in order to capture all boron atoms that escape the thruster. The plasma potential at the channel walls for the case of 500 V, 4 A was compared to measurements obtained using wall-mounted Langmuir probes.[97] The calculated potential at the outer channel wall was found to agree very well with the experimental measurements, but the potential at the inner wall was less than the measured value, possibly indicating that some of the physics near the inner wall are not being adequately captured by the model. Finally, the number density of neutral, ground-state boron was compared to measurements obtained using CRDS.[98] The agreement between the simulation results and the CRDS measurements was found to be very good given the numerous assumptions and sources of uncertainty associated with the numerical model.

CHAPTER VII

Summary and Conclusions

7.1 Dissertation Summary

Presented in this thesis was the development and application of a numerical model to predict the motion of particles eroded from the discharge channel walls of a Hall thruster during operation. The numerical model consists of two parts: A high-fidelity model of the sputtering of hexagonal boron nitride (*h*-BN) by xenon ions, and a separate model of a Hall thruster plasma discharge. By integrating the results of the sputtering model into the plasma model, direct monitoring of the erosion products within the plasma becomes possible.

The sputtering model utilizes the molecular dynamics (MD) method, and is based on work previously performed by Yim.[11,12] MD is a classical, deterministic technique that resolves the interactions between individual atoms according to a set of semi-empirical interatomic potential functions. The force on each atom is then derived from the potential functions, and the position of each atom is integrated according to the laws of classical mechanics. This method is as close to a first-principles approach as possible without introducing quantum force calculations, which would drastically increase the computational cost of the model.

The present MD model builds on the previous work in a few ways. First, the Molière potential previously used to model the interactions between the impacting xenon ions and the boron and nitrogen atoms in the *h*-BN lattice is replaced with the more accurate Ziegler-Biersack-Littmark (ZBL) potential function. Second, the model is implemented within the general purpose MD framework HOOMD-blue.[57] HOOMD-blue utilizes CUDA-based GPU hardware acceleration to reduce the computational cost of MD simulations by up to an order of magnitude compared to a 10-core CPU. For the sputtering model, this allows one to two orders of magnitude more ion impact events to be simulated compared to the previous model in the same amount of real time. This in turn reduces the statistical uncertainty in the calculated sputter yields, allowing the model to much better resolve the spatial and velocity distributions of the sputtered particles. Third, an algorithm for pre-conditioning the *h*-BN lattice is introduced. This algorithm adjusts the chemical composition and structure of the lattice in order to bypass the transient stages of sputtering. Other aspects of the previous model, such as the Albe-Möller potential used for the interactions between boron and nitrogen atoms and the Berendsen thermostat used for thermal regulation, are also used in the present model.

The sputtering model was applied to calculate the integrated sputter yield of *h*-BN under xenon ion bombardment as a function of the incident ion's energy and angle of incidence. The range of ion energies investigated extends from 20 eV up to 300 eV, covering the vast majority of ions that strike the discharge channel walls in a Hall thruster. The range of incidence angles studied extends from 0°, or normal incidence, up to 75°. For more oblique angles of incidence, the sputter yield decreases very rapidly towards zero, and due to the presence of the wall sheath, not many ions are expected to strike the walls of a Hall thruster at very oblique incidence in any case.

The integrated sputter yields at normal incidence were compared to experimental measurements obtained using a quartz crystal microbalance (QCM) by Rubin *et al.*[66] At very low ion energies ($\lesssim 100\,\mathrm{eV}$), the calculated yields fall below the lower bound of the QCM measurements. For higher ion energies ($\sim$ 150–300 eV), the calculated yields fall within the uncertainty of the QCM measurements, but extrapolation suggests that the calculated yields increase more rapidly with ion energy than the measured yields. This indicates that the sputtering model overestimates the integrated sputter yield at high ion energies, which may be an indication that domain independence is not established or that some physics are not being properly captured at those energies.

The minimum energy for which a finite sputter yield was found is 40 eV. Rubin also claims that the minimum energy for which sputtering was detected is 40 eV. Hence, both the sputtering model and the QCM measurements suggest that the threshold energy for sputtering of h-BN by xenon is between 30 eV and 40 eV for normal incidence. A more precise value for the threshold energy was determined by fitting a Bohdansky function[22] to the calculated sputter yields in a least-squares sense. Depending on the initial conditions of the fitting process, the evaluated threshold energy was found to be either 36 ± 3 eV (Fit A) or 48 ± 9 eV (Fit B). However, neither curve fit was found to capture the calculated sputter yields at ion energies greater than about 100–150 eV. A Bohdansky fit to the QCM measurements gives a threshold energy of 32 ± 6 eV, which is very consistent with Fit A to the calculated data.

Analysis of the angular dependence of the sputter yields showed that the peak in the calculated sputter yield occurred around 60° incidence for all simulation cases. The empirical Yamamura function was found to match the calculated sputter yields very well. The peak of the Yamamura curve occurred between 60° and 75° incidence for all cases. The sputtering model was also used to calculate the differential sputter yields of h-BN. The raw data were reduced by fitting a modified Zhang (MZ) function[70] for comparison to Rubin's QCM measurements.[66] Qualitatively, the MZ fits indicated that at normal ion incidence, the differential sputter yields take a diffuse, or cosine-like form, defined by the fit parameter ${}^{E^*}\!/_{\mathcal{E}_i} = 0$. For more oblique incidence angles, the value of ${}^{E^*}\!/_{\mathcal{E}_i}$ was found to increase, indicating an increased preference for forward sputtering. No clear dependence of ${}^{E^*}/_{\mathcal{E}_i}$ on the ion energy was observed. Compared to the QCM data, the values of ${}^{E^*}/_{\mathcal{E}_i}$ for the calculated sputter yields were shown to be a much stronger function of the incidence angle. It is unclear whether this difference indicates a deficiency in the model, as the reported uncertainty in the QCM data is quite high.

An analysis of the chemical composition of the sputtering products showed that *h*-BN tends to sputter in the form of atomic boron and diatomic nitrogen. Some atomic nitrogen and heavier B_xN_y particles were also detected, but in smaller amounts than B and N_2. Because boron is highly condensible, the sputtered boron atoms were studied further by calculating the 3D velocity distribution function (VDF) for each simulation case.

In the direction normal to the *h*-BN surface, the majority of the sputtered boron atoms were found to follow the Sigmund-Thompson distribution.[19–21] The observed behavior is corroborated by the laser-induced fluorescence (LIF) measurements of Tao and Yalin,[35,36] which also indicated that boron atoms sputtered from an *h*-BN target obey the Sigmund-Thompson distribution. Neglecting ion energies less than 100 eV, the average surface binding energy of boron as calculated from the Sigmund-Thompson fits to the MD data was found to be 4.5 eV, whereas the average value determined from the LIF data was 4.8 eV, a difference of only 6%. Hence, there is strong evidence that the sputtering model is accurately predicting the post-ejection behavior of the sputtered boron atoms, at least in the surface normal direction.

In the forward and transverse sputtering directions, the majority of the sputtered boron atoms were found to follow a Maxwell-Boltzmann distribution. The mean velocity in the forward direction was found to depend strongly on the ion incidence angle, with oblique incidence resulting in more positive values of the mean velocity. As with the differential sputter yields, this is an indication that forward sputtering is preferred at oblique angles of incidence. However, no clear dependence on ion energy was observed for a fixed angle of incidence, indicating that the additional energy deposited by higher-energy ions is dissipated through means other than the bulk flow of sputtered particles. Conversely, the mean velocity in the transverse sputtering direction was found to be approximately zero for all simulation cases, as the velocity component of the ions along that axis was zero by definition. The Maxwellian temperature in each direction showed a clear dependence on the energy and incidence angle of the bombarding ions, with the temperature increasing as the energy and incidence angle increase. This suggests that the additional energy deposited into the lattice at higher ion energies and incidence angles is preferentially dissipated through the thermal energy of the sputtered particles.

The plasma model used in this work was the hybrid-PIC code HPHall,[51] a very well established axisymmetric model for Hall thruster discharges. HPHall was updated to include the results of the sputtering model, allowing the dynamic calculation of the erosion rate at the walls and the introduction of boron atoms into the simulation domain. Ionization and electronic excitation of boron to a single metastable state were also included. In addition, the collision cross-sections for single and double ionization of neutral xenon were updated to better match experimental measurements at high electron energies, and triply-charged xenon ions and the associated ionization reactions were added to the code.

The updated version of HPHall was applied to simulate NASA's HiVHAc Hall thruster[93–96] at three operating points covering discharge voltages of 300–500 V and discharge currents of 7–10 A. The revised cross-sections for single and double ionization were found to have a small, but still noticeable effect on the centerline plasma properties, particularly the electron temperature. However, they had a very noticeable impact on the predicted thruster performance, improving the agreement between the measured and calculated values for thrust and anode efficiency. Triply-charged ions were found to have a negligible effect on both plasma properties and thruster performance, and were also found to introduce some numerical instabilities to the simulation. Hence, triple ions were ignored for the remaining simulation cases.

HPHall was then applied to characterize the behavior of eroded boron in HiVHAc at 500 V discharge voltage and 2 A, 4 A, and 6 A discharge current. Each operating point was simulated once for each of the two Bohdansky fits to the MD sputter yield data. It was found that excitation of boron atoms has a negligible effect on the density of ground-state boron at all three points, as the density of the ground state was three orders of magnitude greater than that of the excited state. Ionization was found to have a greater influence than excitation on the ground-state boron density, but the effects are still negligible because the reaction rates are too small to change the ground-state density by more than a few percent. Hence, the model indicates that, for Hall thrusters operating at 500 V or less, almost all (more than 99%) of boron atoms that are sputtered in the neutral, ground state, remain in the neutral, ground state as they travel through the discharge channel and near-field plume. This partially validates techniques such as cavity ring-down spectroscopy (CRDS) as erosion diagnostics, as these tools detect only one electronic state at a time.

The plasma potential along the HiVHAc channel walls was compared to measurements obtained using wall-mounted Langmuir probes for the 500 V, 4 A operating point.[97] The calculated potential profiles along both the inner and outer wall exhibited qualitative behavior very similar to the measurements, suggesting that the location of the acceleration zone in the simulations is approximately correct. Quantitatively, the potential along the outer wall showed excellent agreement with the measurements. Along the inner wall, the calculated potential was everywhere less than the measured potential, suggesting that something is occurring near the inner wall that the HPHall simulations cannot capture. However, the differences are no more than about 25%, and given the considerable level of uncertainty associated with plasma measurements and simulations, this level of agreement is deemed satisfactory.

Finally, the path-integrated number density of ground-state, neutral boron in the HiVHAc near-field plume was investigated for comparison to measurements obtained using CRDS[98] for the cases of 500 V discharge voltage and 2–6 A discharge current. Overall good agreement was found between the simulation results and the measurements. The simulations predicted a more uniform distribution of the boron atoms in general, and the simulations using Bohdansky Fit A generally underestimated the boron density at all three operating points, but the simulations using Bohdansky Fit B matched the measured data reasonably well. This indicates that the amount of boron that diffuses into the thruster plume in these simulations is physically realistic, and also provides additional validation for the MD sputtering model.

7.2 Unique Contributions

Several unique scientific contributions have been made through this work:

1. An improved molecular dynamics model for the sputtering of hexagonal boron nitride by xenon ions was developed. The MD simulations indicated that nitrogen is sputtered preferentially over boron during the early stages of ion bombardment, resulting in a boron-enriched surface, and that the sputtering rate of boron is roughly constant with increasing ion fluence.

2. The threshold energy for sputtering of *h*-BN at normal incidence was found to lie between 30 eV and 40 eV. This observation is heavily corroborated by existing experimental evidence.

3. It was determined that *h*-BN sputters primarily in the form of N_2 and B, with a smaller amount of N and some heavy compounds of B and N. This suggests that boron is the most abundant condensible product of wall erosion in Hall thrusters.

4. The behavior of sputtered boron atoms was characterized and they were found to follow the theoretically-predicted Sigmund-Thompson velocity distribution in the direction normal to the bombarded BN surface. This is the first known numerical model to demonstrate this behavior for a multi-component material.

5. The surface binding energy of boron in *h*-BN was calculated to be 4.5 eV for bombardment by ions of 100 eV and greater kinetic energy. This agrees with the measured value of 4.8 eV to within 6%.

6. The *h*-BN sputter yields and boron velocity distributions were implemented within the established hybrid-PIC model HPHall. The updated model was then applied to simulate a Hall thruster with dynamic production of erosion products at the discharge channel walls as the simulations progressed. No such simulations have been performed using a Hall thruster plasma model in the past.

7. Single ionization of boron and excitation of boron to a single metastable state were included in the plasma model, and it was shown that bulk ionization and excitation of sputtered boron in a Hall thruster are negligible. This partially validates cavity ring-down spectroscopy (CRDS) as an *in situ* diagnostic for measuring Hall thruster channel erosion.

8. The calculated boron density 6 mm downstream of the thruster channel exit was compared to CRDS measurements of ground-state boron. The agreement between the calculated and measured boron density was shown to be reasonably good given the numerous assumptions and sources of uncertainty associated with the MD and plasma models.

7.3 Future Work

There are numerous ways in which to build upon the work presented in this thesis, and many of them relate to uncertainties in the MD sputtering model. For instance, recall that the integrated sputter yield calculated from the MD results seemed to increase more rapidly than the QCM measurements for energies of about 150 eV and greater. In fact, the growth in the sputter yield appears roughly linear, whereas the QCM measurements and the fitted Bohdansky curve appear to approach an asymptotic value for the sputter yield in the limit of infinite ion energy. One possible cause for the observed increase in the calculated sputter yields is that domain independence is not yet established for the high-energy simulation cases, meaning the simulated lattice is not large enough to contain the energy cascade induced by the impacting ion. For small domains, the energy deposited by the ion per lattice atom is higher on average than for larger domains, so it makes sense that the calculated sputter yields might appear too large if the simulation domain is too small. Hence, the domain sizes used for these cases may need to be increased until the calculated sputter yield becomes independent of the lattice dimensions.

An alternative explanation for the high sputter yields at energies greater than about 150 eV is the effect of B–B bonds. Recall from Chapter III that the Albe-Möller potential parameters for B–B bonds differ from those originally proposed by Albe and Möller. The altered parameters were inherited from Yim's work, where it was found that the original parameters caused a strong sensitivity of B–B bonds to bond angles with tertiary atoms, thus requiring a prohibitively small time step to resolve the atomic motion. The change was justified by noting that B–B bonds do not occur in bulk BN. However, this work has demonstrated that the sputtering of *h*-BN results in the formation of an amorphous layer of pure boron at the exposed surface. B–B bonds are, naturally, abundant in this layer, and the boron layer tends to grow thicker with increasing ion energy, making the B–B bonds very important for sputtering by high-energy ions. Thus, repeating the sputtering simulations with the original Albe-Möller parameters may result in more realistic sputter yields at high ion energies.

Another unexplored aspect of the MD results is the existence of condensible species besides atomic boron. As was noted in Chapter IV, atomic nitrogen makes up a significant fraction of nitrogen-containing species, and its behavior has not yet been characterized. Atomic nitrogen can be considered condensible due to its tendency to form compounds with many other elements, and if nitrogen atoms sputtered in a Hall thruster condense on the BN walls, this serves to reduce the net erosion rate just as the redeposition of boron does. It is also possible that not all particles of a "condensible" species actually condense upon contact with a surface as was assumed in the boron transport simulations. One means by which to test this is to perform MD simulations similar in nature to the sputtering simulations, only with the impacting xenon ions replaced with boron atoms or other condensible particles. The fraction of these particles that ultimately bond to the surface could then be quantified.

Yet another question regarding the MD results is the origin of the anomalous population of low-energy boron atoms that appears among the sputtered particles. The majority of sputtered boron atoms follow the Sigmund-Thompson and Maxwellian distributions discussed above, but the anomalous atoms appear to follow a different VDF entirely. The source of these particles is not known, but one possibility is that they are an undesired consequence of the lattice pre-conditioning algorithm. This algorithm perturbs the lattice atoms stochastically in order to approach a local minimum in the system's potential energy. However, there is no guarantee that the resulting structure exactly resembles that produced by extensive sputtering. For example, it is possible for the pre-conditioner to generate "fingers" of boron atoms extending into the space above the lattice surface, whereas it is unlikely that such a structure would form as a result of continuous ion bombardment. The atoms in such structures may easily detach from the lattice and drift slowly away, resulting in a population of low-energy “sputtered” particles. Running additional simulations that start from a perfect lattice should reveal whether this is the case.

As a final note regarding the MD model, recall that the prescribed equilibrium temperature of the h-BN lattice was 150°C. This temperature was selected because many researchers have reported the sample temperature during sputtering experiments as 150°C. However, the wall temperature in a Hall thruster is generally a few hundred degrees Celsius. The integrated sputter yields at such temperatures are expected to be greater than the sputter yields reported for 150°C, but the exact temperature dependence of the sputter yields is not known. Thus, determining that dependence is an obvious step towards improving the accuracy of the wall erosion calculations in Hall thrusters.

There are also some steps that can be taken to test the updated erosion submodel of HPHall. Recall from Chapter V that the angular dependence of the sputter yield and the boron VDFs in the forward and transverse sputtering directions were assumed to be independent of ion energy and incidence angle, in spite of the fact that the MD results showed otherwise. This assumption was made for the sake of simplicity, but it is likely that these dependencies will ultimately affect the predicted boron density in the thruster and plume. The boron VDFs in particular are worth studying, as the MD results indicate a clear increase in the mean velocity along the forward sputtering direction, and in the Maxwellian temperature for the forward and transverse directions, with increasing angle of incidence. At minimum, a parametric study can be performed by adjusting the mean velocity and temperature of the Maxwellian distributions and observing the changes in the boron density.

Another way to test the erosion submodel is to perform a simulated life test. This involves calculating the time-averaged recession rate of the walls for some initial geometry and then adjusting the mesh boundaries according to that erosion rate using a finite time step. The simulation is then iterated between these two steps until the "failure" point is reached, where the depth of the erosion corresponds to the thickness of the thruster walls. Such a test falls well within HPHall's present capabilities, but simply requires time and a suitable throttling table to complete.

Finally, there are several changes that could be made to the plasma model in order to improve its fidelity. Namely, the quasi-1D electron model may not be adequate for accurately computing the local plasma properties. This is especially true of the novel magnetically-shielded thrusters, in which the magnetic field topology is much more complicated than in a traditional Hall thruster. Instead, a fully 2D model could be utilized, such as in the Hall thruster fluid model Hall2De,[40] enabling the simulation of wall erosion and boron transport in magnetically-shielded thrusters. In addition, the effects of triply-charged ions become more important at higher discharge voltages and in magnetically-shielded designs, so the stability issues associated with triply-charged xenon must be resolved in order to study those conditions.

APPENDICES

APPENDIX A

Differentiation of Interatomic Potentials

A.1 Vector Differentiation Identities

The force on a particle i is derived from the potential field as the negative gradient of the potential with respect to the position of particle i: $\mathbf{F}_i = -\nabla_{\mathbf{r}_i}\Phi$. The gradient with respect to $\mathbf{r}_i$ can be written as

$$\nabla_{\mathbf{r}_i} = \hat{\mathbf{x}}\frac{\partial}{\partial x_i} + \hat{\mathbf{y}}\frac{\partial}{\partial y_i} + \hat{\mathbf{z}}\frac{\partial}{\partial z_i}. \tag{A.1}$$

The gradient of the dot product of two vectors $\mathbf{r}_i$ and $\mathbf{r}_j$ can then be written as

$$\nabla_{\mathbf{r}_q}\left(\mathbf{r}_i \cdot \mathbf{r}_j\right) = \mathbf{r}_i\delta_{jq} + \mathbf{r}_j\delta_{iq}, \tag{A.2}$$

where δ is the Kronecker delta function. Noting that the magnitude of a vector $\mathbf{r}$ is given by $\sqrt{\mathbf{r}\cdot\mathbf{r}}$, the gradient of $r_{ij} = |\mathbf{r}_j - \mathbf{r}_i|$ with respect to $\mathbf{r}_q$ becomes

$$\begin{aligned}\nabla_{\mathbf{r}_q} r_{ij} &= \frac{1}{2r_{ij}} \nabla_{\mathbf{r}_q}\left(\mathbf{r}_{ij}\cdot\mathbf{r}_{ij}\right), \\ &= \frac{\left(\mathbf{r}_j - \mathbf{r}_i\right)\left(\delta_{jq} - \delta_{iq}\right)}{r_{ij}}, \\ &= \hat{\mathbf{r}}_{ij}\left(\delta_{jq} - \delta_{iq}\right). \end{aligned} \tag{A.3}$$

Thus, the gradient of r_{ij} with respect to the position of particle i or j always points along the direction of $\mathbf{r}_{ij}$ or $-\mathbf{r}_{ij}$.

A.2 Derivative of the ZBL Potential

The force on atom i due to the ZBL potential interaction with atom j (excluding the cutoff function) is given by

$$\mathbf{F}_i = -\nabla_{\mathbf{r}_i}\Phi_{ZBL} = -\hat{\mathbf{r}}_{ij}\frac{Z_i Z_j e^2}{4\pi\varepsilon_0 r_{ij}} \sum_{n=1}^{4} A_n \left(\frac{1}{r_{ij}} + \frac{B_n}{a_F}\right) \exp\left(-B_n \frac{r_{ij}}{a_F}\right), \tag{A.4}$$

where the coefficients A_n and B_n take the values given in Table 3.2. In contrast, the force on particle j is

$$\mathbf{F}_j = -\nabla_{\mathbf{r}_j}\Phi_{ZBL} = \hat{\mathbf{r}}_{ij}\frac{Z_i Z_j e^2}{4\pi\varepsilon_0 r_{ij}} \sum_{n=1}^{4} A_n \left(\frac{1}{r_{ij}} + \frac{B_n}{a_F}\right) \exp\left(-B_n \frac{r_{ij}}{a_F}\right), \tag{A.5}$$

so that the force on j is equal and opposite to that on i, as one would expect from Newton's third law.

A.3 Derivative of the Albe-Möller Potential

Due to its three-body nature, the Albe-Möller potential is much more difficult to differentiate than the ZBL potential. Using the notation $\nabla_{\mathbf{r}_q} f = f'$, the force can be written as

$$\mathbf{F}_q = -\nabla_{\mathbf{r}_q}\Phi_{AM} = -\frac{1}{2}\left[f'_C\left(f_R - b_{ij}f_A\right) + f_C\left(f'_R - b'_{ij}f_A - b_{ij}f'_A\right)\right]. \tag{A.6}$$

We can then define the various derivatives from the vector differentiation identities:

$$f'_C\left(r_{ij}\right) = -\left(\delta_{jq} - \delta_{iq}\right)\begin{cases} 0, & r_{ij} \leq R - D \\ \frac{3\alpha\hat{r}}{2D\left(\hat{r}^3-1\right)^2}\exp\left(\frac{3\hat{r}^3}{\hat{r}^3-1}\right), & R - D < r_{ij} < R + D\,, \\ 0, & r_{ij} \geq R + D \end{cases} \tag{A.7}$$

$$f'_R\left(r_{ij}\right) = -\frac{D_0\beta\sqrt{2S}}{S-1}\exp\left(-\beta\sqrt{2S}\left(r_{ij} - r_0\right)\right)\hat{\mathbf{r}}_{ij}\left(\delta_{jq} - \delta_{iq}\right), \tag{A.8}$$

$$f'_A\left(r_{ij}\right) = -\frac{D_0\beta\sqrt{2S}}{S-1}\exp\left(-\beta\sqrt{2/S}\left(r_{ij} - r_0\right)\right)\hat{\mathbf{r}}_{ij}\left(\delta_{jq} - \delta_{iq}\right). \tag{A.9}$$

The derivative of the term b_{ij} is given by

$$b'_{ij} = -\frac{1}{2n}\gamma^n\chi_{ij}^{n-1}\left[1 + \left(\gamma\chi_{ij}\right)^n\right]^{-1/2n-1}\chi'_{ij}, \tag{A.10}$$

$$\begin{aligned}\chi'_{ij} = \sum_{k\neq i,j}\Big[&f_C\left(r_{ik}\right)g\left(\theta_{ijk}\right)3\lambda^3\left(r_{ij} - r_{ik}\right)^2\left(\hat{\mathbf{r}}_{ij}\left(\delta_{jq} - \delta_{iq}\right) - \hat{\mathbf{r}}_{ik}\left(\delta_{kq} - \delta_{iq}\right)\right) \\ &+ f'_C\left(r_{ik}\right)g\left(\theta_{ijk}\right) + f_C\left(r_{ik}\right)g'\left(\theta_{ijk}\right)\Big]\exp\left(\lambda^3\left(r_{ij} - r_{ik}\right)^3\right),\end{aligned} \tag{A.11}$$

$$g'\left(\theta_{ijk}\right) = -\frac{2c^2\left(h - \cos\left(\theta_{ijk}\right)\right)}{\left[d^2 + \left(h - \cos\left(\theta_{ijk}\right)\right)^2\right]^2}\nabla_{\mathbf{r}_q}\cos\left(\theta_{ijk}\right). \tag{A.12}$$

$\cos\left(\theta_{ijk}\right)$ can be written in terms of the vectors $\mathbf{r}_{ij}$ and $\mathbf{r}_{ik}$ as

$$\cos\left(\theta_{ijk}\right) = \frac{\mathbf{r}_{ij}\cdot\mathbf{r}_{ik}}{r_{ij}r_{ik}}, \tag{A.13}$$

or, by expanding terms,

$$\cos\left(\theta_{ijk}\right) = \frac{\mathbf{r}_j\cdot\mathbf{r}_k - \mathbf{r}_j\cdot\mathbf{r}_i - \mathbf{r}_i\cdot\mathbf{r}_k + \mathbf{r}_i\cdot\mathbf{r}_i}{r_{ij}r_{ik}}. \tag{A.14}$$

The derivative of the cosine term is then

$$\begin{aligned}
\nabla_{\mathbf{r}_q} \cos\left(\theta_{ijk}\right) &= \frac{1}{r_{ij} r_{ik}} \left[\left(\mathbf{r}_j \delta_{kq} + \mathbf{r}_k \delta_{jq}\right) - \left(\mathbf{r}_j \delta_{iq} + \mathbf{r}_i \delta_{jq}\right) - \left(\mathbf{r}_i \delta_{kq} + \mathbf{r}_k \delta_{iq}\right) + 2\mathbf{r}_i \delta_{iq} \right] \\
&\quad - \frac{\mathbf{r}_{ij} \cdot \mathbf{r}_{ik}}{r_{ij}^2 r_{ik}^2} \left[r_{ij} \hat{\mathbf{r}}_{ik} \left(\delta_{kq} - \delta_{iq}\right) + r_{ik} \hat{\mathbf{r}}_{ij} \left(\delta_{jq} - \delta_{iq}\right) \right], \\
&= \frac{1}{r_{ij} r_{ik}} \Big[- \left(\mathbf{r}_{ij} + \mathbf{r}_{ik} - \left(r_{ij} \hat{\mathbf{r}}_{ik} + r_{ik} \hat{\mathbf{r}}_{ij} \right) \cos\left(\theta_{ijk}\right) \right) \delta_{iq} \\
&\quad + \left(\mathbf{r}_{ik} - r_{ik} \cos\left(\theta_{ijk}\right) \hat{\mathbf{r}}_{ij} \right) \delta_{jq} \\
&\quad + \left(\mathbf{r}_{ij} - r_{ij} \cos\left(\theta_{ijk}\right) \hat{\mathbf{r}}_{ik} \right) \delta_{kq} \Big], \\
&= - \left[\left(\frac{1}{r_{ik}} - \frac{\cos\left(\theta_{ijk}\right)}{r_{ij}} \right) \hat{\mathbf{r}}_{ij} + \left(\frac{1}{r_{ij}} - \frac{\cos\left(\theta_{ijk}\right)}{r_{ik}} \right) \hat{\mathbf{r}}_{ik} \right] \delta_{iq} \\
&\quad + \left[- \frac{\cos\left(\theta_{ijk}\right)}{r_{ij}} \hat{\mathbf{r}}_{ij} + \frac{1}{r_{ij}} \hat{\mathbf{r}}_{ik} \right] \delta_{jq} \\
&\quad + \left[\frac{1}{r_{ik}} \hat{\mathbf{r}}_{ij} - \frac{\cos\left(\theta_{ijk}\right)}{r_{ik}} \hat{\mathbf{r}}_{ik} \right] \delta_{kq}. \qquad \text{(A.15)}
\end{aligned}$$

Finally, by substituting this into Eq. A.12 and following the subsequent chain of substitutions, one can derive the force on each particle i, j, and k.

APPENDIX B

Tabulated Sputter Yield Data

Table B.1: Lattice dimensions in the surface plane for all MD simulations, measured in point-to-point hexagons and graphene-like layers.

Ion energy, eV	Incidence angle	Hexagons	Layers
40	0°	15	20
	45°	15	20
	60°	15	20
	75°	15	20
60	0°	18	24
	15°	18	24
	30°	18	24
	45°	18	24
	60°	18	24
	75°	18	24
80	0°	21	28

Continued on next page.

Table B.1 – *Continued from previous page.*

Ion energy, eV	Incidence angle	Hexagons	Layers
80	45°	21	28
	60°	21	28
	75°	21	28
100	0°	24	32
	15°	24	32
	30°	24	32
	45°	24	32
	60°	24	32
	75°	24	32
150	0°	24	32
	45°	24	32
	60°	24	32
	75°	24	32
200	0°	24	32
	30°	24	32
	45°	24	32
	60°	24	32
	75°	24	32
250	0°	30	40
	45°	30	40
	60°	30	40
	75°	30	40

Continued on next page.

Table B.1 – *Continued from previous page.*

Ion energy, eV	Incidence angle	Hexagons	Layers
300	0°	30	40
	60°	30	40
	75°	30	40

Table B.2: Calculated sputter yield, ${}^{E^*}/_{\mathcal{E}_i}$, surface binding energy, and m for all MD simulations. The total yield is calculated according to Eq. 4.1.

Ion energy, eV	Incidence angle	Y, atoms/ion	${}^{E^*}/_{\mathcal{E}_i}$	U_b, eV	m
40	0°	0.002	0.20	1.7	0.12
	45°	0.001	0.50	2.8	0.0
	60°	0.002	0.52	2.5	0.0
	75°	0.002	0.39	3.5	0.0
60	0°	0.011	0.07	2.7	0.0
	15°	0.009	0.02	2.6	0.0
	30°	0.014	0.18	3.1	0.0
	45°	0.019	0.09	3.3	0.0
	60°	0.019	0.35	3.2	0.0
	75°	0.004	0.88	4.4	0.0
80	0°	0.043	0.0	3.4	0.0
	45°	0.040	0.56	1.0	0.36
	60°	0.073	0.32	4.1	0.0
	75°	0.013	1.0	1.2	0.28
100	0°	0.11	0.0	4.0	0.0
	15°	0.12	0.0	4.1	0.0

Continued on next page.

Table B.2 – *Continued from previous page.*

Ion energy, eV	Incidence angle	Y, atoms/ion	$^{E^*}/_{\mathcal{E}_i}$	U_b, eV	m
100	30°	0.13	0.01	4.3	0.0
	45°	0.15	0.13	3.9	0.0
	60°	0.23	0.27	4.2	0.0
	75°	0.074	0.74	4.2	0.0
150	0°	0.32	0.0	4.8	0.0
	45°	0.53	0.16	4.5	0.0
	60°	0.65	0.34	4.8	0.0
	75°	0.40	0.58	6.0	0.0
200	0°	0.58	0.0	5.1	0.0
	30°	0.63	0.0	5.9	0.0
	45°	0.97	0.17	4.8	0.0
	60°	1.4	0.44	4.2	0.07
	75°	1.1	0.97	4.0	0.11
250	0°	0.90	0.0	5.7	0.0
	45°	1.4	0.15	4.8	0.08
	60°	2.1	0.37	4.7	0.19
	75°	1.7	1.0	3.0	0.23
300	0°	1.1	0.0	5.7	0.0
	60°	2.7	0.33	4.2	0.21
	75°	2.7	0.98	3.0	0.32

BIBLIOGRAPHY

BIBLIOGRAPHY

[1] National Coordination Office for Space-Based Positioning, Navigation, and Timing, "GPS Accuracy," `http://www.gps.gov/systems/gps/performance/accuracy/`.

[2] Wertz, J. R. and Larson, W. J., editors, *Space Mission Analysis and Design*, Microcosm Press, Hawthorne, CA, 3rd ed., 2008.

[3] Zhurin, V. V., Kaufman, H. R., and Robinson, R. S., "Physics of closed drift thrusters," *Plasma Sources Science and Technology*, Vol. 8, No. 1, 1999, pp. R1–R20. doi:10.1088/0963-0252/8/1/021.

[4] Estublier, D., "The SMART-1 Spacecraft Potential Investigations," *IEEE Transactions on Plasma Science*, Vol. 36, No. 5, 2008, pp. 2262–2270. doi:10.1109/TPS.2008.2002032.

[5] Racca, G. D., "SMART-1 from Conception to Moon Impact," *Journal of Propulsion and Power*, Vol. 25, No. 5, 2009, pp. 993–1002. doi:10.2514/1.36278.

[6] "AEHF-1 Satellite Arrives at Its Operational Orbit After 14-Month Journey," *Space Daily*, November 2011.

[7] Gates, M., Stich, S., McDonald, M., Muirhead, B., Mazanek, D., Abell, P., and Lopez, P., "The Asteroid Redirect Mission and sustainable human exploration," *Acta Astronautica*, Vol. 111, 2015, pp. 29–36. doi:10.1016/j.actaastro.2015.01.025.

[8] Strange, N., Landau, D., Mcelrath, T., Lantoine, G., Lam, T., Mcguire, M., Burke, L., Martini, M., and Dankanich, J., "Overview of Mission Design for NASA Asteroid Redirect Robotic Mission Concept," *33rd International Electric Propulsion Conference*, IEPC Paper 2013-321, Washington, DC, USA, Oct. 2013.

[9] Absalamov, S. K., Andreev, V. B., Colbert, T., Day, M., Egorov, V. V., Gnizdor, R., Kaufman, H., Kim, V., Korakin, A., Kozubsky, K., Kudravzev, S., Lebedev, U., Popov, G., and Zhurin, V., "Measurement of Plasma Parameters in the Stationary Plasma Thruster (SPT-100) Plume and its Effect on Spacecraft Components," *28th AIAA/SAE/ASME/ASEE Joint Propulsion Conference & Exhibit*, AIAA Paper 1992-3156, Nashville, Tennessee, USA, July 1992.

[10] Garner, C. E., Brophy, J. R., Polk, J. E., and Pless, L. C., "A 5,730-Hr Cyclic Endurance Test of the SPT-100," *31st AIAA/ASME/SAE/ASEE Joint Propulsion Conference & Exhibit*, AIAA Paper 1995-2667, San Diego, California, USA, July 1995.

[11] Yim, J. T., *Computational Modeling of Hall Thruster Channel Wall Erosion*, Ph.D. thesis, University of Michigan, 2008.

[12] Yim, J. T., Falk, M. L., and Boyd, I. D., "Modeling low energy sputtering of hexagonal boron nitride by xenon ions," *Journal of Applied Physics*, Vol. 104, No. 12, 2008, pp. 123507.

[13] Grys, K. D., Welander, B., Dimicco, J., Wenzel, S., Kay, B., Khayms, V., and Paisley, J., "4.5 kW Hall Thruster System Qualification Status," *41st AIAA/ASME/SAE/ASEE Joint Propulsion Coference & Exhibit*, AIAA Paper 2005-3682, Tucson, Arizona, USA, 2005. doi:10.2514/6.2005-3682.

[14] Welander, B., Carpenter, C., Grys, K. H. D., Hofer, R. R., Randolph, T. M., and Manzella, D. H., "Life and Operating Range Extension of the BPT-4000 Qualification Model Hall Thruster," *42nd AIAA/ASME/SAE/ASEE Joint Propulsion Conference & ExhibitAIAA/ASME/SAE/ASEE Joint Propulsion Conference & Exhibit*, AIAA Paper 2006-5263, Sacramento, California, USA, July 2006.

[15] Hofer, R. R., Mikellides, I. G., Katz, I., and Goebel, D. M., "BPT-4000 Hall thruster discharge chamber erosion model comparison with qualification life test data," *30th International Electric Propulsion Conference*, IEPC Paper 2007-267, Florence, Italy, 2007.

[16] Garnier, Y., Viel, V., Roussel, J.-F., and Bernard, J., "Low-energy xenon ion sputtering of ceramics investigated for stationary plasma thrusters," *Journal of Vacuum Science and Technology A*, Vol. 17, No. 6, 1999, pp. 3246–3254.

[17] Manzella, D., Yim, J., and Boyd, I., "Predicting Hall Thruster Operational Lifetime," *40th AIAA/ASME/SAE/ASEE Joint Propulsion Conference & Exhibit*, No. July in AIAA Paper 2004-3953, Fort Lauderdale, Florida, July 2004.

[18] Sigmund, P., "Theory of Sputtering. I. Sputtering Yield of Amorphous and Polycrystalline Targets," *Physical Review*, Vol. 184, No. 2, 1969, pp. 383–416.

[19] Sigmund, P., "Sputtering by Ion Bombardment: Theoretical Concepts," *Sputtering by Particle Bombardment I: Physical Sputtering of Single-Element Solids*, edited by R. Behrisch, Vol. 47 of *Topics in Applied Physics*, Springer-Verlag, New York, 1981.

[20] Thompson, M. W., "II. The energy spectrum of ejected atoms during the high energy sputtering of gold," *Philosophical Magazine*, Vol. 18, No. 152, 1968, pp. 377–414. doi:10.1080/14786436808227358.

[21] Betz, G. and Wien, K., "Energy and angular distributions of sputtered particles," *International Journal of Mass Spectrometry and Ion Processes*, Vol. 140, No. 1, 1994, pp. 1–110.

[22] Bohdansky, J., "A universal relation for the sputtering yield of monatomic solids at normal ion incidence," *Nuclear Instruments and Methods in Physics Research B*, Vol. 2, No. 1-3, 1984, pp. 587–591.

[23] Matsunami, N., Yamamura, Y., Itikawa, Y., Itoh, N., Kazumata, Y., Miyagawa, S., Morita, K., and Shimizu, R., "A semiempirical formula for the energy dependence of the sputtering yield," *Radiation Effects Letters*, Vol. 57, No. 1-2, 1981, pp. 15–21. doi:10.1080/01422448008218676.

[24] Yamamura, Y. and Tawara, H., "Energy Dependence of Ion-Induced Sputtering Yields From Monatomic Solids At Normal Incidence," *Atomic Data and Nuclear Data Tables*, Vol. 62, No. 2, 1996, pp. 149–253. doi:10.1006/adnd.1996.0005.

[25] Cheng, S. Y. and Martínez-Sánchez, M., "Modeling of Hall thruster lifetime and erosion," *30th International Electric Propulsion Conference*, IEPC Paper 2007-250, Florence, Italy, Sept. 2007.

[26] Gamero-Castaño, M. and Katz, I., "Estimation of Hall Thruster Erosion Using HPHall," *29th International Electric Propulsion Conference*, IEPC Paper 2005-303, Princeton, New Jersey, USA, Nov. 2005.

[27] Yamamura, Y. and Shindo, S., "An empirical formula for angular dependence of sputtering yields," *Radiation Effects*, Vol. 80, No. 1-2, 1984, pp. 57–72. doi:10.1080/00337578408222489.

[28] Zhang, Z. and Zhang, L., "Anisotropic angular distribution of sputtered atoms," *Radiation Effects and Defects in Solids*, Vol. 159, No. 5, May 2004, pp. 301–307. doi:10.1080/10420150410001724495.

[29] Zhang, L. and Zhang, Z., "Anisotropic energy distribution of sputtered atoms induced by low energy heavy ion bombardment," *Radiation Effects & Defects in Solids*, Vol. 160, No. 8, Aug. 2005, pp. 337–347. doi:10.1080/10420150500396803.

[30] Hohenberg, P. and Kohn, W., "Inhomogeneous electron gas," *Physical Review*, Vol. 136, No. 3B, 1964, pp. B864–B871. doi:10.1103/PhysRevB.7.1912.

[31] Ziegler, J. F., Ziegler, M., and Biersack, J., "SRIM The stopping and range of ions in matter (2010)," *Nuclear Instruments and Methods in Physics Research Section B: Beam Interactions with Materials and Atoms*, Vol. 268, No. 11-12, June 2010, pp. 1818–1823. doi:10.1016/j.nimb.2010.02.091.

[32] Biersack, J. P. and Eckstein, W., "Sputtering studies with the Monte Carlo Program TRIM.SP," *Applied Physics A Solids and Surfaces*, Vol. 34, No. 2, 1984, pp. 73–94. doi:10.1007/BF00614759.

[33] Eckstein, W. and Biersack, J. P., "Computer simulation of two-component target sputtering," *Applied Physics A Solids and Surfaces*, Vol. 37, No. 2, 1985, pp. 95–108. doi:10.1007/BF00618859.

[34] Chen, M., Rohrbach, G., Neuffer, A., Barth, K.-L., and Lunk, A., "Simulation of boron nitride sputtering process and its comparison with experimental data," *IEEE Transactions on Plasma Science*, Vol. 26, No. 6, 1998, pp. 1713–1717. doi:10.1109/27.747890.

[35] Tao, L. and Yalin, A., "LIF Velocity Measurement of Sputtered Boron Atoms from Boron Nitride Target," *46th AIAA/ASME/SAE/ASEE Joint Propulsion Conference & Exhibit*, No. July in AIAA Paper 2010-6526, Nashville, Tennessee, USA, July 2010.

[36] Tao, L. and Yalin, A., "Velocity Profiles of Boron Atoms Sputtered from Boron Nitride by Low Energy Xenon Ions," *32nd International Electric Propulsion Conference*, IEPC Paper 2011-067, Wiesbaden, Germany, Sept. 2011.

[37] Alder, B. J. and Wainwright, T. E., "Studies in Molecular Dynamics. I. General Method," *The Journal of Chemical Physics*, Vol. 31, No. 2, 1959, pp. 459–466. doi:http://dx.doi.org/10.1063/1.1730376.

[38] Rahman, A., "Correlations in the Motion of Atoms in Liquid Argon," *Phys. Rev.*, Vol. 136, Oct 1964, pp. A405–A411. doi:10.1103/PhysRev.136.A405.

[39] Smith, B. D. and Boyd, I. D., "Computation of Total and Differential Sputter Yields of Boron Nitride Using Molecular Dynamics," *33rd International Electric Propulsion Conference*, IEPC Paper 2013-156, Washington, DC, USA, Oct. 2013.

[40] Mikellides, I. G. and Katz, I., "Numerical simulations of Hall-effect plasma accelerators on a magnetic-field-aligned mesh," *Physical Review E*, Vol. 86, No. 4, Oct. 2012, pp. 046703. doi:10.1103/PhysRevE.86.046703.

[41] Mikellides, I. G., Katz, I., Hofer, R. R., Goebel, D. M., de Grys, K., and Mathers, A., "Magnetic Shielding of the Acceleration Channel Walls in a Long-Life Hall Thruster," *46th AIAA/ASME/SAE/ASEE Joint Propulsion Conference & Exhibit*, No. July in AIAA Paper 2010-6942, Nashville, Tennessee, USA, July 2010. doi:doi:10.2514/6.2010-6942.

[42] Mikellides, I. G., Katz, I., and Hofer, R. R., "Design of a Laboratory Hall Thruster with Magnetically Shielded Channel Walls, Phase I: Numerical Simulations," *47th AIAA/ASME/SAE/ASEE Joint Propulsion Conference & Exhibit*, No. August in AIAA Paper 2011-5809, San Diego, California, USA, Aug. 2011, pp. 1–18.

[43] Gates, M., Stich, S., Mcdonald, M., Muirhead, B., Mazanek, D., Abell, P., and Lopez, P., "The Asteroid Redirect Mission and sustainable human exploration," *65th International Astronautical Congress*, IAC Paper 14.A5.1.1, Toronto, Canada, Sept. 2014, pp. 1–9.

[44] Bird, G. A., *Molecular Gas Dynamics and the Direct Simulation of Gas Flows*, No. 42 in Oxford engineering science series, Clarendon Press, 1994.

[45] Dragnea, H. C., Boyd, I. D., Lee, B. C., and Yalin, A. P., "Characterization of Eroded Boron Atoms in the Plume of a Hall Thruster," *33rd International Electric Propulsion Conference*, IEPC Paper 2013-158, Washington, DC, USA, Oct. 2013.

[46] Dragnea, H. C., Boyd, I. D., Lee, B. C., and Yalin, A. P., "Characterization of Eroded Boron Atoms in the Plume of a Hall Thruster," *IEEE Transactions on Plasma Science*, Vol. 43, No. 1, 2015, pp. 35–44.

[47] Hockney, R. W. and Eastwood, J. W., *Computer Simulation Using Particles*, IOP Publishing Ltd, Bristol, 1988.

[48] Birdsall, C. K. and Langdon, A. B., *Plasma Physics via Computer Simulation*, Taylor & Francis Group, New York, 2004.

[49] Hara, K., *Development of Grid-Based Direct Kinetic Method and Hybrid Kinetic-Continuum Modeling of Hall Thruster Discharge Plasmas*, Ph.D. thesis, University of Michigan, 2015.

[50] Hara, K., Chapman, T., Banks, J. W., Brunner, S., Joseph, I., Berger, R. L., and Boyd, I. D., "Quantitative study of the trapped particle bunching instability in Langmuir waves," *Physics of Plasmas*, Vol. 22, No. 2, 2015, pp. 022104. doi:10.1063/1.4906884.

[51] Fife, J., *Hybrid-PIC Modeling and Electrostatic Probe Survey of Hall Thrusters*, Ph.D. thesis, Massachusetts Institute of Technology, 1999.

[52] Koo, J., *Hybrid PIC-MCC computational modeling of Hall thrusters*, Ph.D. thesis, University of Michigan, 2005.

[53] Fife, J. M., Martínez-Sánchez, M., and Szabo, J., "A numerical study of low-frequency discharge oscillations in Hall thrusters," *33rd AIAA/ASME/SAE/ASEE Joint Propulsion Conference & Exhibit*, Seattle, Washington, USA, July 1997.

[54] Hara, K., Sekerak, M. J., Boyd, I. D., and Gallimore, A. D., "Mode transition of a Hall thruster discharge plasma," *Journal of Applied Physics*, Vol. 115, No. 20, 2014, pp. 203304. doi:10.1063/1.4879896.

[55] Hara, K. and Boyd, I. D., "Axial-Azimuthal Hybrid-Direct Kinetic Simulation of Hall Effect Thrusters," *34th International Electric Propulsion Conference*, IEPC Paper 2015-283, Kobe, Japan, July 2015.

[56] Cheng, S., *Modeling of Hall thruster lifetime and erosion mechanisms*, Ph.D. thesis, Massachusetts Institute of Technology, 2007.

[57] Anderson, J. a., Lorenz, C. D., and Travesset, a., "General purpose molecular dynamics simulations fully implemented on graphics processing units," *Journal of Computational Physics*, Vol. 227, No. 10, May 2008, pp. 5342–5359. doi:10.1016/j.jcp.2008.01.047.

[58] Nickolls, J., Buck, I., Garland, M., and Skadron, K., "Scalable parallel programming with CUDA," *ACM Queue*, Vol. 6, No. 2, April 2008, pp. 40–53.

[59] Swope, W. C., Andersen, H. C., Berens, P. H., and Wilson, K. R., "A computer simulation method for the calculation of equilibrium constants for the formation of physical clusters of molecules: Application to small water clusters," *J. Chem. Phys.*, Vol. 76, No. 1, 1982, pp. 637–649. doi:10.1063/1.442716.

[60] Albe, K., Möller, W., and Heinig, K., "Computer simulation and boron nitride," *Radiation Effects and Defects in Solids*, Vol. 141, June 1997, pp. 85–97. doi:10.1080/10420159708211560.

[61] Albe, K. and Möller, W., "Modelling of boron nitride: Atomic scale simulations on thin film growth," *Computational materials science*, Vol. 10, 1998, pp. 111–115.

[62] Bazant, M. Z., Kaxiras, E., and Justo, J. F., "Environment Dependent Interatomic Potential for Bulk Silicon," *Physical Review B*, Vol. 56, No. 14, 1997, pp. 8542–8552. doi:10.1103/PhysRevB.56.8542.

[63] Biersack, J. and Ziegler, J., "The Stopping and Range of Ions in Solids," *Ion Implantation Techniques*, edited by H. Ryssel and H. Glawischnig, Vol. 10 of *Springer Series in Electrophysics*, Springer Berlin Heidelberg, 1982, pp. 122–156. doi:10.1007/978-3-642-68779-2_5.

[64] O'connor, D. and Biersack, J., "Comparison of theoretical and empirical interatomic potentials," *Nuclear Instruments and Methods in Physics Research B*, Vol. 15, 1986, pp. 14–19.

[65] Berendsen, H. J. C., Postma, J. P. M., van Gunsteren, W. F., DiNola, A., and Haak, J. R., "Molecular dynamics with coupling to an external bath," *The Journal of Chemical Physics*, Vol. 81, No. 8, Oct. 1984, pp. 3684–3690.

[66] Rubin, B., Topper, J., and Yalin, A., "Total and differential sputter yields of boron nitride measured by quartz crystal microbalance," *Journal of Physics D: Applied Physics*, Vol. 42, Oct. 2009, pp. 1–11. doi:10.1088/0022-3727/42/20/205205.

[67] Yalin, A., Surla, V., Farnell, C., Butweiller, M., and Williams, J., "Sputtering studies of multi-component materials by weight loss and cavity ring-down spectroscopy," *42nd AIAA/ASME/SAE/ASEE Joint Propulsion Conference & Exhibit*, No. July, Sacramento, California, USA, July 2006.

[68] Sun, Q. and Boyd, I. D., "Evaluation of Macroscopic Properties in the Direct Simulation Monte Carlo Method," *Journal of Thermophysics and Heat Transfer*, Vol. 19, No. 3, July 2005, pp. 329–335. doi:10.2514/1.12542.

[69] Smith, B. D. and Boyd, I. D., "Molecular Dynamics Computation of Steady-State Sputter Yields of Hexagonal Boron Nitride," *34th International Electric Propulsion Conference*, IEPC Paper 2015-278, Kobe, Japan, July 2015.

[70] Yalin, A. P., Williams, J. D., Surla, V., and Zoerb, K. A., "Differential sputter yield profiles of molybdenum due to bombardment by low energy xenon ions at normal and oblique incidence," *Journal of Physics D: Applied Physics*, Vol. 40, No. 10, May 2007, pp. 3194–3202. doi:10.1088/0022-3727/40/10/025.

[71] Huismann, T., *Improving Hall Thruster Plume Simulation through Refined Characterization of Near-field Plasma Properties*, Ph.D. thesis, University of Michigan, 2011.

[72] Hofer, R., Katz, I., Mikellides, I., and Gamero-Castaño, M., "Heavy Particle Velocity and Electron Mobility Modeling in Hybrid-PIC Hall Thruster Simulations," *42nd AIAA/ASME/SAE/ASEE Joint Propulsion Conference & Exhibit*, No. July in AIAA Paper 2006-4658, Sacramento, California, USA, July 2006.

[73] Parra, F. I., Ahedo, E., Fife, J. M., and Martinez-Sanchez, M., "A two-dimensional hybrid model of the Hall thruster discharge," *Journal of Applied Physics*, Vol. 100, No. 2, 2006, pp. 023304. doi:10.1063/1.2219165.

[74] Parra, F., Escobar, D., and Ahedo, E., "Improvements on particle accuracy in a Hall thruster hybrid code," *42nd AIAA/ASME/SAE/ASEE Joint Propulsion Conference & Exhibit*, No. July in AIAA Paper 2006-4830, Sacramento, California, USA, July 2006, pp. 1–9.

[75] Hofer, R., Mikellides, I., Katz, I., and Goebel, D., "Wall sheath and electron mobility modeling in hybrid-PIC Hall thruster simulations," *43rd AIAA/ASME/SAE/ASEE Joint Propulsion Conference & Exhibit*, No. July in AIAA Paper 2007-5267, Cincinnati, Ohio, USA, 2007.

[76] Hofer, R., Katz, I., Mikellides, I., Goebel, D. M., Jameson, K. K., Sullivan, R. M., and Johnson, L. K., "Efficacy of Electron Mobility Models in Hybrid-PIC Hall Thruster Simulations," *44th AIAA/ASME/SAE/ASEE Joint Propulsion Conference & Exhibit*, No. 2008-4924 in AIAA Paper 2008-4924, Hartford, Connecticut, USA, July 2008.

[77] Ahedo, E., Santos, R., and Parra, F. I., "Fulfillment of the kinetic Bohm criterion in a quasineutral particle-in-cell model," *Physics of Plasmas*, Vol. 17, No. 7, 2010, pp. 073507. doi:10.1063/1.3456516.

[78] Smith, B. D., Boyd, I. D., and Kamhawi, H., "Influence of Triply-Charged Ions and Ionization Cross-Sections in a Hybrid-PIC Model of a Hall Thruster Discharge," *50th AIAA/ASME/SAE/ASEE Joint Propulsion Conference*, AIAA Paper 2014-3429, Cleveland, Ohio, USA, July 2014, pp. 1–17.

[79] Hobbs, G. D. and Wesson, J. a., "Heat flow through a Langmuir sheath in the presence of electron emission," *Plasma Physics*, Vol. 9, No. 1, 2002, pp. 85–87. doi:10.1088/0032-1028/9/1/410.

[80] Goebel, D. M. and Katz, I., *Fundamentals of Electric Propulsion*, JPL Space Science and Technology Series, John Wiley & Sons, Inc., Hoboken, New Jersey, 2008.

[81] Drawin, H.-W., "Zur formelmäßigen Darstellung der Ionisierungsquerschnitte gegenüber Elektronenstoß," *Zeitschrift für Physik*, Vol. 164, 1961, pp. 513–521, in German.

[82] Mathur, D. and Badrinathan, C., "Ionization of xenon by electrons: Partial cross sections for single, double, and triple ionization," *Physical Review A*, Vol. 35, No. 3, 1987, pp. 1033–1042.

[83] Katz, I., Hofer, R. R., and Goebel, D. M., "Ion Current in Hall Thrusters," *IEEE Transactions on Plasma Science*, Vol. 36, No. 5, Oct. 2008, pp. 2015–2024. doi:10.1109/TPS.2008.2004219.

[84] Stephan, K. and Märk, T. D., "Absolute partial electron impact ionization cross sections of Xe from threshold up to 180 eV," *The Journal of Chemical Physics*, Vol. 81, No. 7, 1984, pp. 3116–3117. doi:10.1063/1.448013.

[85] Wetzel, R., Baiocchi, F., Hayes, T., and Freund, R., "Absolute cross sections for electron-impact ionization of the rare-gas atoms by the fast-neutral-beam method," *Physical Review A*, Vol. 35, No. 2, 1987, pp. 559–577.

[86] Hofer, R., Goebel, D., Mikellides, I., and Katz, I., "Design of a laboratory Hall thruster with magnetically shielded channel walls, phase II: experiments," *48th AIAA/ASME/SAE/ASEE Joint Propulsion Conference & Exhibit*, AIAA Paper 2012-3788, Atlanta, Georgia, USA, Aug. 2012.

[87] Achenbach, C., Mueller, A., Salzborn, E., and Becker, R., "Electron-impact double ionization of I1+ and Xeq+ (q=1,...,4) ions: role of 4d electrons like in photoionization," *Physical Review Letters*, Vol. 50, No. 26, June 1983, pp. 4–7.

[88] Achenbach, C., Mueller, A., Salzborn, E., and Becker, R., "Single ionisation of multiply charged xenon ions by electron impact," *Journal of Physics B: Atomic and Molecular Physics*, Vol. 17, No. 7, 1984, pp. 1405–1425.

[89] Smith, B. D., Boyd, I. D., and Kamhawi, H., "Hybrid-PIC Modeling of the Transport of Atomic Boron in a Hall Thruster," *34th International Electric Propulsion Conference*, IEPC Paper 2015-252, Kobe, Japan, July 2015.

[90] Fuhr, J. R. and Wiese, W. L., "Tables of Atomic Transition Probabilities for Beryllium and Boron," *Journal of Physical and Chemical Reference Data*, Vol. 39, No. 1, 2010, pp. 013101. doi:10.1063/1.3286088.

[91] Kim, Y.-K. and Stone, P. M., "Ionization of boron, aluminum, gallium, and indium by electron impact," *Physical Review A*, Vol. 64, No. 5, Oct. 2001, pp. 052707. doi:10.1103/PhysRevA.64.052707.

[92] Ballance, C. P., Griffin, D. C., Berrington, K. a., and Badnell, N. R., "Electron-impact excitation of neutral boron using the R -matrix with the pseudostates method," *Journal of Physics B: Atomic, Molecular and Optical Physics*, Vol. 40, No. 6, March 2007, pp. 1131–1139. doi:10.1088/0953-4075/40/6/004.

[93] Kamhawi, H., Manzella, D., Pinero, L., Haag, T., Mathers, A., and Liles, H., "In-Space Propulsion High Voltage Hall Accelerator Development Project Overview," *45th AIAA/ASME/SAE/ASEE Joint Propulsion Conference & Exhibit*, AIAA Paper 2009-5282, Denver, Colorado, USA, Aug. 2009, pp. 1–12.

[94] Kamhawi, H., Manzella, D., Pinero, L., Haag, T., and Huang, W., "In-Space Propulsion High Voltage Hall Accelerator Development Project Overview," *46th AIAA/ASME/SAE/ASEE Joint Propulsion Conference & Exhibit*, AIAA Paper 2010-6860, Nashville, Tennessee, USA, July 2010.

[95] Kamhawi, H., Haag, T., Pinero, L., Huang, W., Peterson, T., Manzella, D., Dankanich, J., Mathers, A., and Hobson, D., "Overview of the Development of a Low-Cost High Voltage Hall Accelerator Propulsion System for NASA Science Missions," *47th AIAA/ASME/SAE/ASEE Joint Propulsion Conference & Exhibit*, No. August in AIAA Paper 2011-5520, San Diego, California, USA, 2011, pp. 1–11.

[96] Kamhawi, H., Pinero, L., Haag, T., Peterson, T., Huang, W., Dankanich, J., Shastry, R., and Mathers, A., "High Voltage Hall Accelerator Propulsion System Development for NASA Science Missions," *2013 IEEE Aerospace Conference*, Big Sky, Montana, USA, March 2013.

[97] Shastry, R., private communication.

[98] Lee, B. C., Yalin, A. P., Gallimore, A., Huang, W., and Kamhawi, H., "Real-Time Boron Nitride Erosion Measurements of the HiVHAc Thruster via Cavity Ring-Down Spectroscopy," *33rd International Electric Propulsion Conference*, IEPC Paper 2013-119, Washington, DC, USA, Oct. 2013.

[99] Smith, B. D., Boyd, I. D., Kamhawi, H., and Huang, W., "Hybrid-PIC modeling of a high-voltage, high-specific-impulse Hall thruster," *49th*

AIAA/ASME/SAE/ASEE Joint Propulsion Conference & Exhibit, AIAA Paper 2013-3887, San Jose, California, USA, July 2013, pp. 1–11.

[100] "Hot-Pressed Boron Nitride Shapes," product brochure, Momentive Performance Materials, Inc., 2012.

[101] Huang, W., *Study of Hall Thruster Discharge Channel Wall Erosion via Optical Diagnostics by Wensheng Huang*, Ph.D. thesis, University of Michigan, 2011.